JOURNAL OF MATERIALS RESEARCH AND TECHNOLOGY 2023;23:3362–3423

Available online at www.sciencedirect.com

jmr&t Journal of Materials Research and Technology

journal homepage: www.elsevier.com/locate/jmrt

Review Article

Twenty years of the CoCrFeNiMn high-entropy alloy: achieving exceptional mechanical properties through microstructure engineering

Hamed Shahmir [a,*], *Mohammad Sajad Mehranpour* [a], *Seyed Amir Arsalan Shams* [b], *Terence G. Langdon* [c]

[a] *Department of Materials Engineering, Tarbiat Modares University, Tehran, Iran*

[b] *Graduate Institute of Ferrous Technology, Pohang University of Science and Technology, Pohang, 37673, Republic of Korea*

[c] *Materials Research Group, Department of Mechanical Engineering, University of Southampton, Southampton, SO17 1BJ, UK*

ARTICLE INFO

Article history:
Received 6 December 2022
Accepted 24 January 2023
Available online 1 February 2023

Keywords:
CoCrFeNiMn
High-entropy alloy
Mechanical properties
Microstructure engineering
Thermomechanical treatment

ABSTRACT

The CoCrFeNiMn multicomponent is one of the most widely and best studied of all high-entropy alloys (HEAs) since its exceptional properties suggest potential uses as a structural material in many industrial applications. In practice, a good balance between strength and ductility is one of the most important challenges in developing alloys in modern materials science and engineering. There have been many attempts to overcome the strength-ductility trade-off in the CoCrFeNiMn alloy due to its relatively low strength. These attempts include adding a minor sixth element, such as oxide or carbide particles, and also developing thermomechanical processing for grain refinement or precipitation to produce a tailored microstructure with optimum mechanical properties. This review describes the deformation mechanisms and the microstructural evolutions in this alloy during plastic deformation under different conditions of temperature, strain and strain rate where these are important for the processing and manufacturing of the alloy. In addition, this study provides a perspective on the behavior of the alloy under high temperature exposure and also under cyclic loading which is generally the most important factor in industrial applications. This understanding demonstrates that there is a very large potential for the future enhancement and optimization of this and other comparable HEAs.

* Corresponding author.
E-mail address: shahmir@modares.ac.ir (H. Shahmir).
https://doi.org/10.1016/j.jmrt.2023.01.181

1. Introduction

The CoCrFeNiMn multicomponent or high-entropy alloy, known as the Cantor alloy, is an equi-atomic alloy with a single-phase structure which was introduced and developed by Cantor et al. almost twenty years ago [1]. It is one of the most widely and best studied high-entropy alloys (HEAs) as a new class of material containing five or more principal elements with each elemental concentration lying between 5 at% and 35 at% [1,2].

Although the general concept of these alloys was not at first considered, the overall interest in these alloys developed rapidly so that they became a significant topic in the field of materials science and engineering with an ever-increasing number of research publications. Several parameters have been proposed for the prediction of phase formations in order to achieve a single-phase structure in HEAs and this includes the enthalpy of mixing (ΔH_{mix}), the entropy of mixing (ΔS_{mix}), the atomic size difference (δ) and the electronegativity on the Pauling scale ($\Delta\chi_P$) as defined by Eqs. (1)–(4) [3–6]. The calculations to obtain these parameters for the equiatomic CoCrFeNiMn HEA are given by

$$\Delta H_{mix} = \sum_{i=1.i\neq j}^{n} 4H_{ij}c_i c_j \quad (1)$$

where H_{ij} is the mixing enthalpy of binary liquid alloys as in Table 1 and

$$\Delta S_{mix} = -R\sum_{i=1}^{n} c_i \ln c_i \quad (2)$$

where R is the gas constant and

$$\delta = 100\sqrt{\sum_{i=1}^{n} c_i(1-r_i/r)^2} \quad (3)$$

where $\bar{r} = \sum_{i=1}^{n} c_i r_i$, ci and ri are the atomic percentage and atomic radius of the ith element, and

$$\Delta\chi_{P=}\sqrt{\sum_{i=1}^{n} c_i(\chi_i-\chi)^2} \quad (4)$$

where $\overline{\chi} = \sum_{i=1}^{n} c_i\chi_i$ and χ_i is the Pauling electronegativity for the ith element.

Calculations revealed that ΔH_{mix} and ΔS_{mix} are −3.36 kJ $mol^{-1}$and 13.38 J. K^{-1} mol^{-1}, respectively, for the equiatomic CoCrFeNiMn HEA. The criteria for the formation of the simple disorder phase in HEAs are $-15 \leq \Delta H_{mix} \leq 5$ kJ mol^{-1}, $\delta \leq 4.3$, and $12 \leq \Delta S_{mix} \leq 17.5$ J $(K\ mol)^{-1}$ [7,8]. In practice, a large δ leads to excess strain energy and therefore destabilizes simple structures. This parameter is equal to 3.27% for the equiatomic CoCrFeNiMn HEA and this is sufficiently low to encourage the formation of a single-phase alloy. It has been shown that the formation of a topologically close-packed phase like the sigma phase can be observed when $\Delta\chi_{Pauling} > 13.3\%$ [9]. The calculation of this parameter in the Cantor alloy ($\Delta\chi_P = 13.84\%$) predicted the formation of the sigma phase and many investigations subsequently confirmed the formation of this phase in this HEA after heat treatment at <800 °C.

The Cantor alloy exhibits an excellent strain hardening capability, exceptional ductility at ambient and cryogenic temperatures; and a promising fracture toughness at cryogenic temperatures [10–12] which designates it as a structural material with extraordinary properties for many industrial applications. Basically, the equiatomic CoCrFeNiMn HEA shows a relatively low yield stress (YS ≈ 300 MPa) and ultimate tensile strength (UTS ≈ 500 MPa) at room temperature which has led to many efforts to modify the alloy in order to improve the mechanical properties for practical applications [11–13].

There are four fundamental methods in physical metallurgy by which the resistance to plastic deformation of a metal may be increased, including solid solution strengthening by adding interstitial and substitutional elements, strain hardening by plastic deformation, grain refinement through the application of severe plastic deformation (SPD) and appropriate thermomechanical treatments, and precipitation or particle hardening by aging or appropriate thermomechanical effects. It is well known that one or more of these effects are often used in the production of modern high-strength alloys. In the general perspective, improving the strength without losing the ductility denotes the microstructural engineering of the alloy. Therefore, it is apparent that many methods are now available to tailor the microstructure of the CoCrFeNiMn HEA to cover the requirements of any applications in industry.

Solid solution strengthening in the Cantor alloy, as in other materials, depends on the size mismatch and the chemical bonding of the added solutes. Although most of the added substitutional alloying elements make no effective contribution to this mechanism, interstitial solutes such as C, N, B and even H may play a significant role in this mechanism in the Cantor alloy. However, precipitates appearing in the microstructure when the concentration of the sixth alloying element goes further than its solubility are found to be especially effective in enhancing the mechanical properties. For example, adding 2 at. % of Ti leads to an ultimate tensile strength (UTS) as high as ~2220 MPa. Moreover, adding interstitials such as B by only 30 ppm leads to a high elongation of ~55% and a UTS of ~1000 MPa so that this is one of the best alloying elements to overcome the strength-ductility trade-off. Deformation mechanisms such as mechanical twinning and transformation-induced plasticity may also be triggered by alloying elements such as H and Si.

A good balance between strength and ductility is one of the most important issues associated with the CoCrFeNiMn HEA. Many attempts have been made to overcome the strength-ductility trade-off such as adding oxide or carbide particles,

Table 1 – The mixing enthalpy ΔH_{mix} ($kJ.mol^{-1}$) and atomic radii (nm) of each element [3].

Element	Co	Cr	Fe	Ni	Mn
Atomic radii (nm)	0.125	0.128	0.126	0.124	0.135
Co	0	−4.5	−0.6	−0.2	−5.2
Cr	–	0	−1.5	−6.7	2.1
Fe	–	–	0	−1.6	0.2
Ni	–	–		0	−8.2
Mn	–	–	–	–	0

adding minor elements and/or numerous types of thermo-mechanical processing to obtain tailored microstructures. Amongst these approaches, thermomechanical processing is a well-established industrial method for overcoming the strength-ductility trade-off. One of the most popular methods is through the use of cold deformation followed by annealing within a specific temperature range. The formation of Cr-rich precipitates (*bcc* and sigma), ultrafine grain sizes, bimodal microstructures and heterogeneous microstructures including both recrystallized and non-recrystallized regions play vital roles in determining the mechanical properties. In addition, CoCrFeNiMn composites have remarkable mechanical properties at high temperatures [14].

Since studies of the behaviour of HEAs under cyclic loads extend over a period of less than one decade, this field of study may be regarded as generally premature. However, initial reports show that the CoCrFeNiMn alloy exhibits an intermediate fatigue resistance among engineering alloys. The fatigue-crack growth resistance and low-cycle fatigue of the Cantor alloy outperform those of austenitic stainless steels, Al and Mg alloys, and in general they are similar to those of twinning-induced plasticity (TWIP) steel but less than for Ni-base superalloys, copper, titanium alloys and metastable HEAs. The alloy also shows a much better fatigue limit than most other engineering alloys such as stainless steels, TWIP steels and pure titanium.

Surprisingly, the mechanical characteristics of the CoCrFeNiMn HEA, including the yield stress (YS), UTS and elongation to fracture, increase simultaneously with decreasing temperature from room to liquid nitrogen temperature. This behavior is attributed to the new interfaces that form due to nano-deformation twinning and the dynamic Hall-Petch mechanism. This phenomenon effectively postpones the early onset of necking instability and improves the degree of work hardening and fracture toughness at low temperatures [12,15,16].

Obviously, even after almost twenty years since the introduction of the Cantor alloy, it is now only the beginning of developing a fundamental understanding of this alloy as a new structural material which may be used in industry. Accordingly, this review was undertaken to provide a summary of the main attempts undertaken to date to improve the mechanical properties, and specifically the strength, of the CoCrFeNiMn HEA through the use of microstructure engineering.

2. Plastic deformation and strain hardening

2.1. *Deformation mechanisms in the CoCrFeNiMn HEA*

During plastic deformation, the microstructure of materials changes based on the two important factors of (1) the intrinsic characteristics of the material such as the crystal structure, Young's modulus, stacking-fault energy (SFE) and melting point and (2) the processing parameters such as strain, strain rate and the temperature of deformation. It is well-known that three deformation mechanisms of dislocation slip, deformation-induced twinning and deformation-induced martensitic transformations are introduced in face-centered cubic (*fcc*) materials mainly based on the SFE and deformation temperature/pressure. Based on the difficulty of cross slip in metals with low values of the SFE, deformation-induced twinning and martensitic-phase transformations may occur to accommodate the applied strain during deformation. It is well-established that deformation-induced twinning is a major deformation mechanism in *fcc* metals having SFEs lower than ~25 mJ m^{-2} and deformation-induced martensitic phase transformations may appear in *fcc* metals with SFEs lower than ~15 mJ m^{-2} [17]. In addition, lowering the deformation temperature or increasing the pressure promotes the appearance of other plastic deformation mechanisms together with dislocation slip.

Basically, the CoCrFeNiMn HEA with a single-phase *fcc* crystal structure has a major potential for easy deformation by dislocation slip due to the high activity of its slip systems. It was reported that during tensile testing the initial plasticity occurred exclusively by planar glide of 1/2<110> dislocations on the {111} planes and at higher strains the slip became more homogeneous with the development of cell structures [11]. However, the low value of SFE in this alloy affects the role of slip during plastic deformation. It was proposed that the energy difference between the energy state of the stacking fault and that of the matrix is inherently reduced due to the high energy level of the heavily-distorted matrix in the CoCrFeNiMn HEA [18]. This mechanism is fundamentally different from the Suzuki mechanism in which solute segregates form in stacking faults to reduce their energy [19]. An SFE of ~21 mJ m^{-2} was proposed for the CoCrFeNiMn HEA at room temperature after *ab initio* calculations [20]. Accordingly, deformation twinning is one of the anticipated deformation mechanisms in this HEA after plastic deformation and this was confirmed by many investigations after deformation of the alloy with different grain sizes, ranging from several tens to a few micrometers, at room and cryogenic temperatures [11,12,16,21–23]. The formation of deformation twins, known as the dynamic Hall-Petch effect, decreases the dislocation mean free path and thereby should increase the strength of the material.

The appearance of deformation twins depends on the magnitude of the applied strain in *fcc* metals having low values of SFE. Planar dislocation glide is the deformation mechanism in the early stage of plastic deformation up to ~2% strain in tensile testing [11] or an equivalent strain of 0.05 [24] regardless of the grain size and temperature of plastic deformation in the Cantor alloy. Stacking faults were also observed consistent with the splitting of planar dislocations into Shockley partials at lower strains at different deformation temperatures. The slip became more homogeneous when cell structures developed at higher strain values at room or elevated temperatures. However, nanoscale deformation twins were observed at higher strains, typically >20% during tensile testing, at cryogenic temperatures [11] or at an equivalent strain of ~0.14 at room temperature [24]. The thickness of these twins was in the range of ~0.2–0.3 nm and in these nano-twins the twin-parent repeat distance within the bands ranged from 0.5 to 3 nm. The formation of deformation twins leads to the introduction of new interfaces and therefore produces a high degree of work hardening and a significant increase in strength. It is important to note also that twinning

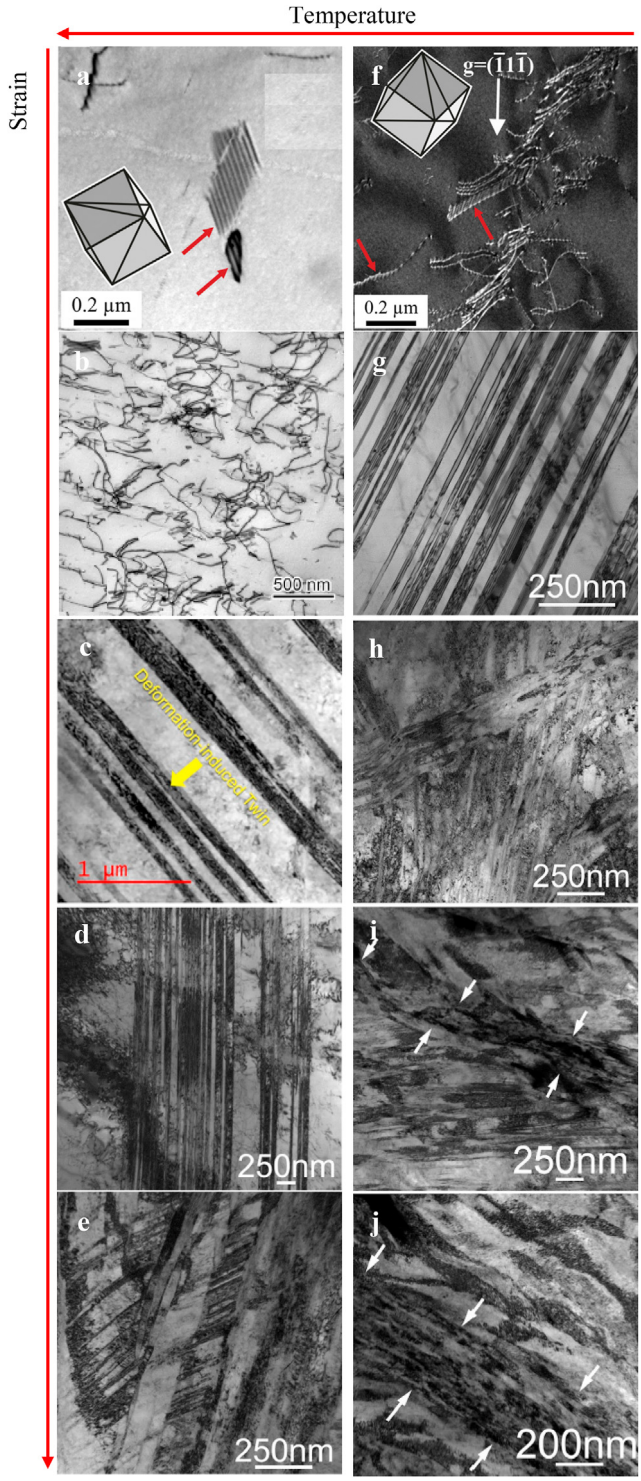

Fig. 1 – TEM images of CoCrFeNiMn HEA after deformation at room (a–e) and cryogenic (at −196 °C) (f–j) temperatures. Microstructure after small plastic deformation: (a,f) (2.4% tensile) [11], (b) 5% tensile testing [24], (c) 28% cold rolling [27], (g) 5% cold rolling and (h) 15% cold rolling [21]. Microstructures after medium (40–60% cold rolling) and large (up to 80% cold rolling) plastic deformation are shown in (d,i) and (e,j), respectively [21]. Arrows show stacking faults in (a,f), twins in (c) and shear bands in (i,j).

is responsible for the high ductility at low temperatures by providing an additional deformation mode [11]. Microstructural evolution during medium (~40–70%) and large (up to ~90%) plastic deformation by rolling at room temperature confirms the important role of twinning together with the motion and generation of dislocations during plastic deformation. Microstructural evolution during wire drawing showed the formation of discrete dislocations, Lomer-Cottrell locks and Taylor lattices in the early stage of deformation after straining of <0.28. Dislocation cells, deformation twins and irregular dislocations appear in the microstructure by increasing the equivalent strain up to ~1.96 and even further increasing the strain leads to the formation of lamellae structures parallel to the metal flow direction that contain twins and shear bands [25].

The microstructural hierarchy during deformation is shown in Fig. 1(a-e) which confirms the proposed scenario. In addition, the role of twinning becomes more prominent during cryogenic plastic deformation as shown in Fig. 1(f-j). The twins are rotated into alignment with the direction of deformation (the rolling plane) as plastic deformation proceeds. Micro-shear bands also appear to form in the microstructure in the later stages of deformation. Isolated shear bands are first seen at medium plastic deformation and specifically in regions where twin alignment with the rolling plane is already well established. These procedures improve the ultimate tensile strength from ~440 MPa before deformation to ~1500 or 1200 MPa after deformation at −196 or 25 °C, respectively [21]. Strongly localized deformation areas associated with extensive shear bands were reported after rotary swaging, as a high stress/strain process, at room temperature [26]. Finally, it is important to note that plastic deformation and strain hardening can improve the strength significantly by operating twining at the expense of reducing the ductility.

2.2. *Heavy and severe plastic deformation*

Many attempts have been undertaken to gain a fundamental understanding of the microstructural evolution in the CoCrFeNiMn HEA during heavy and severe plastic deformation at different temperatures where this is recognized as an effective procedure for improving the strength [11,28–34]. It is well-known that the application of SPD produces significant grain refinement which can improve the mechanical properties of materials [35–37]. Nanostructured alloys fabricated by SPD show significant strength but remarkably limited ductility due to their low rate of strain hardening [38,39]. Accordingly, short-term annealing after deformation is normally mandatory in order to improve the overall ductility with a minimum effect on strength. Thus, a good combination of strength and ductility may be achieved with an opportunity to specifically tailor the microstructure after SPD processing in the CoCrFeNiMn HEA. In practice, however, this short-term annealing of the CoCrFeNiMn alloy is challenging due to a significant potential for decomposition and the formation of new phases which may reduce the ductility (see section 4.3). This low SFE alloy reveals mechanical twinning as an important deformation mechanism at room and cryogenic temperatures and this

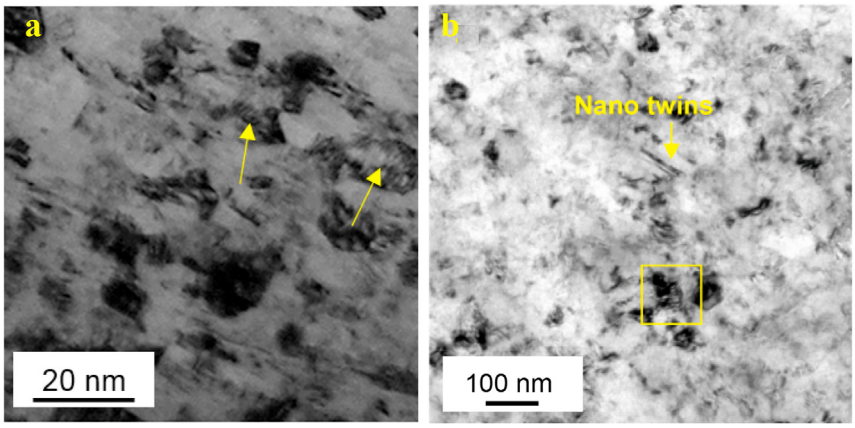

Fig. 2 – TEM images of microstructure of CoCrFeNiMn after SPD by HPT at (a) room temperature and (b) cryogenic temperature. Arrows show grains contain nano-twins [32,40].

plays an important role in grain refinement, as in Fig. 2, through the introduction of extra interfaces within the grains during deformation twinning, thereby reducing the dislocation mean free path and increasing the dislocation density [11,21,32,40]. Moreover, the advent of a deformation-induced martensitic transformation, that is a well-known deformation mechanism accommodating strain during heavy and severe plastic deformation in materials with low SFE [41], was also reported in the CoCrFeNiMn HEA [40] (see section 2.3).

The most important and well known techniques for imposing SPD are high-pressure torsion (HPT) [42] and equal-channel angular pressing (ECAP) [43]. Processing by HPT is especially attractive because it provides a means of tuning the structures of the materials in a manner that is not achievable by conventional processing techniques and this gives an opportunity to study unique nanostructures in materials [42]. In this procedure, a disk-shaped specimen is deformed by simple shear between two anvils where it is constrained under high pressure and subjected to concurrent torsional straining [35,36,44].

Intensive deformation twinning and significant grain refinement are the two main features of microstructural evolution in the CoCrFeNiMn HEA during HPT (Fig. 2) [32]. These twin boundaries may have a significant influence on the evolution and/or the refinement of the microstructure during further straining following the saturation of twinning [21,45–47]. The very high ductility of the alloy in the homogenized condition is primarily associated with the intensive twinning [21] and therefore the decrease in ductility in the HPT-processed samples is a consequence of the cessation of twining at large strains [32]. In fact, the introduction of extra interfaces within the grains during deformation twinning leads to significant grain refinement and extraordinary increments in hardness and strength after HPT processing at room temperature [48]. It is expected that the formation of deformation twins will lead to continuous grain subdivision through the introduction of new interfaces which effectively reduce the dislocation mean free path and cause hardening. Another hardening mechanism is substructure hardening due to the dislocation density [47]. The CoCrFeNiMn alloy was processed by HPT under 6.0 GPa pressure up to 10 turns at room temperature and this processing gave a single-phase nano-grained microstructure (<50 nm) with an exceptional increase in the hardness and strength of ~4.41 and ~1.75 GPa but with a relatively low elongation to fracture of ~4% [32].

In ECAP processing, a rod or bar is forced through a die constrained within a channel that is bent through a sharp angle near the center of the die. The material in this processing method experiences a high shearing strain in a single pass through the die but without any change in its cross-sectional dimensions. Repeating the process through several passes leads to exceptionally high strains in the material. Since relatively large bulk samples may be used in ECAP processing, it is generally considered as a superior method to most other SPD techniques. Furthermore, long rods can be produced easily in a combination of ECAP with subsequent appropriate thermo-mechanical treatments due to the general simplicity of the operation [43,49,50].

The Cantor alloy was successfully processed by ECAP at 400 °C for up to four passes which led to a gradual increase in the hardness from ~1.32 to ~3.09 GPa by increasing the numbers of ECAP passes. The YS and UTS reached ~0.98 and ~0.99 GPa, respectively, with an acceptable elongation to failure of ~35% for the sample processed through four passes. The microstructure after processing through four passes showed a single-phase ultrafine-grained CoCrFeNiMn HEA with an average grain size of ~100 nm and a high dislocation density of ~1.3×10^{9} cm^{-2} [33].

It is well established that processing by SPD can produce an excess free volume including vacancies in the lattice as well as crystal interfaces, dislocations, grain boundaries, nano-voids at triple junctions and micro-cracks in the microstructure [51]. Nano-voids with average sizes of less than 10 nm were detected in the CoCrFeNiMn HEA associated with an excess free volume (~1%) after processing by severe cold shape rolling (SCSR) to an equivalent strain of 4.2 at room temperature where a study of the microstructure revealed significant grain refinement to ~50 nm and a high dislocation density of 2.1×10^{11} cm^{-2} [34]. It is important to note that this remarkable excess free volume is the highest reported value for an *fcc* material processed by SPD and this is probably due to the low value of the SFE in the CoCrFeNiMn HEA and the deformation

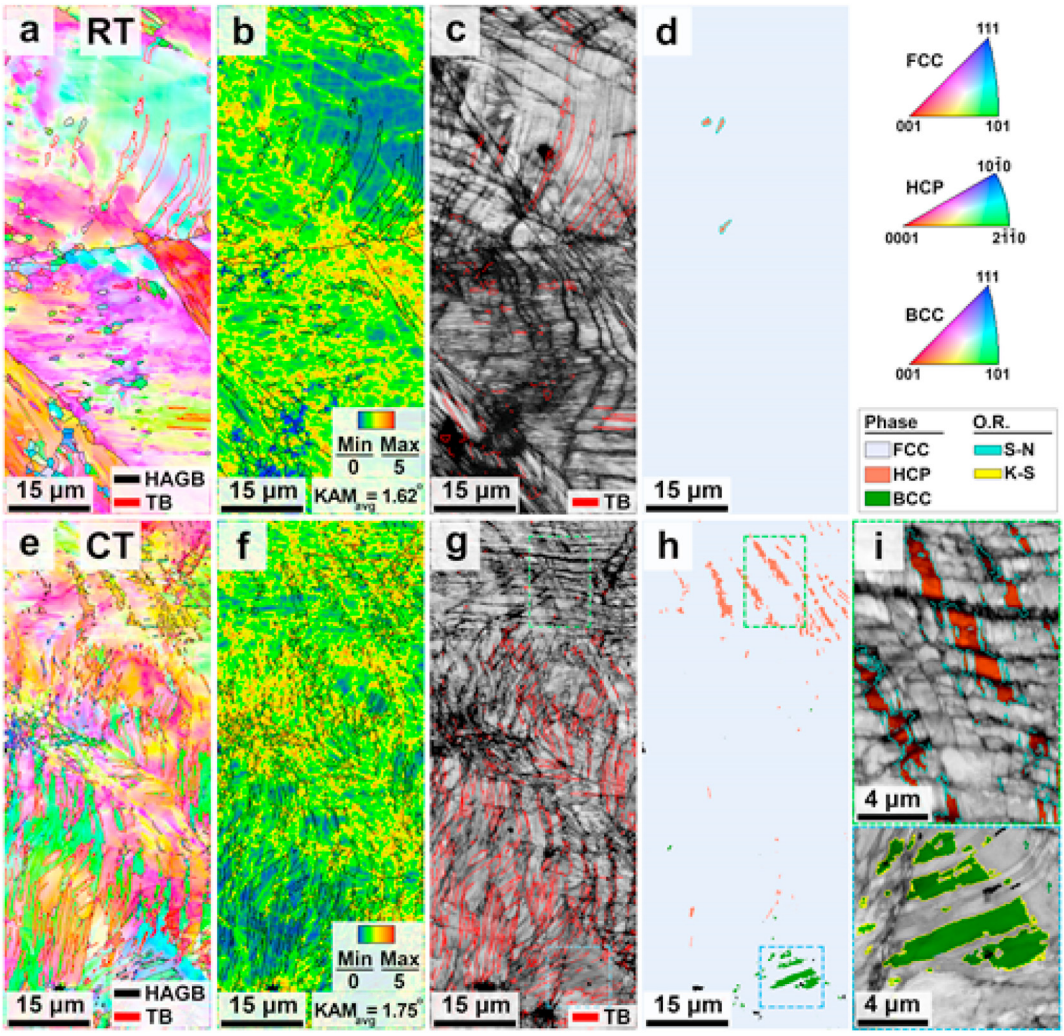

Fig. 3 – Electron back-scatter diffraction (EBSD) inverse pole figure (IPF) (a, e), kernel average misorientation (KAM) (b, f), image quality (IQ) (c, g), and phase distribution (d, h, i) maps of CoCrFeNiMn HEA after a quarter turn HPT at (a–d) room temperature (RT) and (e–i) cryogenic temperature (CT). High-angle grain boundaries (HAGB) and twin boundaries (TB) are shown in the IPF, KAM, and IQ images [40].

mode conducted by severe cold shape rolling [34,52]. It is important to note also that the relatively low amounts of excess free volume in materials processed by HPT is due to the imposition of a high hydrostatic pressure which decreases the probability of void or crack formation [53,54].

2.3. *Significance of phase transformations*

Basically, a deformation-induced martensitic transformation is a well-known phenomenon as a deformation mechanism which accommodates strain during heavy and severe plastic deformation in materials with low SFE [41]. The *fcc* to *hcp* phase transformation usually occurs during plastic deformation when the SFE is < 15 mJ m^{-2} [17]. The SFE of the Cantor alloy is ~21 mJ m^{-2} at room temperature and it may reach to ~5–10 mJ m^{-2} at temperatures as low as −196 °C [56]. An *fcc* to *hcp* martensitic transformation was reported in the Cantor alloy under high pressures of >14 GPa and the results revealed an almost complete transition to the *hcp* phase at ~40 GPa [57,58]. The superior strain imposed during HPT, due to applying both high pressure and shear straining, may stimulate a diffusionless transformation in many materials [59–61]. No phase transformation was detected in an earlier investigation after HPT processing of the CoCrFeNiMn HEA under 6–7.8 GPa up to 10 turns at room temperature [31,32]. Nevertheless, an *fcc* to *hcp* martensitic transformation was detected during cryogenic HPT processing under 5 GPa in a non-equiatomic CoCrFeNiMn HEA with a lower SFE (~3.5 mJ m^{-2} [62]) by comparison with the equiatomic CoCrFeNiMn HEA [63]. A further investigations revealed a dual-phase microstructure of *fcc* and *hcp* in the equiatomic CoCrFeNiMn HEA after a high level of straining by HPT processing under 6–7.8 GPa at cryogenic temperatures [64,65].

Other investigations provide a clear demonstration of the formation of the *bcc*-martensitic phase plus the *hcp*-martensitic phase induced by HPT processing under 10 GPa in the Cantor alloy. The microstructures exhibited significant grain refinement and deformation-induced *fcc* to *hcp* and *bcc*

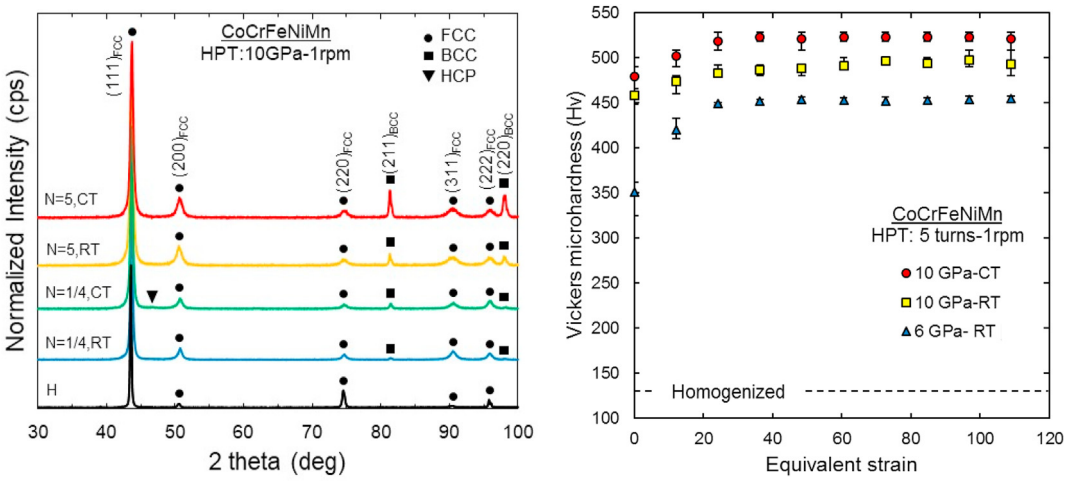

Fig. 4 – (a) X-ray diffraction patterns of the homogenized condition (H) and near the edge of the disks processed by 1/4 and 5 turns HPT at RT and CT and (b) Values of the Vickers microhardness plotted against equivalent strain after processing by HPT through 5 turns at RT and CT [32,40].

martensitic transformations. The *hcp* and *bcc*-martensitic phases formed with Shoji-Nishiyama and Kurdjumov-Sachs orientation relationships, respectively, with the parent *fcc* phase at the early stage of deformation as in Fig. 3 [40]. In addition, X-ray diffraction patterns are shown in Fig. 4(a) which agree with the electron back-scatter diffraction (EBSD) characterization. Additionally, hardness results show that *bcc*-martensite can play an important role in increasing the strength and hardness as documented in Fig. 4(b).

An *fcc* to *hcp* martensitic phase transformation and twinning was reported in the Cantor alloy processed by ECAP at high temperatures and a relatively complicated microstructure was achieved containing dislocations, twins and an *hcp*-phase together with fine grains. These microstructural

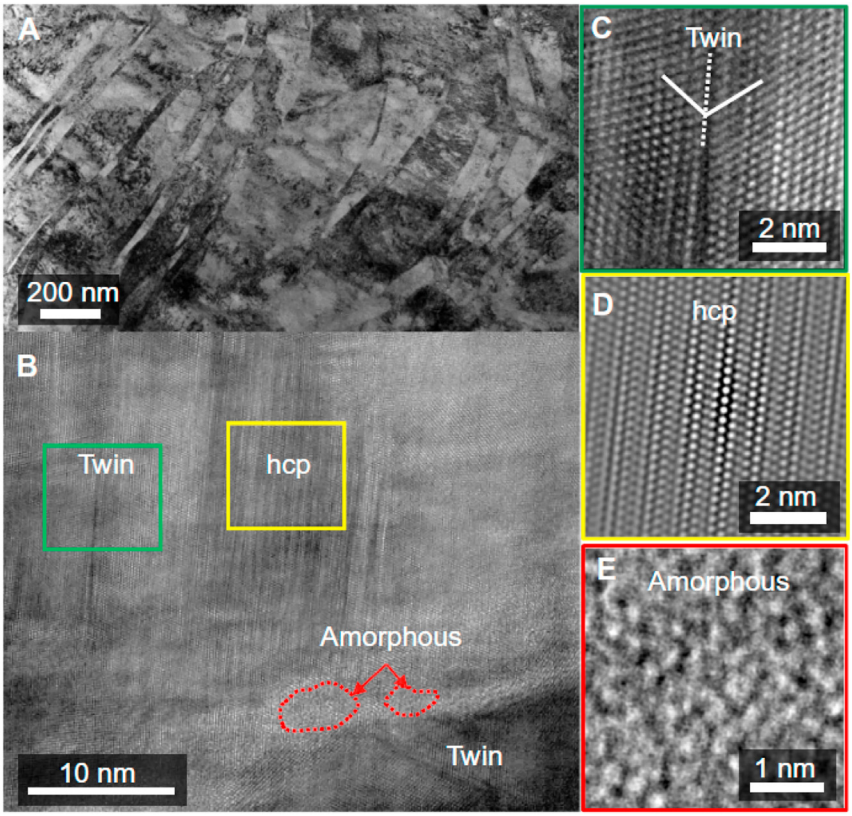

Fig. 5 – Deformation microstructure of the swaged CoCrFeNiMn HEA subjected to quasi-static compression [67].

features provide a strain hardening capability and postpone any necking instability, thereby producing a uniform plastic deformation [66].

The application of SPD through swaging followed by either quasi-static compression or dynamic deformation in shear forms a complex microstructure containing dislocations, stacking faults, twins, an *hcp* phase and nano-size amorphous islands (Fig. 5) [67]. The first three microstructural features were expected even after small and medium amounts of plastic deformation but the *hcp* phase and nano-size amorphous islands were obtained due to the application of SPD. A localized amorphization was proposed as an additional deformation mechanism together with dislocations, deformation twins and martensitic phase transitions after SPD through swaging followed by either quasi-static compression or dynamic deformation in shear at low temperatures [67]. It was proposed that the coordinated propagation of stacking faults and twins along {111} planes generates regions of high deformation which can easily reorganize into *hcp* packets. Increasing the defect density in these regions reaches a critical level and therefore generates islands of amorphous phases as shown in Fig. 5 [67].

The three governing factors promoting the martensitic transformation during deformation are the large amounts of imposed strain/stress, the applied pressure and the deformation temperature (see Fig. 6). The HPT processing provides a high imposed strain and a high pressure. It is well established that Shockley partials are responsible for the nucleation of both twins and the martensitic transformation [68,69]. Thus, the high level of applied strain and the strain rate in SPD methods facilitate the partial separation of dislocations in grains with favorable orientations and this reduces the effective SFE [70,71]. Decreasing the deformation temperature is an effective way for decreasing the SFE that promotes deformation-induced phase transformations in place of dislocation glide and deformation twinning. The activation of the martensitic transformation in the early stage of deformation and the formation of a significant amount of *bcc* phase in the steady-state stage of microstructural refinement shows the importance of the applied pressure and the processing temperature. It is important to note also that the formation of *hcp* and *bcc* phases can play a significant role in the process of phase engineering and strengthening of the Cantor alloy [40]. The general concept is that the formation of martensitic or amorphous phases in the microstructure provides outstanding mechanical properties and improves the strength which then enhances the capability of the Cantor alloy to withstand extreme loading conditions.

2.4. *Warm and Hot deformation*

Understanding the warm and hot deformation mechanisms of the materials during plastic deformation at elevated temperatures is important for determining the optimum conditions to control the grain size and properties. It is well known that deformation mechanisms change by increasing the deformation temperature due to the increasing importance of diffusive processes. Increasing the temperature can change the slip systems and activate deformation along grain boundaries [72]. In addition, the thermal stability in materials containing precipitates or having a deformed microstructure may be affected under exposure at elevated temperatures. Thermo-mechanical treatments via warm or hot deformation are well established procedures that can significantly refine the microstructure by the dynamic recrystallization mechanism.

The microstructural evolution of the Cantor alloy during plastic deformation at elevated temperatures was studied in detail in the temperature interval of 600–1100 °C at different strain rates from 10^{-4} to 10^{-2} s^{-1} and the results showed that the mechanical behavior was different based on whether the deformation was at warm (<800 °C) or hot (>800 °C) temperatures [73]. In the early stage of deformation, the deformation mechanism is planar dislocation glide which is similar to other *fcc* materials regardless of the value of the SFE [11]. High temperature deformation behavior revealed a hardening stage continuously up to the maximum strain during compression of the alloy in the interval of 600–800 °C. Nevertheless, increasing the deformation temperature revealed deformation curves with a well-defined steady-state flow stage following a short hardening stage at the very beginning of deformation in the temperature interval of 900–1100 °C.

The sluggish diffusion [74] or low SFE [62] of the Cantor alloy may significantly affect its dynamic recrystallization behavior. As discussed in section 2.3, a severely distorted matrix is responsible for decreasing the SFE and grain boundary energy so that discontinuous recrystallization and grain growth are hindered. In addition, sluggish diffusion can have an effect on recrystallization and coarsening [18].

It is well known that discontinuous and continuous dynamic recrystallization are two types of mechanisms during deformation at elevated temperatures and they can be distinguished by the characteristics of the deformation behavior and by the nature of the microstructural evolution. Discontinuous dynamic recrystallization produces a grain structure with a decreased dislocation density and this is associated with the formation of nuclei via a bulging

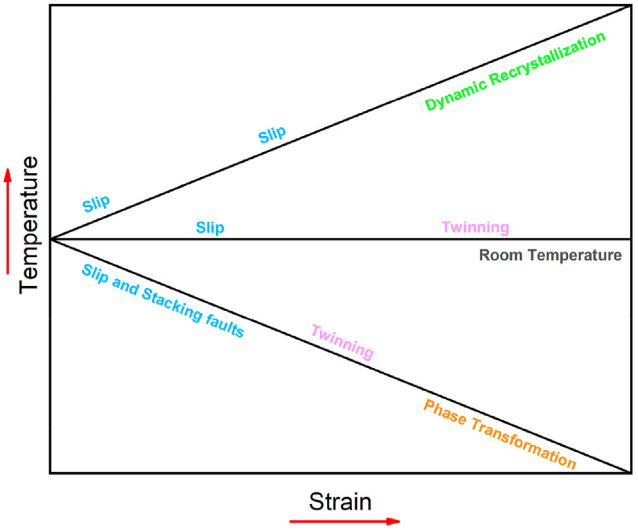

Fig. 6 – Proposed hierarchical deformation mechanism for the CoCrFeNiMn HEA subjected to increasing degrees of deformation at different temperatures.

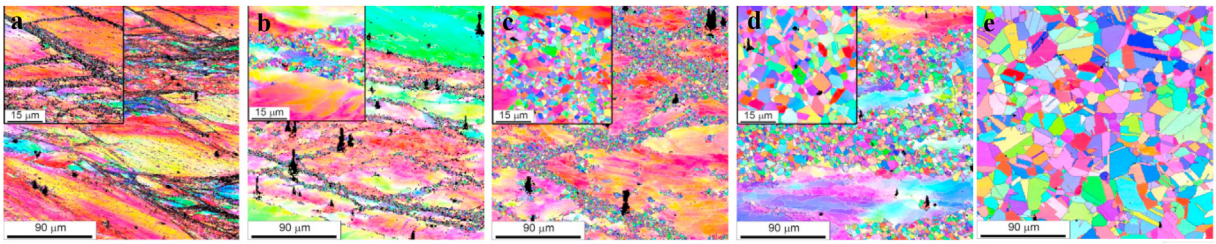

Fig. 7 – EBSD IPF maps of the CoCrFeNiMn alloy after compression at a strain rate of 10^{-3} s^{-1} and a compressive true strain of ~1.4 at different temperatures of (a) 600, (b) 700, (c) 800, (d) 900 and (e) 1000 °C [73].

mechanism followed by growing to consume the deformed matrix. However, continuous dynamic recrystallization consists of the formation of a stable network of low-angle grain boundaries (LAGBs) that is followed by their gradual transformation into high-angle grain boundaries (HAGBs) upon straining [72]. Dynamic recrystallization in the CoCrFeNiMn HEA during plastic deformation in the warm interval mainly appeared in the form of adiabatic shear bands. However, during deformation in the hot interval a discontinuous dynamic recrystallization appeared throughout the material [73]. Accordingly, the volume fraction of the recrystallized structure of 0.085 reaches to the significant value of 0.95 by increasing the deformation temperature from 600 to 1000 °C as demonstrated in Fig. 7.

It is important to note that the recrystallized grain size increased from 0.2 to 40.4 μm for deformation temperatures of 600–1100 °C [73]. In addition to the deformation mechanisms within these two temperature intervals, the measured activation energies for the hot and warm intervals were ~291 and ~213 kJ mol^{-1}, respectively. An activation energy of ~321.7 kJ mol^{-1} was proposed earlier for grain growth in the Cantor alloy [75]. The process can be controlled in turn by diffusion of Ni with an activation energy of 317.5 kJ mol^{-1} which is the slowest element in the Co–Cr–Fe–Mn–Ni alloy system [74]. An activation energy of ~330 kJ mol^{-1} was determined during tensile testing at a temperature of ≥1023 K and strain rate of $>10^{-5}$ s^{-1} and this value lies within the range of the above reported values [76]. Dynamic recrystallization in the CoCrFeNiMn HEA was also observed in other investigations during hot deformation at various temperatures ranging from 800–1000 °C and at different strain rates from 10^{-3} to 1 s^{-1}. The apparent activation energy was estimated as ~350 kJ mol^{-1} for the hot deformation and this is comparable to the activation energy for diffusion of the slowest diffusing element of Ni in this alloy. This gave fairly fine recrystallized grain sizes at high temperatures which are consistent with sluggish diffusion in the HEA [77].

Very recently, the deformation mechanisms of the CoCrFeNiMn HEA were investigated at the elevated temperature of 800 °C and it was suggested that the presence of both a concentrated solid solution and forest dislocations effectively controlled the high temperature plastic deformation [78]. It is well established that the flow behavior in the Cantor alloy is controlled by a combination of a rate-dependent Hall-Petch strengthening, solid solution hardening and forest dislocation hardening and these strengthening mechanisms are generally similar to conventional alloys [79]. The high temperature deformation mechanisms in the CoCrFeNiMn HEA are controlled by dislocation-lattice interactions due to concentrated solid solution hardening and dislocation-dislocation interactions due to the forest dislocation hardening. Transmission electron microscopy (TEM) observations confirmed these mechanisms due to the presence of extensive lattice pinning and dislocation junctions in the microstructure. This clearly shows a suppression of recovery and other diffusion-related mechanisms such as subgrain boundary formation and solute atmosphere migration due directly to the pinning effect of the concentrated solid solution matrix at elevated temperatures as in Fig. 8 [78]. It was suggested, therefore, that the plastic deformation theories for the CoCrFeNiMn HEA at room and cryogenic temperatures may be directly extended to elevated temperatures [80].

3. Grain refinement

3.1. *Fine-grained microstructures*

The thermomechanical processing, including cold working followed by annealing or plastic deformation at a controlled elevated temperature, is a typical procedure for achieving fine-grained materials. Refining the grain size to the range of fine and ultrafine grains leads to an enhancement in the strength level [13,55,81]. However, it is important to note that refining the grain size in the CoCrFeNiMn alloy to the range of fine and ultrafine grains led to only a minor improvement in strength [13,55,81] such that even a fine-grained CoCrFeNiMn HEA exhibited a low yield strength at room temperature [13,40]. Mechanical twinning as a deformation mechanism plays a significant role in the evolution and/or refinement of the microstructure in the CoCrFeNiMn alloy during cold working [21]. Moreover, the large plastic deformation due to heavy cold rolling produces a submicrometer cell structure characterized by the presence of dense shear bands in the HEA [18]. In order to reach the desired ductility in the deformed material, a subsequent annealing heat treatment is necessary. Annealing at >800 °C leads to grain refinement by comparison with the pre-deformation condition in the CoCrFeNiMn alloy and increasing the annealing temperatures significantly increases the fraction of Σ3 boundaries that forms in the

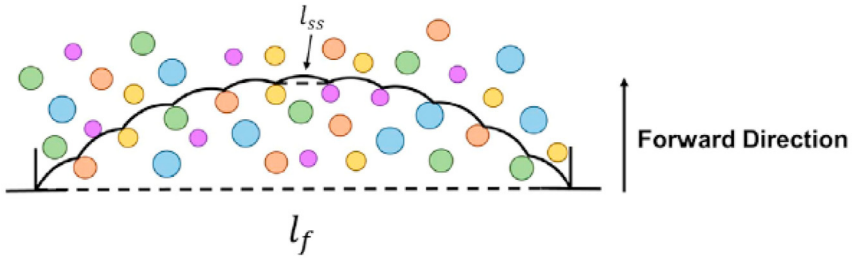

Fig. 8 – Schematic of the dislocation configuration applied to separate the contributions of solid solution hardening and forest dislocation hardening. The values of the spacing between two adjacent pinning points for the two mechanisms are l_{ss} and l_f, respectively [78].

recrystallized microstructure [18]. However, this is accompanied by a decrease in the fraction of HAGBs while the fraction of LAGBs remains almost unchanged. This is reasonable because of the much higher energy of the HAGBs compared with the Σ3 boundaries [18].

The recrystallization temperature in metals is usually ~0.5T_m where T_m is the melting temperature in degrees Kelvin [72]. Accordingly, it is anticipated that the recrystallization temperature in the CoCrFeNiMn HEA should be ~500 °C. However, there are many reports confirming recrystallization at higher temperatures of the order of ~800 °C [11,18,32,40]. This behaviour was attributed to the severely distorted matrix which decreases the dislocation energy, the SFE and the grain boundary energy that hinder discontinuous recrystallization and grain growth [18]. It then becomes more difficult for dislocation motion in the HEA due to its severely distorted crystal lattice which significantly affects the recrystallization process [75]. In addition, the sluggish diffusion can have a significant effect on recrystallization and coarsening [18].

Medium to large plastic deformation, such as 61–96% cold rolling followed by annealing at 800 °C for 1 h, leads to a single-phase microstructure with complete recrystallization and no variation in grain size (~4–5 μm). Nevertheless, partial recrystallization occurs after annealing at the same temperature but with a smaller prior plastic deformation such as 21–41% by cold rolling [13]. Increasing the annealing temperature from 800 to 1200 °C for 1 h after ~87% cold rolling led to grain growth from ~4.4 to ~150 μm [11]. It was reported that coarsening in the CoCrFeNiMn HEA exhibits a classical power-law behaviour with an exponent of 3 which suggests that the grain boundary motion is controlled by a solute-drag mechanism [75] (see Table 2).

The variation of hardness with grain size, as defined by the Hall–Petch relationship, is shown in Fig. 9(a) for the fine-grained CoCrFeNiMn HEA. The hardening coefficient of this HEA is larger than the upper-bound value obtained in conventional *fcc* metals (677 vs. 600 MPa $\mu m^{-0.5}$) [75]. The effect of grain size on the YS in the CoCrFeNiMn HEA was reported in several studies as also illustrated in Fig. 9(b) [11,81,82]. The consequent Hall-Petch relationship of YS = $508D^{-0.5}$ + 183 is true in a broad range of grain sizes from ultrafine (<1 μm) to coarse-grained (>100 μm) [83]. It is worth nothing also that the Hall-Petch strengthening coefficient of the CoCrFeNiMn HEA in this presentation (~508 MPa $\mu m^{0.5}$) is less than for conventional materials such as 304 L and 316 L stainless steels (558 and 546 MPa $\mu m^{0.5}$, respectively) [84]. Table 3 and Table 4 summarize, respectively, the reported Hall-Petch parameters and the effect of different annealing conditions on tensile properties in the CoCrFeNiMn HEA.

3.2. *Ultrafine/nano grained microstructures*

Experiments show that even by refining the grains to a size of ~1 μm it was not possible to improve the YS in the CoCrFeNiMn HEA to more than ~600 MPa, [13,32]. However, with a grain size of <0.1 μm an exceptional strength of >1 GPa was achieved at room temperature [31,32]. It was confirmed that a recrystallized microstructure with a grain size between 0.1 and 1.0 μm revealed an excellent balance of strength and ductility. Thus, an ultrafine-grained Cantor alloy with an average grain size of ~0.5 μm gave a YS and ductility of ~0.89 GPa and ~20%, respectively [55,81]. Deformation twinning is responsible for significant grain refinement in this HEA during plastic deformation [22,23,32]. Nevertheless, it was reported that grain

Table 2 – The grain size, *d*, dislocation density, ρ, Vickers microhardness, YS, UTS, and elongation to failure (δ) of the CoCrFeNiMn HEA after heavy and severe plastic deformation.

Processing	Equivalent strain	*d* (nm)	ρ (cm^{-2})	Hv	YS (MPa)	UTS (MPa)	δ (%)	Ref.
Homogenized	0	–	–	135 ± 4	240	500	90	[32]
ECAP-1st pass	~1	160	3.5×10^8	260 ± 8	670	770	55	[33]
ECAP-2nd pass	~2	130	8.1×10^8	285 ± 3	810	890	45	[33]
ECAP-4th pass	~4	100	1.3×10^9	315 ± 3	980	990	35	[33]
HPT	>40	<50	–	455 ± 15	1400	1740	4	[32]
Cold rolled (>90%)	~4	130	–	–	1199	1335	5	[55]
Cold drawn	1.4	–	–	–	–	1330	6	[25]
Cold shape rolled (>90%)	4.2	50	2.1×10^{11}	450 ± 10	–	–	–	[52]

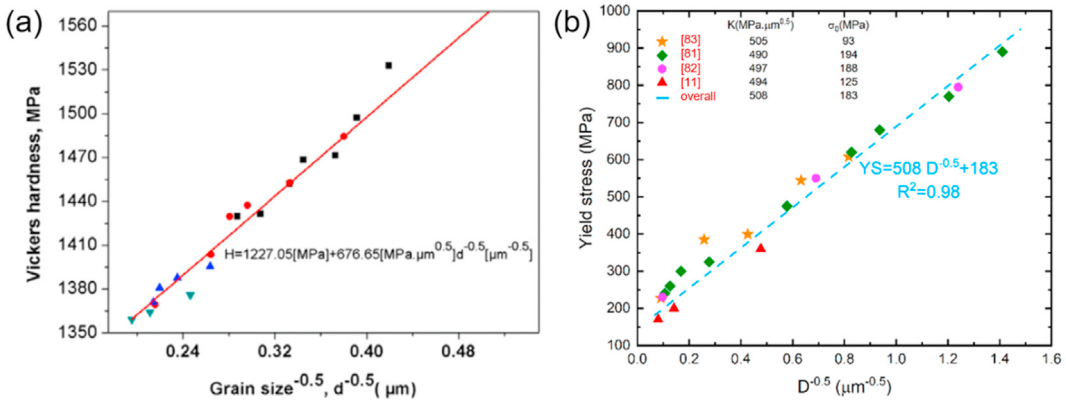

Fig. 9 – (a) Hardness as a function of grain size in the CoCrFeNiMn HEA [75] and (b) yield stress as a function of grain size to develop a general Hall-Petch relationship for the CoCrFeNiMn HEA alloy [11,81–83].

refinement suppressed the formation of deformation twinning by increasing its critical activation stress. Specifically, deformation twinning was observed clearly at a grain size of >3 μm after tensile testing but it was not detected when testing with an ultra-fine grain size of ~0.5 μm [23].

The effect of refining to an ultrafine grain size on the properties of HEAs was studied through the use of HPT, ECAP, severe cold rolling, and cryogenic rolling at −196 °C [13,21,32,33,75,87]. In practice, HPT and ECAP are the most important and well known techniques for using SPD to achieve significant grain refinement where HPT processing provides a procedure for tuning the structures of the materials to attain a nano-grain structure in a manner that is not possible using conventional processing techniques [42]. It was reported that HPT processing leads to a significant incremental increase in the YS, up to ~1400 MPa, at the expense of a decreased ductility with a total elongation lower than 5% in the CoCrFeNiMn HEA after imposing an equivalent strain of >20 [32]. However, the Cantor alloy was processed by four passes of ECAP at 400 °C and showed a YS of ~1 GPa with an elongation to failure of ~35%. In this condition, the microstructure is single-phase with an average grain size of ~100 nm and a high dislocation density [33]. It is important to note that no decomposition was detected in the microstructures after ECAP due to the sluggish diffusion in the CoCrFeNiMn HEA at 400 °C and the short duration of the process [74,88].

Severe cold rolling is a simple and a very useful method for imposing a remarkable strain in the microstructure and therefore promoting grain refinement. The main advantage of this method is the ability to fabricate rod or wire as a continuous process with a potential for industrial applications [89,90]. It was reported that an 80% reduction of the thickness, with an equivalent strain of magnitude 1.6, by cold rolling gave an increment of YS and UTS up to ~1120 and ~1175 MPa, respectively, with a very low uniform elongation of 1.5% [85].

The CoCrFeNiMn HEA was subjected to shape rolling through equivalent strains of 0.5, 1.1, 1.4, 2.5, 3.7 and 4.2 at room temperature in order to study the microstructural evolution and the formation of excess free volume during SPD. The microstructure of the processed sample taken through an equivalent strain of 4.2 revealed a single *fcc* phase with an average grain size of ~50 nm and an excess free volume of ~0.96% due to the formation of nano-voids and defects after severe shape rolling. Microhardness measurements showed a saturation level but there were no nano-voids in the processed samples with equivalent strains less than ~4.2 [34].

An ultrafine-grained structure was also achieved in the CoCrFeNiMn HEA by a twinning-induced grain refinement

Table 3 – Summary of the Hall-Petch relationships at different grain size ranges after cold rolling followed by annealing in the CoCrFeNiMn HEA.

Type	Grain size (μm)	Hall-Petch slope (MPa.μm$^{-0.5}$)	Ref.
YS vs. D$^{-0.5}$	4–160	494	[11]
HV vs. D$^{-0.5}$	3.9–26.1	677	[75]
YS vs. D$^{-0.5}$	0.6–100	497	[82]
YS vs. D$^{-0.5}$	0.5–100	490	[81]

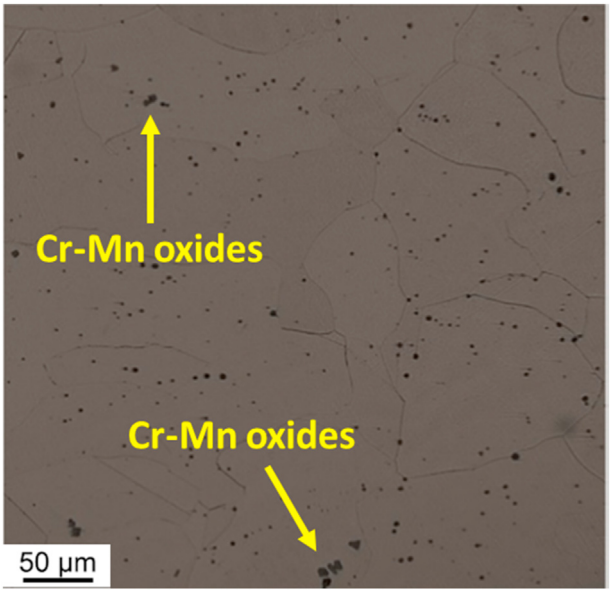

Fig. 10 – A Cr–Mn oxide in a homogenized equiatomic CoCrFeNiMn HEA [32].

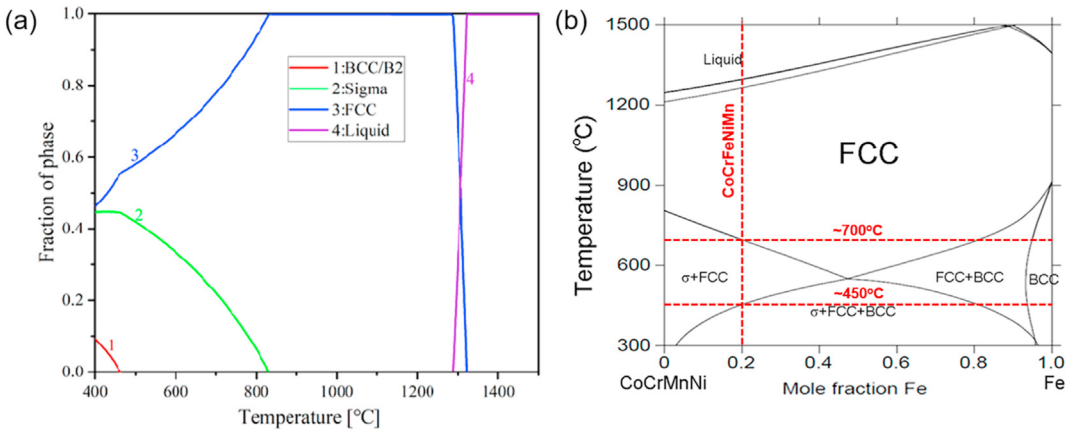

Fig. 11 – (a) Thermo-Calc predictions of the equilibrium phase for the CoCrFeNiMn HEA using TCHEA v2.1 database [99] and (b) phase diagram of $(CoCrMnNi)_{1-x}Fe_x$ HEAs [100].

Table 4 – Summary of the available data on the strength enhancement due to grain refinement.

	Processing	condition	Temperature (°C)	t (min)	Grain size (μm)	UTS (MPa)	YS (MPa)	δ (%)	Ref.
Recrystalization	HPT	5 turn/6 GPa	800	60	4	680	530	80	[32]
				30	–	725	570	78	
				10	–	830	680	65	
			900	60	17	600	370	90	
				30	–	610	390	80	
				10	–	630	410	76	
	Cold Rolling	80%	800	60	3.6	735	425	52.5	[85]
			900	60	17.1	630	270	60.5	
	Cold Rolling	90%	800	60	10	700	–	60	[86]
			900	60	20	650	–	63	
	Cold Rolling	95%	800	60	4.6	736	495	38.7	[55]
			900	60	13.5	673	367	42.6	
			1000	60	22.4	619	291	43.2	
			1100	60	30.6	599	259	45.1	

mechanism after large plastic deformation up to an equivalent strain of $\varepsilon = 1$ applied by cryogenic multi-pass caliber rolling. This procedure led to significant grain refinement and a high strength of >1 GPa but with almost no uniform elongation [89].

The HEA showed ultra-high strength together with a superior ductility after large plastic deformation applied by

Table 5 – Summary of the microstructural and crystallographic results obtained from the matrix and precipitates.

Phase	Major element	Crystal structure	Lattice parameter (nm)			Nucleation site	Morphology
			a	b	c		
Bcc	Cr	*bcc*	0.288	–	–	Grain boundary/inclusion/pores [95] Shear bands [101] Dislocation walls [101] Deformation twins [101]	Fine spherical [87]
Sigma	Cr	Tetragonal (*TCP*)	0.879	–	0.455	Grain boundary/inclusion/pores [95]	Blocky/faceted [95] Rectangular [87]
NiMn	Ni & Mn	Tetragonal ($L1_0$)	0.261	–	0.349	Grain boundary/inclusion/pores [95] Shear bands [101] Dislocation walls [101] Deformation twins [101]	–
FeCo	Fe & Co	Cubic (*B2*)	0.285	–	–	Grain boundary/inclusion/pores [95] Shear bands [101] Dislocation walls [101] Deformation twins [101]	–
Matrix	–	*Fcc*	0.360	–	–	–	–

Table 6 – Summary of the chemical analysis (at.%) of precipitates in the CoCrFeNiMn HEA.

Precipitate	Method	Co	Cr	Fe	Ni	Mn	Ref.
Bcc	TEM EDX	3.6	86.3	5.2	0.6	4.3	[95]
	TEM EDX	14.62	42.26	16.88	12.66	13.58	[52]
Sigma	SEM EDX	19.0	26.0	20.0	16.0	19.0	[34]
	TEM EDX	18.1	46.8	16.9	5.7	12.5	[95]
	APT	18.2	46.0	17.1	6.7	12.3	[95]
	TEM EDX	16.2	43.8	17.6	7.8	14.6	[85]
NiMn	TEM EDX	3.6	1.9	2.2	54.9	37.4	[95]
	APT	3.9	2.3	1.2	50.6	42.0	[95]
FeCo	TEM EDX	45.9	2.0	46.0	0.6	5.5	[95]

asymmetric rolling, with a total rolling reduction of 92% followed by post-deformation annealing [91]. Improved mechanical properties were reported in the processed alloy by asymmetric rolling by comparison with the conventional symmetric rolling. It was claimed that an ultra-high strength was obtained due to the formation of fine grains and a high back-stress and the superior ductility was due to a gradient structure and fine grains in the annealed sample [91].

The nanocrystalline HEA demonstrates an exceptionally high strength of ~3 GPa at the very low temperature of 4.2 K whilst maintaining reasonable plasticity at this temperature. The generation of dislocations from the grain boundaries and a transition to the grain interior was the proposed deformation mechanism in the nanocrystalline CoCrFeNiMn HEA [92].

4. Precipitation hardening

4.1. *Decomposition and formation of precipitates*

It is well established that the CoCrFeNiMn HEA has a single-phase *fcc* solid solution structure in the as-cast and homogenized conditions [93,94]. However, microstructural studies revealed the formation of a few volume fractions of a Cr–Mn oxide (~0.1%) in the microstructure as inclusions as illustrated in Fig. 10 [13,26,28,32,76,95–98].

A phase diagram calculation of an equiatomic CoCrFeNiMn HEA by Thermo-Calc is presented in Fig. 11 (a) [99]. These calculations predict the formation of sigma and *bcc/B2* phases at <460 and < 820 °C, respectively. Another calculated phase diagram using Thermo-Calc between the quaternary CoCrNiMn HEA and Fe shown in Fig. 11(b) suggests the formation of

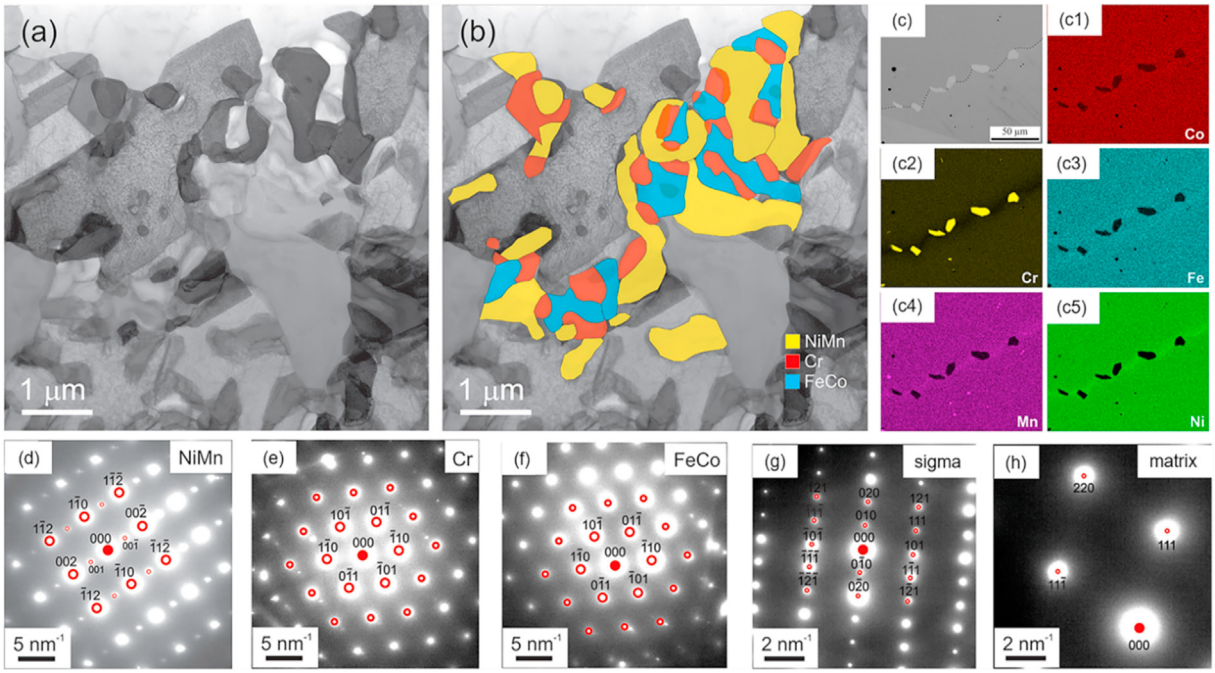

Fig. 12 – (a) STEM BF contrast reveals the presence of several secondary precipitates in a grain boundary of the CoCrFeNiMn HEA, (b) EDX maps superimposed on the image in (a) show that the precipitates have three distinct chemical compositions after a 500 °C anneal for 500 days, (c) microstructure and EDS-map of the CoCrFeNiMn HEA after 500 days annealing at 700 °C, (d, e, f, g, h) corresponding SAD images on which the simulated diffraction patterns (red circles) are superimposed for NiMn, *bcc* Cr-rich, FeCo, sigma and matrix phases, respectively [95].

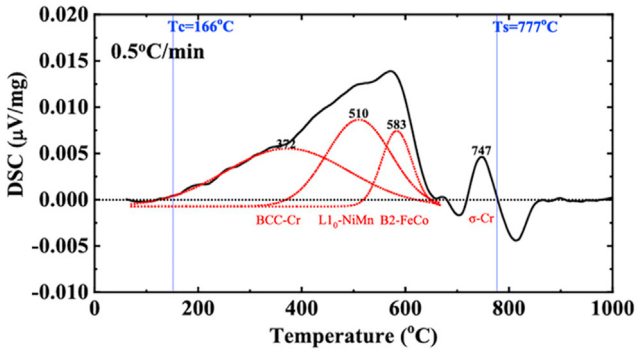

Fig. 13 – DSC curves of CoCrFeNiMn HEA at a heating rate of 0.5 °C.min^{-1} [102].

the sigma-phase over a wide range of chemical compositions [100]. These predictions demonstrate the formation of sigma and *bcc* phases in the Cantor alloy from room temperature to ~450 °C. The sigma precipitates are stable in the temperature range of ~450–~700 °C wherein the *bcc* precipitates are dissolved. The present calculations clearly show the stability of the *fcc* single-phase solid solution at elevated temperatures (>~700 °C).

The decomposition and formation of new phases in the *fcc*-matrix phase was reported earlier in the Cantor alloy after annealing within special temperature ranges [95]. It was suggested that Cr promotes the formation of a *bcc* phase. Based on thermodynamic calculations, the solubility of Cr in the *fcc* phase is quite high at high temperatures but decreases at low temperatures and this makes possible the formation of a Cr-rich *bcc* phase. It was shown experimentally that the CoCrFeNiMn alloy has a single-phase *fcc* structure above 800 °C while a mixture of *fcc* and *bcc* phases, or under some conditions a sigma phase with a tetragonal crystal structure, forms below this temperature [32].

The decomposition behavior was studied in a homogenized CoCrFeNiMn HEA using a long-term annealing of 500 days at intermediate temperatures of 500 and 700 °C [95]. A multitude of precipitates including Cr-rich *bcc*, FeCo (*B2*), and NiMn ($L1_0$) with complex morphologies were distributed at the grain boundaries as in Fig. 12. These precipitates dissolved at 700 °C and Cr-rich sigma precipitates with a tetragonal structure formed at the grain boundaries as in Fig. 12(c) [95].

A summary of the microstructural features and crystallographic information on the matrix and the precipitates is shown in Table 5. It is important to note that these phases were detected in the CoCrFeNiMn HEA subjected to SPD after

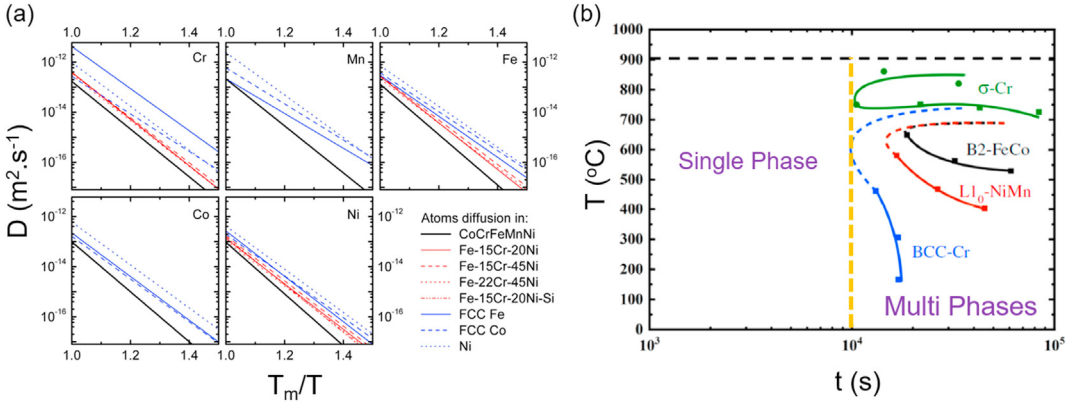

Fig. 14 – (a) Temperature dependence of the diffusion coefficients for Cr, Mn, Fe, Co and Ni in. Different alloys [103] and (b) Schematic TTT diagram for CoCrFeNiMn HEA [102].

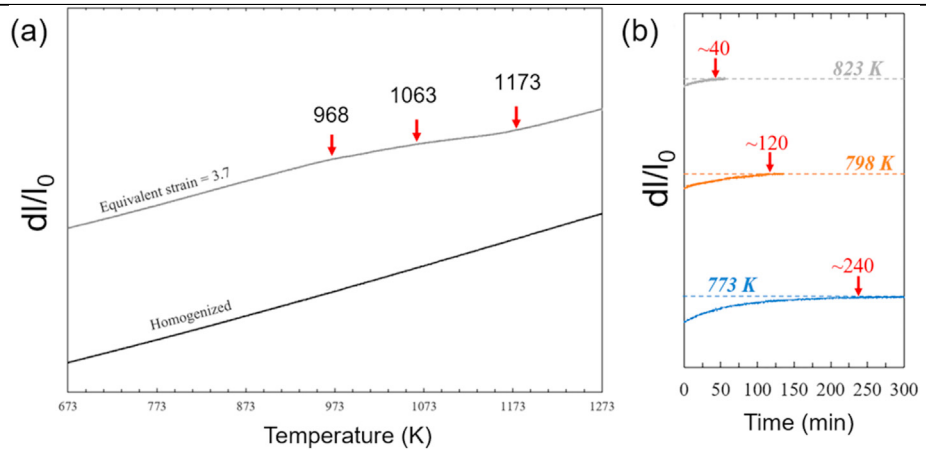

Fig. 15 – (a) Relative length changes of CoCrFeNiMn samples before and after SPD [52] and (b) Isothermal dilatometric measurements at 500, 525 and 550 °C after SPD [104].

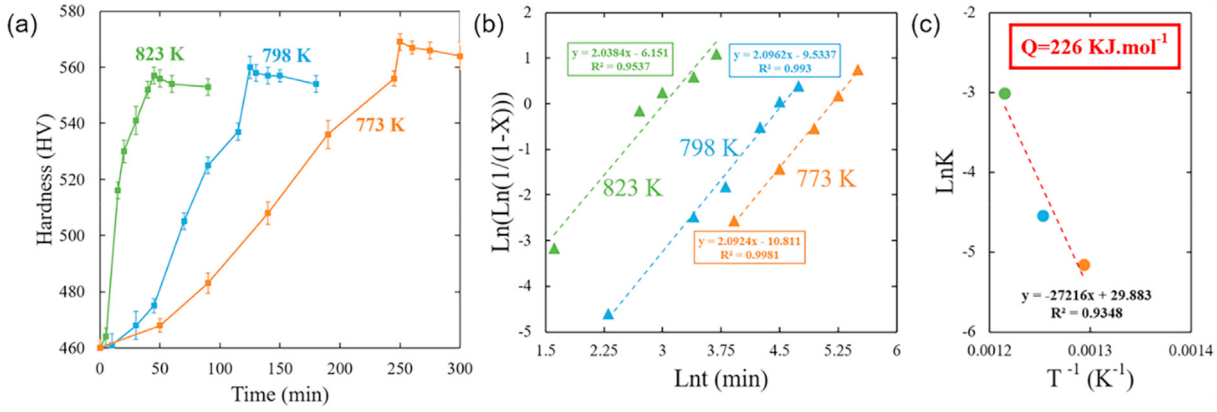

Fig. 16 – (a) The hardness value of SPD samples after annealing at 500, 525 and 550 °C for different holding times [104], (b) The JMAK curve to obtain the K parameter based on the volume fraction of the *bcc* Cr-rich phase formation (X) calculated according to the hardness results [104] and (c) Calculation of the activation energy for *bcc* Cr-rich precipitation [104].

Table 7 – Summary of the temperature range of sigma and *bcc* precipitates in different conditions.

Condition	*bcc* Cr-rich		Sigma Cr-rich		Ref.
	T_s (°C)	T_f (°C)	T_s (°C)	T_f (°C)	
HPT	200	800	600	700	[32]
ECAP	–	–	500	700	[33]
Shape Roll	450	750	650	850	[52]
Cold Roll	500	700	600	800	[85]
Cold Roll	600	700	600	800	[87]
Homogenized	200	700	700	900	[102]

short-term annealing. It appears that the severely-deformed structure of the processed HEA facilitates the phase decomposition due to the large numbers of defects and grain boundaries introduced during this process. These defects serve both as fast diffusion pathways and as preferential nucleation sites for the formation of new phases. It is therefore concluded that the application of SPD leads more quickly to the formation of these stable phases [31,32].

Table 6 Summary of the chemical analysis of precipitates of the CoCrFeNiMn HEA using different techniques. The

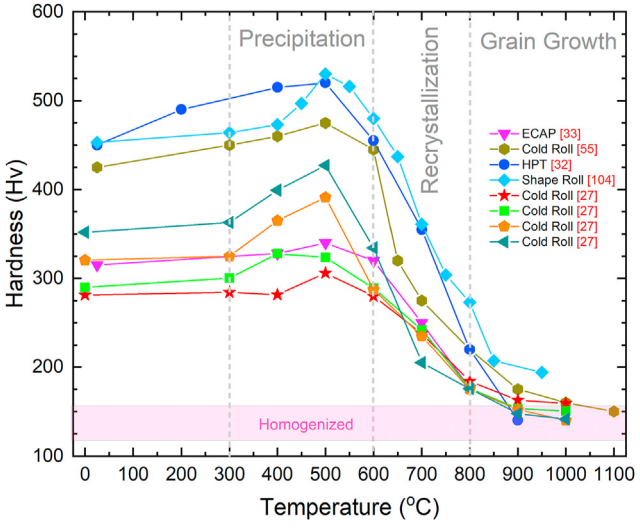

Fig. 17 – Hardness evolution of deformed CoCrFeNiMn HEA by different processes after annealing at different temperatures [27,32,33,55,104].

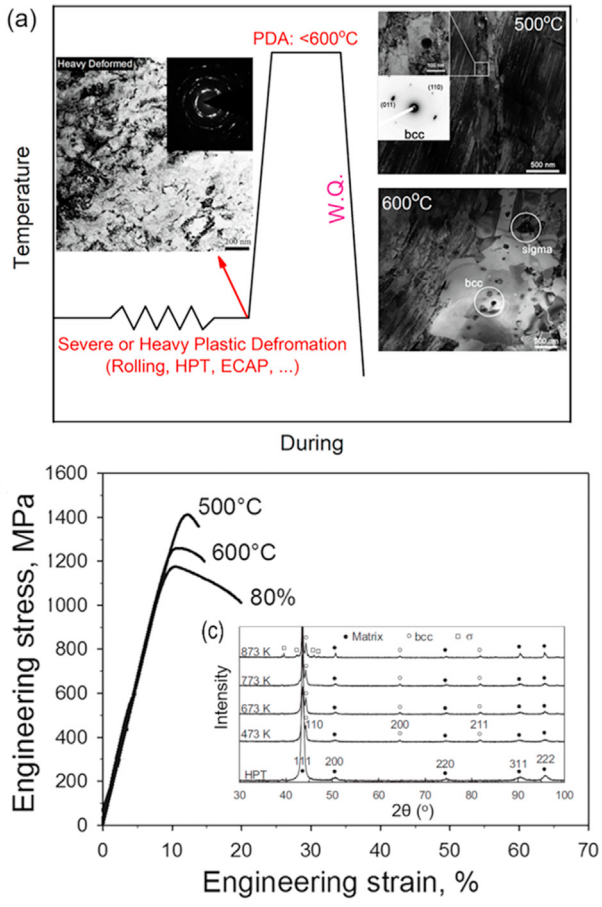

Fig. 18 – (a) Schematic of the process for precipitation to increase strength [34,85], (b) engineering stress versus engineering strain for deformed and annealed CoCrFeNiMn samples [85] and (c) X-ray diffraction pattern for deformed and annealed samples [32].

results show that *bcc* and sigma precipitates are Cr-rich precipitates and NiMn and FeCo phases are near equiatomic.

Figure 13 illustrates the thermal stability of the CoCrFeNiMn HEA using differential scanning calorimetry (DSC) thermal analysis [102]. The results show that there are two exothermic peaks over temperature ranges of ~160–640 °C and ~720–780 °C, respectively. It is apparent that the first exothermic peak is not a simple Gaussian type, suggesting the occurrence of several phase transformations including the formation of *bcc* Cr-rich, NiMn and FeCo precipitates. The later exothermic peak is a simple Gaussian type and represents the formation of the sigma precipitates. It is particularly noted that two endothermic peaks (~700 and ~800 °C) also appear in the DSC curve possibly due to the dissolution of these phases [102].

4.2. *Precipitation kinetics*

Many attempts were conducted to study the precipitation kinetics in the Cantor alloy in order to understand the procedure of microstructure engineering. Fig. 14(a) shows the dependence of the diffusion coefficient on temperature for the Ni, Co, Cr, Fe and Mn elements in different alloys and it confirms that the CoCrFeNiMn HEA has the slowest diffusion coefficient among the various alloys [103]. Generally, precipitation includes two stages containing the diffusion of atoms to achieve the precipitation composition and the change in crystal structure, where the first stage mainly controls the precipitation [104].

Comprehensive experiments showed that the activation energies of diffusion for Cr, Mn, Fe, Co and Ni elements in an homogenized CoCrFeNiMn HEA are 292.9, 288.4, 309.6, 306.9 and 317.5 kJ mol^{-1}, respectively [74]. The highest value for Ni suggests that this element has the lowest diffusion coefficient and therefore it controls the diffusion mechanism in this alloy and also the precipitation kinetics [104]. Accordingly, the slowness of Ni diffusion in the alloy indicates a very slow precipitation. Sluggish diffusion facilitates maintaining the alloy in the supersaturated state and this leads to the formation of fine precipitates during precipitation and a reduced coarsening rate of precipitation [75,105–112]. These advantages are beneficial in controlling the microstructure and providing an improved performance.

A temperature-time-transformation (TTT) diagram of the CoCrFeNiMn HEA is given in Fig. 14(b). The results clearly confirm the formation of different phases over different temperature ranges and this suggests no precipitate formation in a reasonable holding time due to the sluggish precipitation kinetics in this HEA [52,104]. According to the TTT diagram, the alloy will be a single-phase solid solution at cooling rates faster than about 0.076 °C.s^{-1} which can be readily achieved during laboratory-scale casting where the rates usually range from 10 °C.s^{-1} to 100 °C.s^{-1} [102,113,114].

The effect of plastic deformation on the thermal stability in the CoCrFeNiMn HEA is shown in Fig. 15(a) which clearly demonstrates the increasing precipitation kinetics. As expected, the homogenized condition reveals no slope changes in the heating regime which demonstrate the high thermal stability of the alloy in this condition [52,74]. Nevertheless, several slope changes are visible in the severely deformed microstructure due to precipitation, recovery, recrystallization and the dissolution of precipitates [34,52]. This suggests that plastic deformation encourages precipitation within a reasonable annealing time. As already noted, a large number of grain boundaries and dislocations introduced into the microstructure during plastic deformation provide fast diffusion pathways together with preferential nucleation sites for the formation of new phases [31,104]. Fig. 15(b) illustrates isothermal thermal analyses at 500, 525 and 550 °C with a heating rate of 10 °C.min^{-1}. Phase transformations such as recrystallization, grain

Table 8 – Summary of the available data on the increase in strength due to precipitation in different conditions.

Plastic deformation method	Condition	T (°C)	Time (min)	UTS (MPa)	YS (MPa)	Total Elongation (%)	Ref.
ECAP	2 Passes	–	–	810	890	45	[33]
		500	60	850	960	37	
		600	60	820	880	41	
	4 Passes	–	–	980	990	35	[33]
		500	60	1015	1080	30	
		600	60	890	1010	32	
Cold Roll	80%	–	–	1120	1175	14.0	[85]
		500	60	1290	1415	3.6	
		600	60	1135	1260	6.7	
	90%	–	–	1150	1175	6	[86]
		500	60	1300	1300	1	
		600	60	1030	1060	10	
	60%	–	–	1130	1180	14	[101]
		450	1080	1200	1250	4	
		450	2880	1160	1230	6	
	95%	–	–	1200	1335	4.4	[55]
		300	60	1270	1366	1.2	
		400	60	1371	1403	1.6	
		500	60	1363	1471	3.2	
		600	60	1242	1325	4.3	
–	Homogenized	–	–	291	657	55	[124]
		610	21,600	319	680	54	

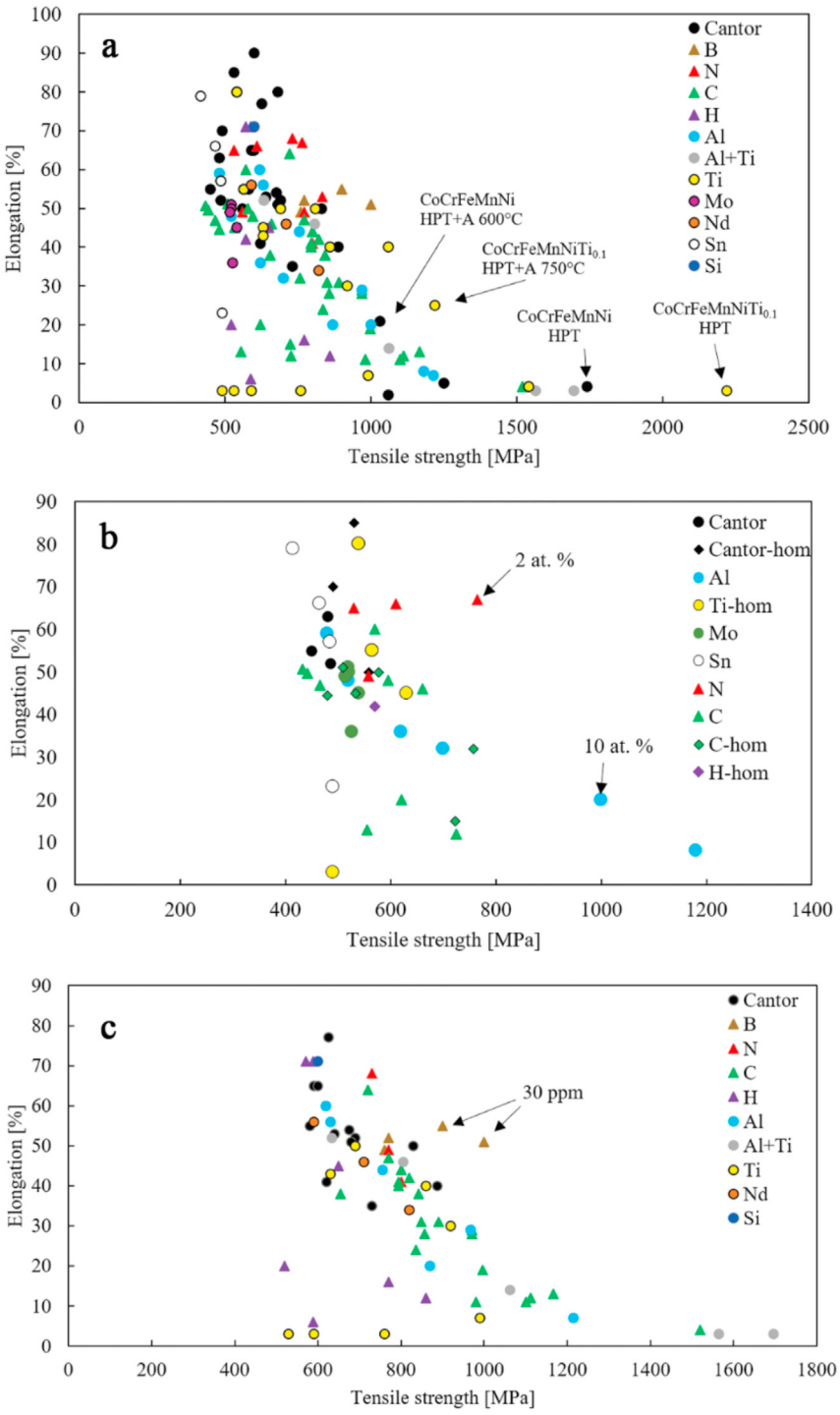

Fig. 19 – (a) Comparing the effect of Al [131,135,136], Ti [129,137–140], Mo [141], Nd [142], Sn [143], Si [140], B [144], N [130,145–147], C [145,148–156], H [157–160] on tensile properties in the Cantor alloy [32,131,140,142,144,145,148–150, 153,155,156,161,162]. As-cast and homogenized (b) and cold-rolled and annealed conditions (c) are also compared separately.

growth and the formation of some precipitates are associated with a decrease in volume or a reversal for some precipitations [52]. The formation of the sigma precipitate with lattice parameters of a~8.8 Å and c~4.5 Å [95,115] and the formation of *bcc* Cr-rich precipitates (a≈2.88 Å [31,32]) in the *fcc* matrix (a≈3.59 Å [34]) lead to a decrease and increase of the volume, respectively. Therefore, this increase in volume indicates the formation of Cr-rich *bcc* precipitates. It was suggested earlier that Cr promotes the formation of a *bcc* phase and the solubility of Cr in the *fcc*-matrix phase decreases with decreasing temperature giving rise to the formation of a Cr-rich *bcc* phase in the CoCrFeNiMn HEA [32].

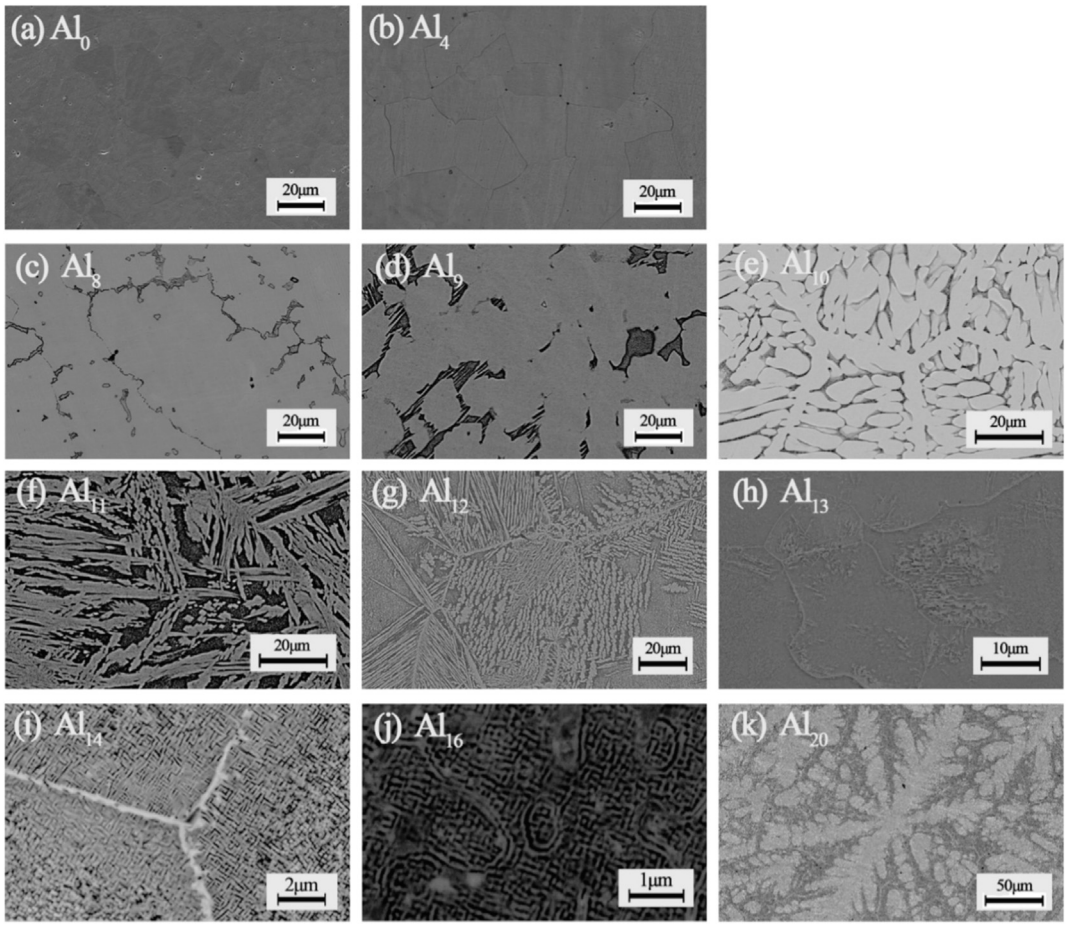

Fig. 20 – The SEM micrographs of the as-cast $(FeCoNiCrMn)_{100-x}$ Al_x alloy (x = 0–20 at. %) [131].

Very recently, precipitation kinetics of mono-crystalline and polycrystalline equiatomic CoCrFeNiMn HEAs were investigated in which the polycrystalline alloy decomposed into multiple phases during 3 min at 700 °C even though the mono-crystalline alloy was stable at the same temperature for 5 h [116]. The philosophy behind this difference in thermal stability relates to the volume fractions of defects and particularly the grain boundaries and triple junctions [117–119]. It was shown that sigma Cr-rich precipitates were formed by hot compression at 700 °C [120]. This suggested that the sigma phase is strongly generated as the recrystallization progressed, thereby implying that the recrystallization process is essential for sigma phase formation in the *fcc* crystal structure. In addition, the sigma Cr-rich phase kinetics are faster in dynamic precipitation conditions than in static precipitation [120].

The kinetics of precipitation were investigated in a severely deformed Cantor alloy using microhardness measurements and the modified JMAK relation [104]. Fig. 16(a) shows the hardness diagram of the severely deformed CoCrFeNiMn HEA versus time at different annealing temperatures. From these results it is concluded that the increase in hardness with increasing annealing time is related to the formation of *bcc* Cr-rich precipitates. From the onset of aging up to the peak of hardness was taken as the precipitation sequence. Therefore, the transformed fraction (X) can be calculated based on the following equation:

$$X = \frac{Hv - Hv_{SPD}}{Hv_{PEAK} - Hv_{SPD}} \tag{5}$$

where Hv, Hv_{SPD}, and Hv_{PEAK} are the measured hardness after annealing, before annealing, and the hardness value at the peak, respectively. It was shown that the modified JMAK relation in the following Eq. (6) may be used to obtain the activation energy of precipitation [104,121]:

$$X = 1 - \exp\left(-Kt^n\right) \tag{6}$$

where *X* is the transformed fraction, *t* is the anealing time, and *K* and *n* are the JMAK coefficient and the exponent parameters, respectively. The following equation can be drived from Eq. (6):

$$Ln\left(Ln\left(\frac{1}{1-X}\right)\right) = nLnK + nLnt \tag{7}$$

A plot of $Ln\left(Ln\left(\frac{1}{1-X}\right)\right)$ versus Lnt is shown in Fig. 16(b) where the slope and the intercept of each plot are equal to *n* and *nLnK*, respectively. Therefore, the values of *K* can be determined directly. The *K* parameter has an exponential relationship with the annealing temperature as given by:

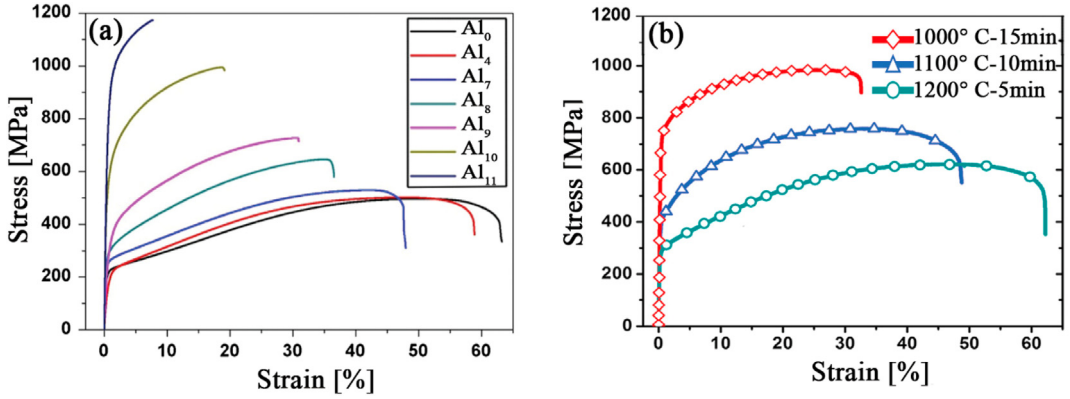

Fig. 21 – Engineering stress-strain curves of (a) as-cast $(FeCoNiCrMn)_{100-x}$ Al_x alloys at room temperature [131] and (b) cold-rolled $Al_{0.5}$CoCrFeNiMn alloy after annealing under different conditions [135].

$$K = K_0\, exp(-Q/RT) \tag{8}$$

where T is the annealing temperature in degrees Kelvin, R is the gas constant and Q is the activation energy. The value of Q was determined as ~226 kJ mol^{-1} in Fig. 16(c). The n value at 500–550 °C was ~2 which suggests that the grain edge nucleation mechanism may be a possible mechanism according to the strain applied to the material [104,122]. The activation energy of the *bcc* Cr-rich precipitation, obtained in the severely deformed sample, is less than the activation energy of diffusion for different elements in the homogenized CoCrFeNiMn HEA [74]. The reason for this difference lies in the presence of many defects, including dislocations and non-equilibrium grain boundaries [32]. It is worth noting that the value obtained for the activation energy of *bcc* Cr-rich precipitates is approximately equal to the value for the activation energy for grain boundary diffusion in nickel [123]. This suggests that the *bcc*-Cr rich precipitation is controlled directly by grain boundary diffusion of Ni [104].

Table 7 shows the temperature range of sigma and *bcc* precipitate formation under different conditions. It is apparent that there are several discrepancies between the results. For example, no *bcc* Cr-rich precipitates were reported in an ECAP-processed sample after annealing [33] but data suggest the *bcc* Cr-rich precipitates form and dissolve earlier than sigma Cr-rich precipitates.

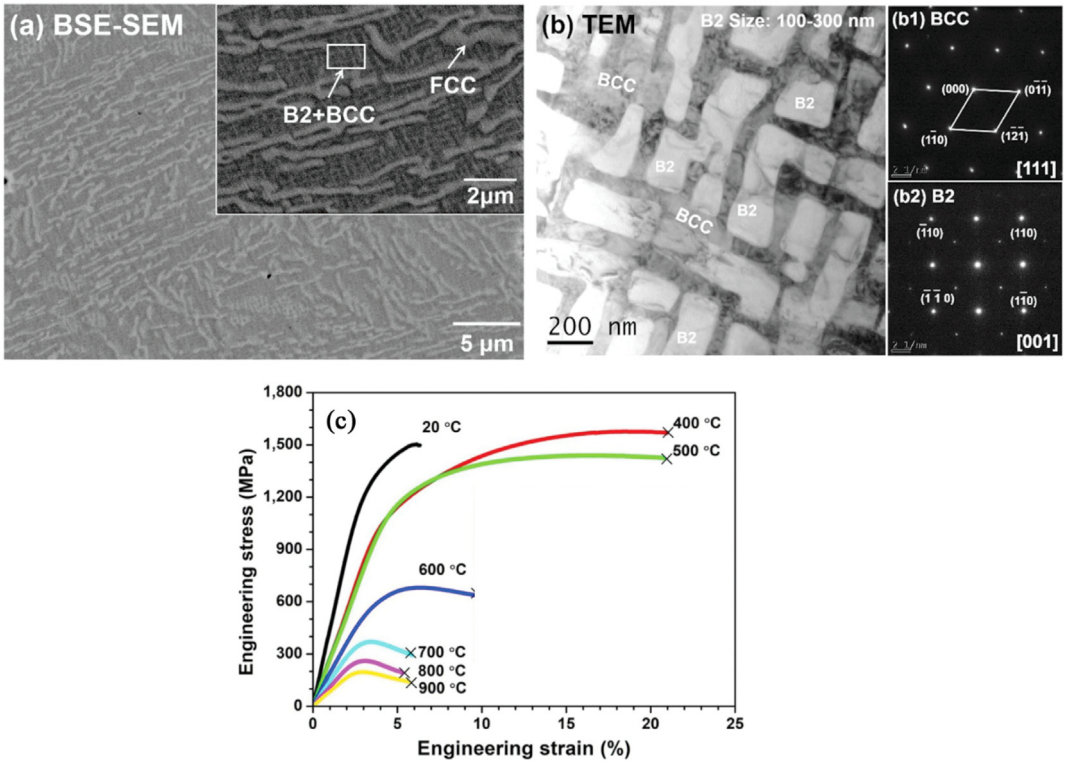

Fig. 22 – The as-cast microstructure (a–b) and the compression engineering stress-strain curves (c) of the $CoCrFeNiMnAl_{0.75}$ alloy at room and elevated temperatures [166].

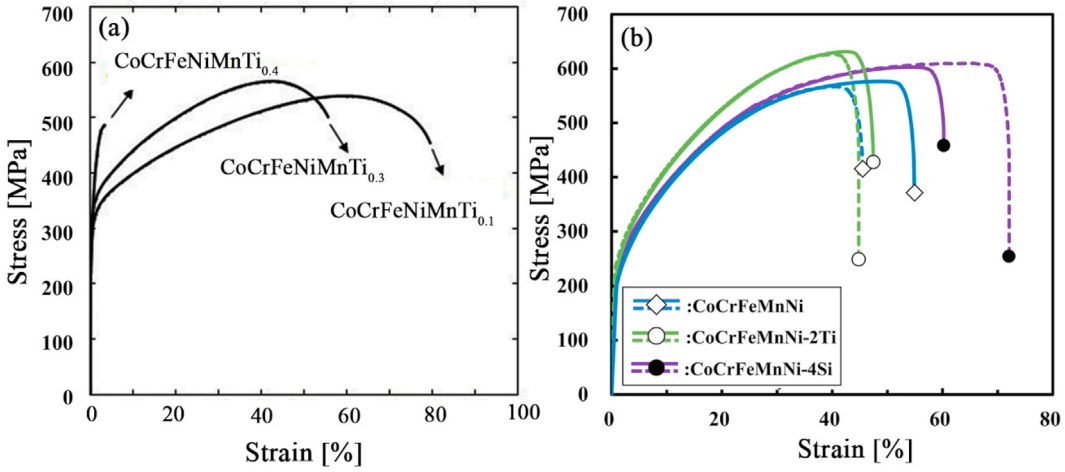

Fig. 23 – The tensile engineering stress-strain curves of (a) homogenized CoCrFeNiMnTi$_x$ (x = 0.1–0.4) alloys [138] and (b) Ti and Si-containing CoCrFeNiMn alloys annealed for 15 min at 1000 °C after homogenization and cold-rolling [140]. Broken curves and solid curves in (b) indicate the results of two different specimens.

4.3. *Significance of precipitation during thermomechanical treatment*

It is expected that the decomposition and formation of precipitates will affect the mechanical properties of the CoCrFeNiMn HEA by increasing the strength and probably also decreasing the ductility. The Cantor alloy may be classified as an age-resistant alloy in which the mechanical properties can be manipulated by controlling the temperature and time of any aging treatment. The production of a well-decorated microstructure in the HEA by different available precipitates is a method for improving the strength with no significant loss of ductility. However, the sluggish diffusion in the Cantor alloy dictates using an artificial aging treatment on the deformed material to increase the kinetics of precipitation within a reasonable time. Accordingly, many attempts were undertaken to study precipitation in the HEA by thermomechanical treatment including deformation followed by annealing. Fig. 17 shows the hardness of the deformed CoCrFeNiMn HEA by different procedures after annealing at temperatures in the range of 200–1000 °C [32,33,55,104]. The results demonstrate that the hardness of the deformed HEA increases slightly after annealing at 500 °C and then decreases rapidly with increasing annealing temperatures up to 1000 °C. At this latter temperature, the hardness is very close to the initial value for the homogenized condition. This behavior clearly suggests that Cr-rich precipitates form at temperatures up to 500 °C with the dissolution of Cr-rich precipitates and recrystallization/grain growth after annealing up to 1000 °C [33,52]. Therefore, the temperature range of ~300–600 °C is recommended for increasing the strength by precipitation.

Figure 18 shows a schematic of the process for precipitation to increase the strength of the CoCrFeNiMn HEA. The required process to increase strength through precipitation strengthening consists of two separate steps: (a) applying heavy straining or SPD and (b) post-deformation annealing at temperatures below 600 °C. The microstructure of the heavily-deformed samples is shown in Fig. 18(a) which demonstrates a typical severely deformed microstructure containing tangled dislocations and grain fragmentations at the

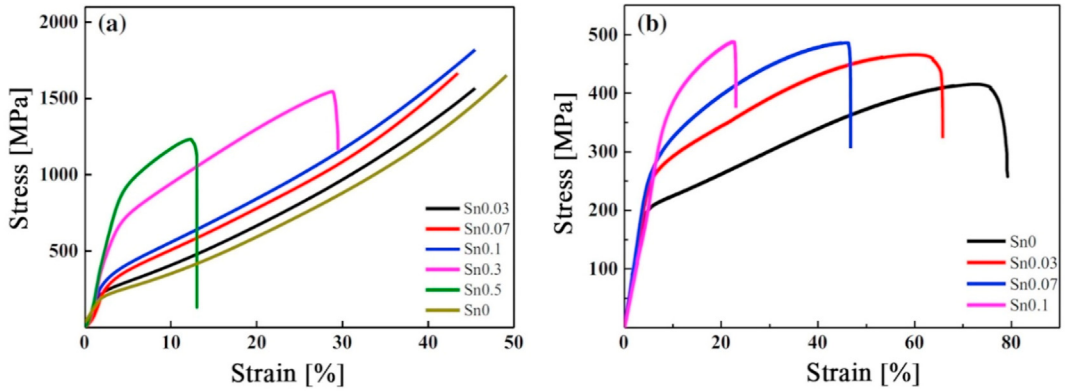

Fig. 24 – (a) Compressive engineering stress-strain curves and (b) tensile stress-strain curves of CoCrFeNiMnSn$_x$ alloys in as-cast condition [143].

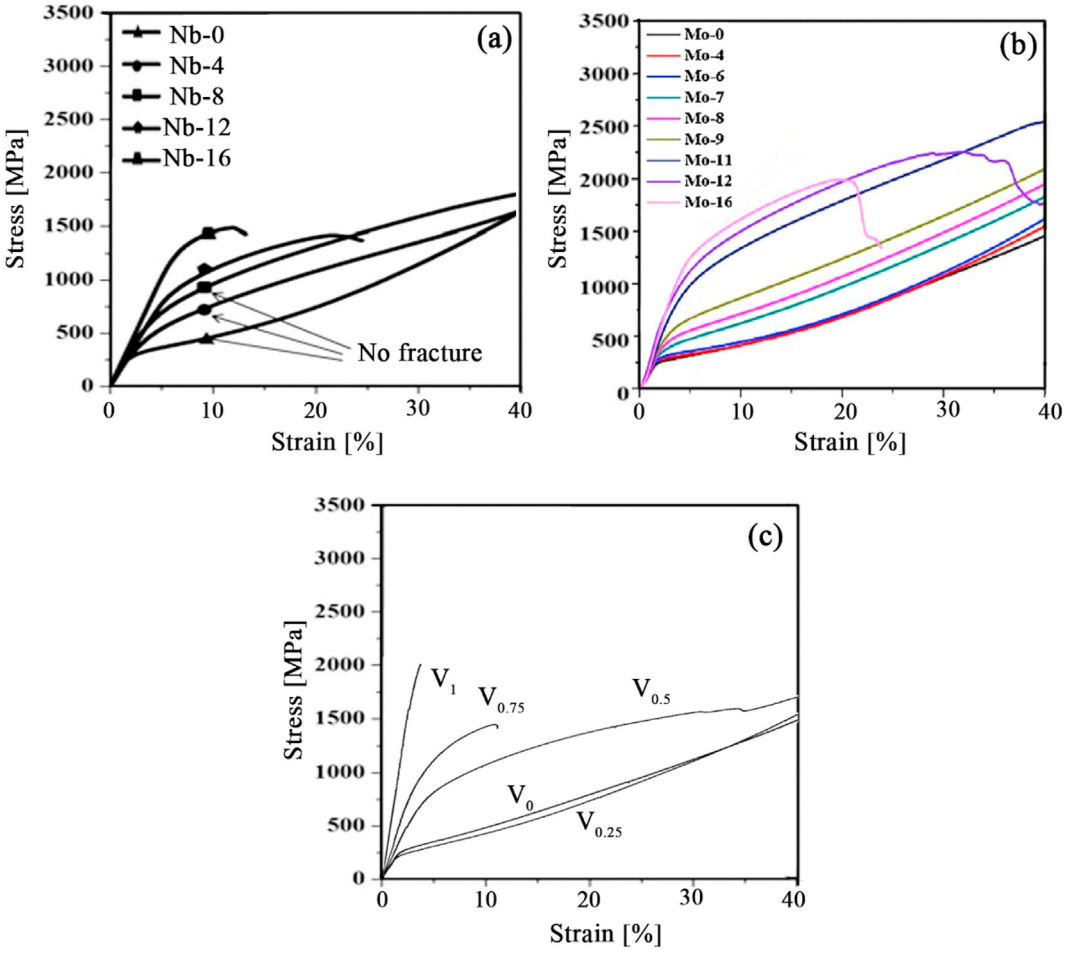

Fig. 25 – The compressive engineering stress-strain curves of (a) $(CoCrFeNiMn)_{100-x}Nb_x$ [134], (b) $(CoCrFeNiMn)_{100-x}Mo_x$ [170] and (c) $CoCrFeNiMnV_x$ [96].

nanoscale [32,34,52]. As already noted, heavy straining or SPD accelerates the precipitation kinetics by introducing many defects such as dislocations, and grain boundaries [94,104]. TEM images show *bcc* Cr-rich precipitates with spherical morphology in a non-recrystallized microstructure and *bcc* Cr-rich and sigma Cr-rich precipitates in a partially recrystallized microstructure after post-deformation annealing at 500 and 600 °C, respectively, as shown in Fig. 18(a) [85]. The results of mechanical testing demonstrate that the formation of Cr-rich precipitates increases the strength and slightly decreases the ductility [85]. Fig. 18(c) shows the X-ray diffraction patterns for the deformed sample and annealed samples in the temperature range of 200–600 °C which emphasizes the formation of *bcc* Cr-rich precipitates at 300–600 °C and sigma Cr-rich precipitates at 600 °C.

Table 8 summarizes the available data on the increase in strength due to precipitation after different procedures [33,55,85,86,101] and it demonstrates that the precipitates can be formed by conducting long-term annealing in a homogenized sample in which the value of the YS is increased only ~10% and the ductility reduced only slightly. In addition, a YS above 1 GPa can be achieved in deformed samples by post-deformation annealing. The combination of strength and ductility in the CoCrFeNiMn HEA by tailoring the microstructure through thermomechanical treatment is discussed in more detail in section 7.

5. Solid solution strengthening to make a senary alloy

Basically, the configurational entropy of an ideal solid solution increases when the number of components increases and the composition gets closer to equiatomic. The high configurational entropy stabilizes the resultant solid solution in the Cantor alloy. This concept is used to overcome the strength-ductility trade-off by simultaneously using solid solution strengthening and an appropriate ductility through the advent of multiple slip systems in the *fcc* crystal structure [125].

Solid solution strengthening is associated with the interaction of moving dislocations in a lattice of host atoms with solutes. The distortion that is made by the solute in a lattice of very dilute alloys makes a barrier to the movement of dislocations. The size mismatch and the different chemical bondings of the substitutional atoms with the host atoms contribute to the interactions of the dislocations and solutes. The extra resolved shear stress that is then needed to

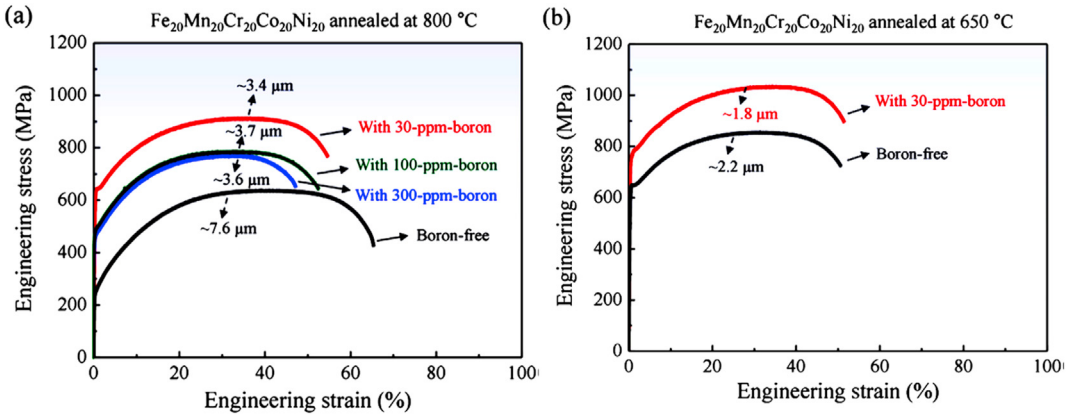

Fig. 26 – The tensile stress-strain curves of undoped and boron-doped cold-rolled Cantor alloy after annealing at (a) 800 °C and (b) 650 °C [144].

overcome such impediments leads to solid solution hardening. The extent to which an alloy can be strengthened by solid solution hardening depends on the distortion made by the solute atoms [126]. Although the incorporation of a higher number of constituent elements does not guarantee enhanced structural properties [127], the distortion that is introduced by adding a new element can contribute to additional hardening [125]. Another strengthening mechanism which is important when adding new elements to HEAs is precipitation hardening [128]. When the concentration of an alloying element becomes more than its solubility limit, it usually segregates as a precipitate and this can contribute to strengthening. However, the effects of these precipitates on ductility compromise their strengthening effects which then depend on their size and volume fraction.

The effect of adding various 6th alloying elements on the tensile properties of the CoCrFeNiMn HEA are compared in Fig. 19. It is apparent that, at least to date, the most effective substitutional alloying element for increasing the UTS is Ti after HPT as in Fig. 19(a). Adding 2 at.% of Ti was effective in enhancing the UTS in the Cantor alloy after HPT from 1740 MPa [32] to 2220 MPa [129] with the same processing conditions. Even after HPT of the $CoCrFeNiMnTi_{0.1}$ alloy accompanied by annealing at 750 °C for 1 h, a UTS value of 1220 MPa with a total elongation of 25% was achieved where these values were superior to those in the alloy after HPT and annealing at 600 °C for 1 h where there was a UTS of 1030 MPa and an elongation of 21%.

If senary alloys are compared in the as-cast condition as in Fig. 19(b), the benefits of adding 2 at. % of N becomes obvious in increasing the UTS to 765 MPa at a high elongation of ~67% [130]. Although the duplex *fcc* plus *bcc* structure that is produced by adding Al has the best strength in the as-cast condition, it comes with low elongation values [131]. Without doubt, therefore, it is reasonable to conclude that interstitials are the best alloying elements to overcome the strength-ductility trade-off. The decoration of grain boundaries that is achieved by 30 ppm of B leads to a high elongation of 55% and a UTS of 1000 MPa after cold rolling followed by annealing [132]. Other interstitials such as C and N were also successful in maintaining elongation values of 64% and 70% with UTS of 720 MPa [133] and 730 MPa [134], respectively.

Some of the important studies on the effect of adding new alloying elements on the number, volume fraction and crystal structure of stable phases, and the resultant mechanical properties in the CoCrFeNiMn HEA, are considered in detail in this section. The 6th alloying element is classified in substitutional and interstitial forms that are reviewed in two separate sections.

5.1. *Substitutional alloying elements*

5.1.1. *Aluminum*

Due to the low density and its affordable price, Al is a good candidate material and among the first studied as a 6th alloying element in the CoCrFeNiMn HEA [131]. Moreover, its larger atomic radius (d ≈ 143 pm) than any other alloying elements in the Cantor alloy (125 < d < 137 pm) can induce solid solution strengthening [163]. Even though Al has an *fcc* structure, its effects on the microstructure of HEAs are contrasting. Thus, it was found that the crystalline structure of $(FeCoNiCrMn)_{100-x}$ Al_x in the as-cast condition changed from an initial single *fcc* structure to a duplex *fcc* plus *bcc* structure and then a single *bcc* structure as the Al concentration was increased, as illustrated in Fig. 20 [131].

In single *fcc* structure alloys achieved by adding less than 8 at. % of Al a solid solution hardening was the most active strengthening mechanism [131]. Adding Al was accompanied by an increase in the lattice parameter of the *fcc* phase [163]. However, as a solid solution strengthener, the addition of Al is not so effective in increasing the strength. For example, it is possible to compare the curve for Al_0 with Al_4 and Al_7 in Fig. 21(a).

Even though introducing the second phase in higher amounts of Al, as in 8% ≤ Al < 16%, produced an increase in both the fracture and YS, it is readily apparent that the ductility was reduced significantly [131]. The duplex structure in the alloys of this region, such as Al_{11} with 25.4% of *bcc* in Fig. 20, gave a UTS as high as 1174 MPa with a total elongation of 7.7%. Poor ductility was achieved when adding more Al up to >11% [131].

In alloys that have a single *fcc* phase structure in the as-cast condition, such as the $CoCrFeNiMnAl_{0.32}$ alloy with 6 at. % of Al, subsequent cold-rolling and annealing led to the introduction of second phases such as *B2* or sigma [136]. The presence of these phases was effective in delaying recrystallization and thereby enhancing the mechanical strength by grain refinement and precipitation hardening. Furthermore, even though the heterogeneous microstructure led to a YS of 1050 MPa, a UTS of 1215 MPa and a low total elongation value of 7%, it was shown that the uniformly distributed condition of these precipitates resulted in a YS of 620 MPa, a UTS of 870 MPa and a uniform elongation of 20% [136]. In the cold-rolled $(CoCrFeNiMn)_{95.2}Al_{3.2}Ti_{1.6}$ alloy, there is a less brittle type of *B2* precipitates by comparison with the $CoCrFeNiMnAl_{0.32}$ alloy [137]. The elongation was then doubled to ~14% at similar high strength levels, with a YS of 927 MPa and UTS of 1063 MPa and a heterogeneous microstructure compared with the $CoCrFeNiMnAl_{0.32}$ alloy.

Although the *B2* phase may be present in the as-cast microstructure of the $CoCrFeNiMnAl_{0.5}$ alloy, a sufficient homogenization heat treatment can remove this phase and improve the workability of the material during plastic deformation [164]. The good combination of strength and ductility in this alloy after annealing at 1000 °C for 15 min was related to grain refinement in the matrix and ~10% volume fraction of a hard *B2* phase as shown in Fig. 21(b) [135]. The other claim in this study was the effect of adding Al in lowering the SFE due to studying the volume fraction of mechanical twins in the *B2*-free microstructure [135]. However, by using first-principle methods it was shown that the probability to induce mechanical twins decreases with increasing Al content or at high temperatures in the Al-doped Cantor alloy [165].

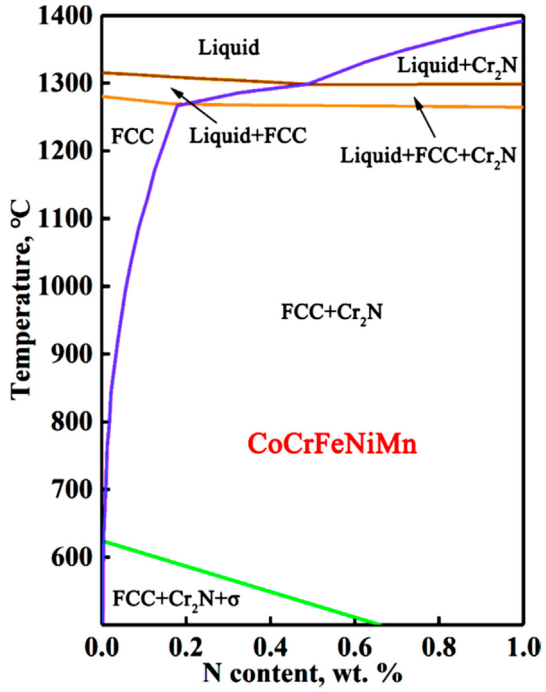

Fig. 27 – Calculated phase-diagram of CoCrFeNiMn–N [172].

It was also reported that the *B2* precipitates made the microstructure of the $CrMnFeCoNiAl_{0.75}$ alloy similar to superalloys and led to a high compression YS of 1194 MPa at room temperature and 1070 MPa at 500 °C as shown in Fig. 22 [166]. Despite the low amount of ductility at room temperature, which was less than 3%, this alloy exhibited adequate formability at temperatures as high as 500 °C at strains >20% [166].

5.1.2. *Titanium*

The atomic radius of Ti (~147 pm) is larger than Al (~143 pm) and this produces more crystal distortion and stability in the CoCrFeNiMn HEA. In a first attempt to clarify the effect of Ti, it was reported that adding ~2 at.% Ti can improve the hardness and thermal stability in the CoCrFeNiMn HEA [132] and it is important to note that no Ti-rich precipitates were detected even after processing by HPT [129]. The finer grain size achieved after HPT and similar heat treatment conditions enhanced the elongation in superplastic tensile testing from 570% in CoCrFeNiMn to 650% in $CoCrFeNiMnTi_{0.1}$ [167]. The maximum solubility of Ti in the alloy to maintain an *fcc* single phase after a homogenization heat treatment was 5.5 at. % as in $CoCrFeNiMnTi_{0.3}$ and this increased the YS and UTS from 300 to 530 MPa in the quinary alloy to 340 and 565 MPa in the $CoCrFeNiMnTi_{0.3}$ alloy, respectively [138]. Although the appearance of the Cr-rich σ phase could enhance the YS to 485 MPa, it significantly decreased the uniform elongation from 43% in $CoCrFeNiMnTi_{0.3}$ to only ~3% in $CoCrFeNiMnTi_{0.4}$ as shown in Fig. 23(a) [138].

The thermal stability and volume fraction of precipitates such as Cr-rich *bcc* and Cr-rich σ phases can be promoted in the Ti-containing Cantor alloy together with the formation of the η-Ni_3Ti phase [168]. The higher UTS value of 920 MPa and reasonable elongation of 30% in the $CoCrFeNiMnTi_{0.1}$ alloy compared with the quinary alloy [85] where the UTS was 815 MPa and the elongation was 43% at a similar YS of ~590 MPa, was attributed to the effects of these precipitates on strain hardening [139]. However, despite higher thermal stability in $CoCrFeNiMnTi_{0.3}$, it exhibited an inferior tensile behavior with UTS = 590 MPa and a ductility of 3% under similar processing conditions by comparison to the other two alloys [139].

5.1.3. *Silicon*

As an important alloying element in the steel industry, Si is another candidate that was studied as a potential 6th constituent in the CoCrFeNiMn alloying system. The atomic radius of Si at ~111 pm is smaller than for the main alloying elements of the Cantor alloy where $125<d<137$pm. Therefore, and in contrast to Al and Ti, the addition of Si decreases the lattice constant of the alloy [140]. A small amount of Si of ~4% not only increases the UTS, similar to Ti, but also it enhances the elongation as shown in Fig. 23(b) [140]. However, for large amounts of Si addition, as at >7%, brittle phases such as the σ and Laves phases appear in the as-cast microstructure and this significantly reduces the elongation. Although the YS was not affected by Si, the higher UTS and elongation values show their impact on the SFE and strain hardening mechanisms. It was also reported in other HEAs with similar chemical compositions that the addition of Si is effective in generating more strain-induced ε-martensite and crack branching in bending

fatigue tests [169]. However, in practice more research is needed to more fully clarify the precise active mechanisms associated with an Si addition.

5.1.4. *Tin*

Sn has a large atomic radius of ~140.5 pm and this leads to solid solution hardening in the CoCrFeNiMn HEA. Even though adding Sn produces a higher strength, its low solubility in the *fcc* phase leads to the formation of an $MnNi_2Sn$-like phase even in the $CoCrFeNiMnSn_{0.03}$ alloy as shown in Fig. 24(a). This amount of Sn could increase the tensile YS and UTS to 200–250 MPa and 400–450 MPa, respectively, at the expense of decreasing the total elongation from 80% to 65% as in Fig. 24(b) [143]. Although the higher amount of Sn in $CoCrFeNiMnSn_{0.1}$ increases the UTS to 500 MPa, the total elongation decreases significantly to 20%. Thus, it is hard to achieve a balance between a high strength and good elongation by adding this alloying element to the Cantor alloy in the as-cast condition.

5.1.5. *Neodymium*

The positive mixing enthalpy of Nd with the main alloying elements of the Cantor alloy, produce a liquid phase separation. However, a single *fcc* phase was reported after solidification of $(CoCrFeNiMn)_{100-x}Nd_x$ alloys with $x \leq 0.1$ [142]. Higher amounts of Nd develop an Nd-rich phase with an *hcp* structure that precipitates randomly at grain boundaries and in the interior of grains. Although these precipitates have a hardness of three times more than that of the matrix which could increase the UTS from ~520 MPa to ~800 MPa, Nd shows no significant solid solution strengthening effect [142].

5.1.6. *Molybdenum, vanadium and niobium*

Nb, Mo and V can enhance the YS of the Cantor alloy in the as-cast condition as in Fig. 25 [96,134,141,170]. Although solid solution hardening is active, the presence of the second phase was suggested as the main reason for enhancing the strength. Second brittle phases such as σ and Laves will also form if the amount of these alloying elements exceeds 4% for Mo, 4.5% for V and less than 4% for Nb as demonstrated in Fig. 25 [96,134,170].

5.2. *Interstitial alloying elements*

The distortion that arises from the great differences in the atom sizes and binding energies suggests that the addition of interstitial alloying elements will be a promising way to improve the strength of HEAs via solid solution hardening. As expected, precipitation strengthening is another mechanism that is activated by interstitials [149]. The addition of interstitial elements in austenitic stainless steels contributed to a higher strength compared to that of substitutional elements added in a similar amount [171]. The small size interstitial atoms easily enter the tetrahedral or octahedral interstitial sites of the alloys, further aggravating the lattice-distortion effect and thereby increasing the lattice constants. In addition, adding these elements reduces the kinetics of diffusional transformations which provide the opportunity to control the microstructural parameters [172]. Accordingly, the effect of adding interstitials such as B, C, N, and H on the microstructure and mechanical properties of the CoCrFeNiMn HEA are examined in this section.

5.2.1. *Boron*

Adding a very small amount of B with atomic radius of ~85 pm is known as a very appropriate method for the grain boundary engineering of polycrystalline materials in order to improve their mechanical properties and thermal stability [173]. Earlier studies reported that boron segregation leads to a change in the grain boundary structure, energy, composition and the mechanical properties in some materials [174]. However, segregation of B as a brittle compound has a weakening effect on the grain boundaries and this has restricted its usage. The addition of only 30 ppm of B significantly enhanced the YS from 250 to 630 MPa and the UTS from 600 to 900 MPa with a

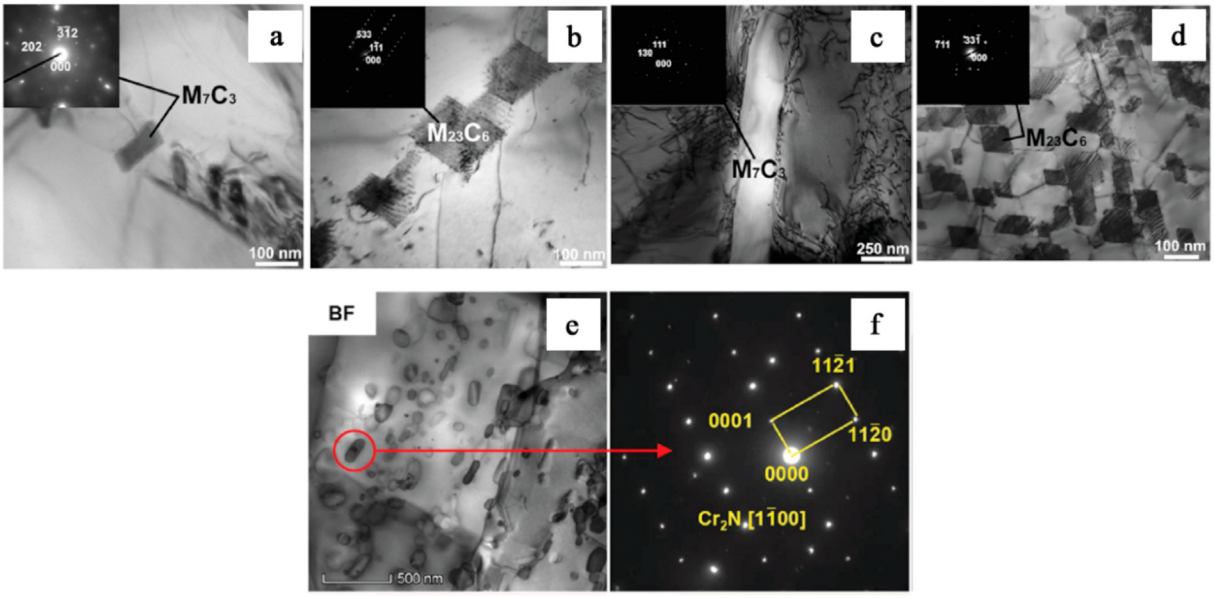

Fig. 28 – The TEM images from carbides in $CoCrFeNiMnC_{0.1}$ (a–b) [178], $CoCrFeNiMnC_{0.25}$ (c–d) [178] and nitrides in CoCrFeNiMn doped with 1 at. % of N (e–f) [145].

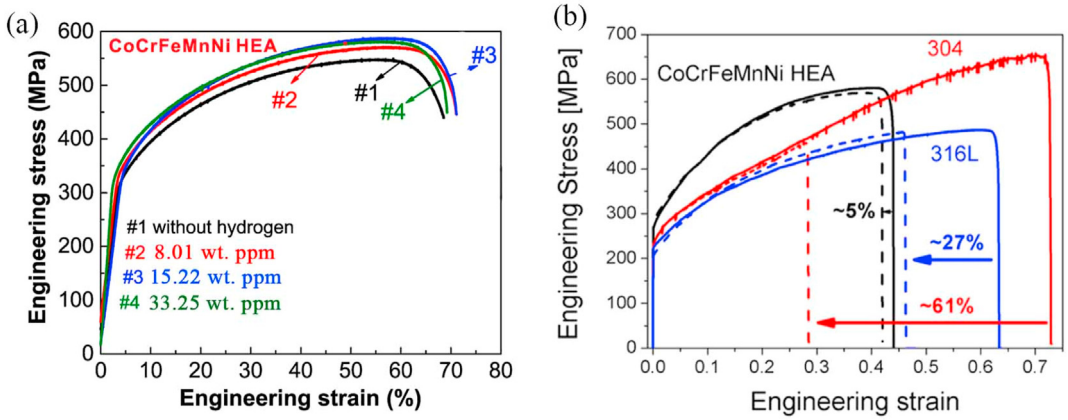

Fig. 29 – Stress-strain curves of the Cantor alloy (a) at different concentrations of H [159] and (b) in comparison with other stainless steels [157].

decrease in the total elongation for 10% after cold rolling followed by annealing at 800 °C as in Fig. 26 [144]. Boron decorates the grain boundaries and acts both through interface strengthening and through a grain size reduction. Even in conditions where the grain growth is sluggish, as in annealing at 650 °C, 30 ppm of B increased the YS for ~120 MPa without any reduction in ductility. These effects enhance the grain boundary cohesion and retard any capillary-driven grain coarsening, thereby demonstrating that boron-induced grain boundary engineering is an ideal strategy for the development of advanced HEAs [144].

5.2.2. *Carbon and nitrogen*

The two most studied interstitial alloying elements in traditional alloys are C and N with atomic radii of ~70 pm and ~65 pm, respectively [175,176]. Solid solution strengthening, precipitation hardening, grain boundary strengthening and the TWIP (twinning-induced plasticity) effect are the mechanisms that are affected by the addition of N and C [172].

Nitrogen was reported to contribute to higher local distortion in the *fcc* matrix than carbon which leads to higher strain fields and atomic misfit [177]. In addition, the binding energy of the dislocation-interstitial atom is higher for N than for C and this gives a greater inhibition in dislocation movement [177].

The elastic properties, atomic interactions and phase-volume fractions that have a direct effect on mechanical properties are changed by adding interstitial alloying elements. The precipitation of carbides and nitrides increases the hardness of the CoCrFeNiMn HEA [178–182]. It is well established that C/N atoms tend to segregate and combine with strong carbide/nitride forming elements to form precipitates when the C/N content exceeds the solid solubility of HEAs. According to the solubility, the precipitate forming alloying elements can be ranked as Cr > Mo > W > Mn > Fe [172].

Deformation and strengthening mechanisms were also affected by adding these interstitial elements. Solid solution strengthening is effective in increasing the YS of HEAs by

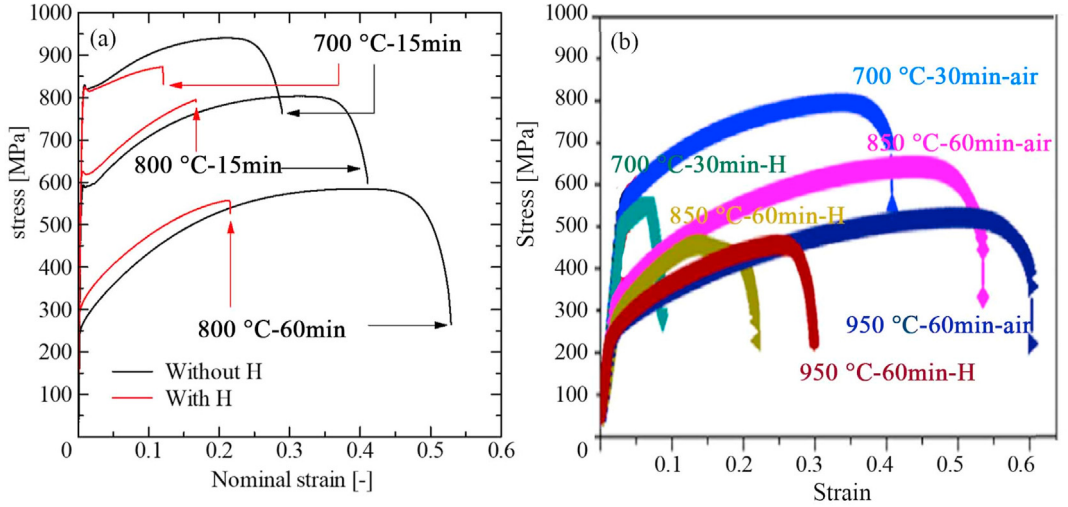

Fig. 30 – Engineering stress-strain curves of the Cantor alloy after cold-rolling and annealing heat treatment (a) pre-charged with 100 MPa hydrogen gas atmosphere at 270 °C for 200 h [158] and (b) *in situ* H-charging [210].

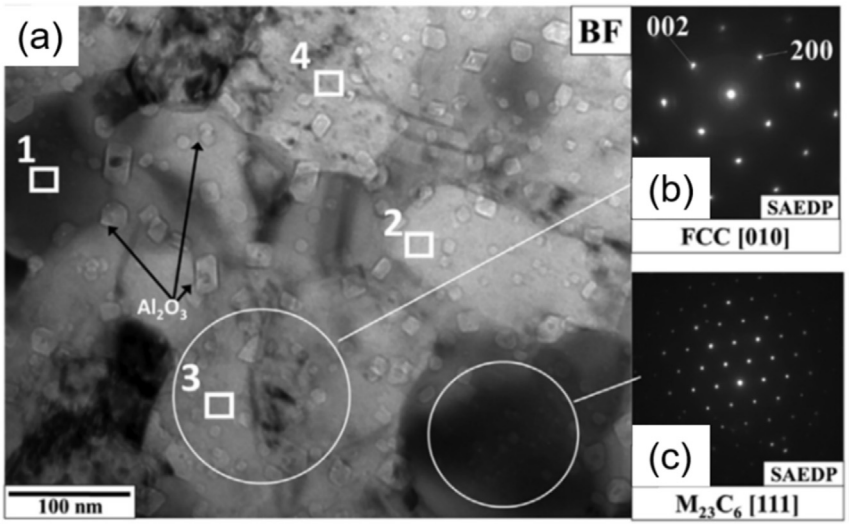

Fig. 31 – (a) Bright-field TEM image of the CoCrFeNiMn HEA with 5% Al_2O_3 and (b, c) SAED patterns of *fcc* and carbide [214].

Table 9 – Summary of the mechanical properties of CoCrFeNiMn HEA matrix composites.

	Particle	%	Processing	Hardness	E (GPa)	YS at RT (MPa)	Ref.
CoCrFeNiMn	–	–	MA + HIP	418 HV	185	1180[a]	[214]
	Al_2O_3	5 wt	MA + HIP	545 HV	210	1600[a]	
	–	–	MA + SPS	1.96 GPa	–	–	[215]
	Y_2O_3	3 wt	MA + SPS	5.36 GPa	–	–	
	–	–	MA + SPS + AN at 900°C-5h	1.83 GPa	–	–	
	Y_2O_3	3 wt	MA + SPS + AN at 900°C-5h	5.16 GPa	–	–	
	–	–	MA + SPS + AN at 900°C-10 h	1.86 GPa	–	–	
	Y_2O_3	3 wt	MA + SPS + AN at 900°C-10 h	5.33 GPa	–	–	
	–	–	MA + SPS	3.63 GPa	204	971[b]	[14]
	Y_2O_3	0.3 wt	MA + SPS	4.24 GPa	204	1005[b]	
	TiO(C)	–	MA + SPS + HE		–	1298[b]	[216]
$Al_{0.3}$CoCrFeNiMn	–	–	MA + SPS	–	–	970[a]	[217]
	Y_2O_3	0.5 vol	MA + SPS	–	–	1150[a]	
	Y_2O_3	1 vol	MA + SPS	–	–	1600[a]	
	Y_2O_3	1.5 vol	MA + SPS	–	–	1650[a]	
	Y_2O_3	2 vol	MA + SPS	–	–	1660[a]	
	Y_2O_3	3 vol	MA + SPS	–	–	1760[a]	
CoCrFeNiMn	$M_{23}C_6$+ $(Cr,Mn)_3O_4$	–	MA + HE at 1000 °C	–	–	820[b]	[218]
	$M_{23}C_6$+ $(Cr,Mn)_3O_4$	–	MA + HE at 1150 °C	–	–	464[b]	
	–	–	SPS	181 HV	–	271[a]	[219]
	Cr_3C_2	10 wt	SPS	323 HV	–	578[a]	
	Cr_3C_2	20 wt	SPS	417 HV	–	713[a]	
	Cr_3C_2	40 wt	SPS	682 HV	–	2045[a]	
	–	–	MA + SPS	–	–	507[a]	[220]
	TiC	5 wt	MA + SPS	–	–	698[a]	
	–	–	MA + HPT	577 HV	–	–	[221]
	–	–	MA + HPT at 700 °C-1h	380 HV	–	–	
	–	–	MA + HPT at 700 °C-1h	300 HV	–	–	
	–	–	MA + HPT at 700 °C-1h	240 HV	–	–	
	TiC	5 wt	MA + HPT	626 HV	–	–	
	TiC	5 wt	MA + HPT at 700 °C-1h	450 HV	–	–	
	TiC	5 wt	MA + HPT at 700 °C-1h	390 HV	–	–	
	TiC	5 wt	MA + HPT at 700 °C-1h	300 HV	–	–	
	–	–	MA + HIP	484 HV	184	1180[a]	[222]
	SiC	5 wt	MA at 100 rpm + HIP	485 HV	229	1480[a]	
	SiC	5 wt	MA at 200 rpm + HIP	699 HV	214	1900[a]	

[a] and.
[b] are representative results of compression and tensile tests, respectively.

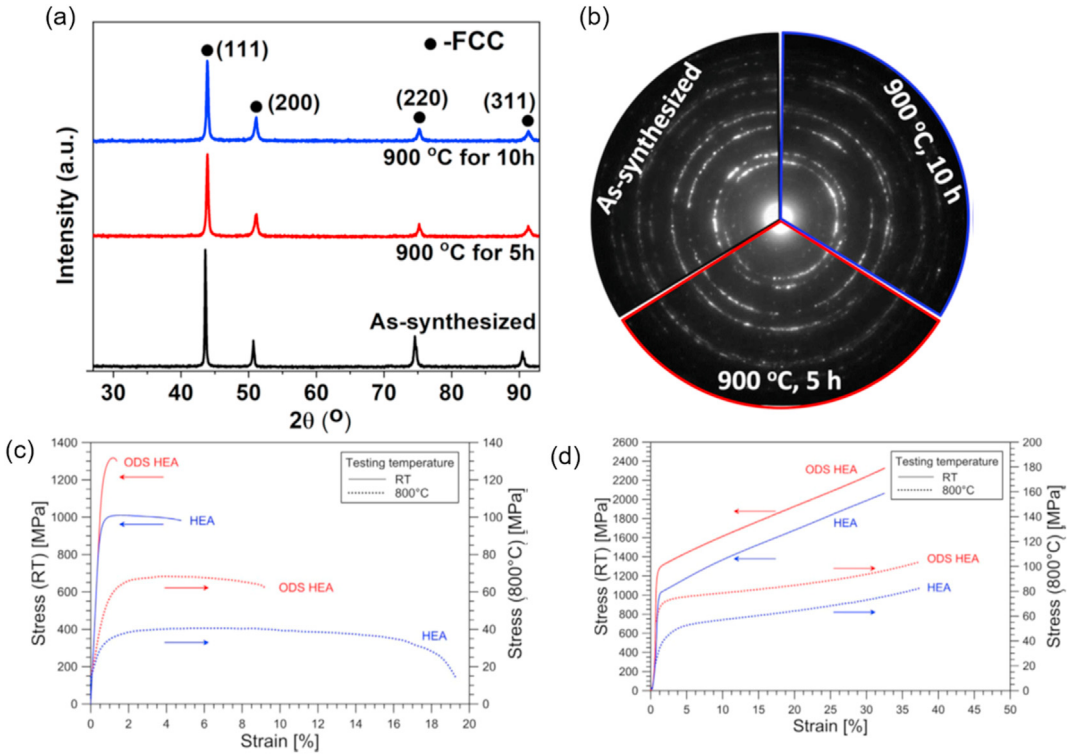

Fig. 32 – (a, b) X-ray diffraction patterns and SAED patterns of the as-synthesized ODS CoCrFeNiMn HEA sample and after annealing at 900 °C for 5 and 10 h [215], (c, d) Tensile stress-strain and compression stress-strain curves of HEA and ODS HEA tested at room temperature (RT) and at 800 °C, respectively [14].

adding C/N [172,183,184]. However, the main strengthening effect of adding C/N is due to the precipitation hardening of carbides and nitrides [161]. Most of the reports show that these particles are incoherent with the matrix in the alloy and mobile dislocations bypass the particles through conventional Orowan looping [161]. The grain refinement that was noted earlier as one of the advantages in doping with C/N extends the dislocation accumulation at the grain boundaries and significantly improves the strength of the material [152].

As noted in earlier sections, the formation of deformation twinning and twin boundaries can be beneficial for improving the plasticity and strength simultaneously in HEAs [148,172]. Although adding N to the alloy led to a higher SFE [145,185], the effect of C on the SFE and mechanical twin formation are in debate and the claimed mechanisms are not fully convincing [172]. It was reported in some investigations that adding C atoms increases the SFE of the HEA [150,151,181,186] but there are other claims that the solid solution hardening induced by interstitials increases the activation energy for dislocation slip and facilitates the activation of twinning [153,154,187]. Although for conditions that carbon remains in a solid solution state (~0.99 at.%) the occurrence of mechanical twinning was promoted in the alloy [148,154], in N-doped alloy a deformation-induced twinning was not observed even after

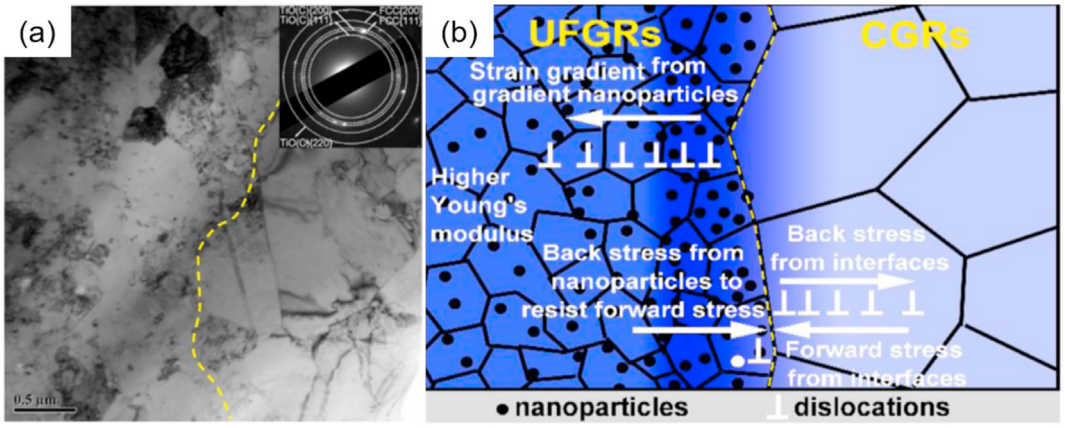

Fig. 33 – (a) TEM bright-field image for CoCrFeNiMn HEA containing TiO(C) particles produced by MA followed by SPS and a further HE process and (b) schematic illustration of the three mechanisms enhancing the back stress [216].

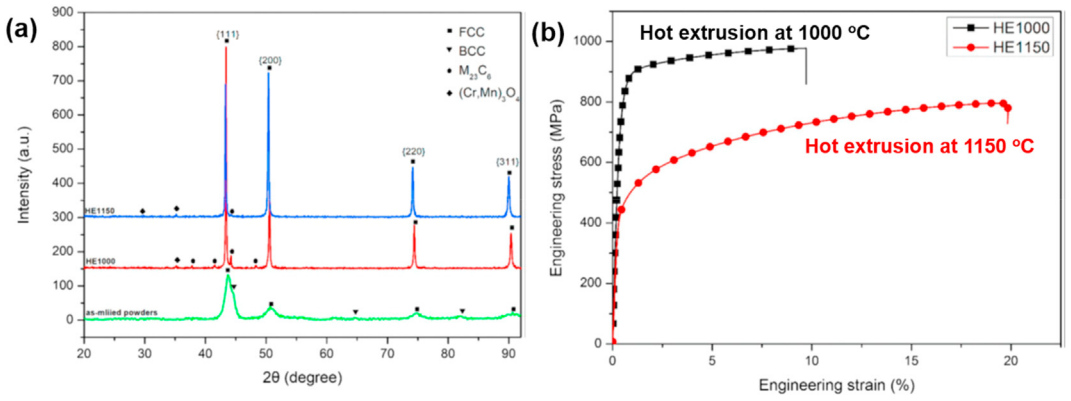

Fig. 34 – (a) X-ray diffraction patterns before and after the consolidation of CoCrFeNiMn matrix containing carbide and oxide particles and (b) tensile engineering stress-strain plots [218].

tensile testing at a low temperature of −196 °C [130]. However, mechanical twinning is hampered when any extra carbon precipitates as carbides [150]. Similarly, N changed the microstructure of the rolled alloy by leading to the formation of micro-bands instead of mechanical twinning [145].

These elements have a strong effect on the planarity of slip [188,189]. When the concentration of interstitials is more than their solubility limits and segregates as precipitates, they become strong obstacles to the slip of dislocations and thereby they promote the occurrence of cross-slip. Therefore, wavy slip is favored in this condition, and the interactions of large numbers of dislocations contribute to the formation of dislocation cells, dislocation clusters and dislocation dense walls. When the local stress near these precipitates exceeds a critical stress, the nucleation of micro-cracks and their propagation produces a plastic instability. However, planar slip governs the plastic deformation when these precipitates are absent [189]. Planar slip also occurs more easily in homogenous compositions or low SFE HEAs. When the strain is low, dislocations move in a planar mode and stacking faults form due to the low SFE. Increasing the strain values duplicates the stacking faults and produces a Taylor lattice structure. A mixed structure of non-cell forming structures, as with a Taylor lattice, micro-bands and domain boundaries, and rare

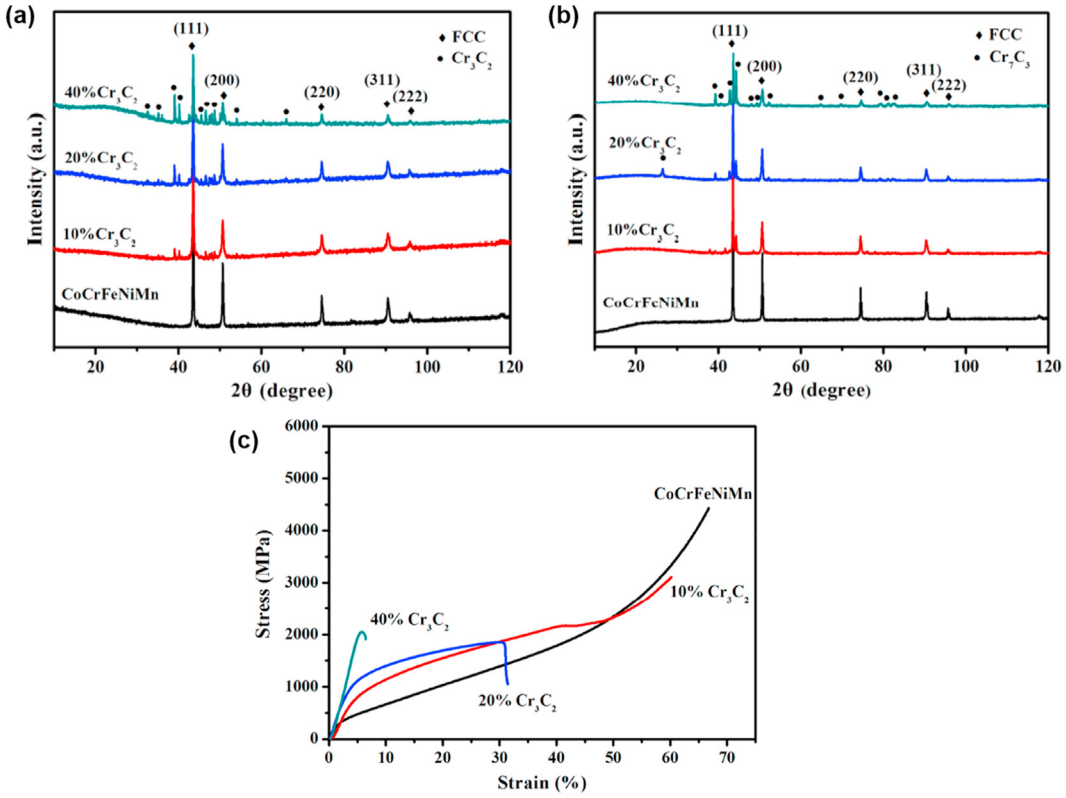

Fig. 35 – (a) X-ray diffraction patterns (a) before and (b) after SPS and (c) compressive stress-strain plots of CoCrFeNiMn matrix composite reinforced by Cr_3Cr_2 carbide at room temperature [219].

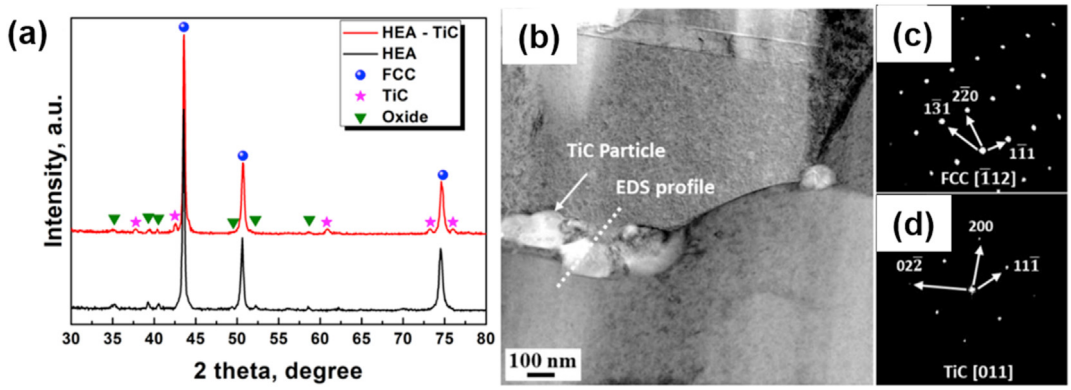

Fig. 36 – (a) X-ray diffraction patterns after SPS and (b, c, d) Bright-field TEM image and corresponding SAED patterns of the CoCrFeNiMn matrix and TiC [220].

twins appear at higher strains. At high strain values, the non-cell forming structures are destroyed and mechanical twins appear on these stress concentration sites [172].

The calculated phase diagram of CoCrFeNiMn–N alloys by Thermo-Calc software is presented in Fig. 27. According to the prediction, the highest solubility of N is only ~0.18 wt. % (0.84 at. %) near the melting point of the alloy in equilibrium conditions. This suggests decreasing the N content from 1 to 0.5 at.% leads to a disappearance of the nitride particles after cold-rolling followed by annealing [190]. The more sluggish diffusion of N by comparison with C leads to a lower volume fraction of precipitates in the as-cast condition of the N-doped material than in the carbon-containing HEAs [130,179,191].

The reported carbides are M_7C_3 with elongated irregular shapes and $M_{23}C_6$ with nearly-circular and rectangular or regular shapes as shown in Fig. 28 [153,178]. However, in N-doped alloys the extra N precipitates in the form of semi-coherent Cr-rich M_2N particles with an hexagonal structure [145,177,192,193]. The size and the volume fraction of these precipitates depend on the annealing temperature and this subsequently affects the pinning force in the Zener effect and the grain sizes [152,193]. These precipitates restrict dislocation motion and therefore inhibit the movement of grain boundaries and thus decelerate recrystallization. The other reported reason for the grain refining effect of interstitial alloying elements is their role in lowering the recovery rate that leads to a

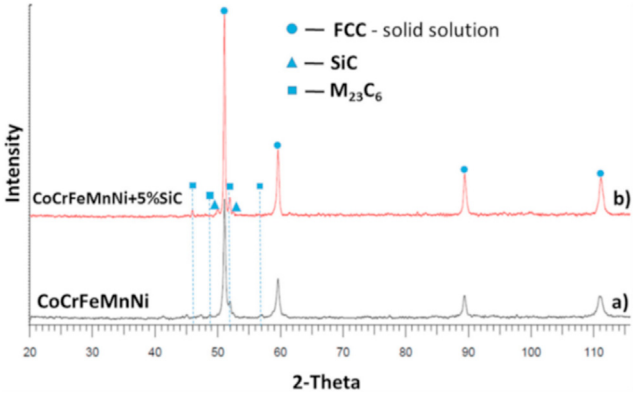

Fig. 37 – X-ray diffraction patterns of (a) CoCrFeNiMn HEA and (b) CoCrFeNiMn–SiC composite [222].

higher storage of cold-work energy [153]. As an example, the presence of Cr_2N decreases the grain size of an alloy containing ~1 at.% N from 7.6 μm to 2.5 μm after friction-stir processing [146]. Moreover, due to the low mixing enthalpy of Cr–N and Cr–C binding, the presence of nitrides and carbides prevents sigma phase precipitation that is generally formed at low annealing temperatures [161,177]. It should be noted that these nitride and carbide particles will dissolve after exposure to temperatures more than 1000 °C [193] and 1125 °C [194], respectively.

The other effect of N and C is that it becomes easier to make a heterogeneous microstructure so that, as discussed in section 5.2, it combines soft and hard domains and is beneficial for enhancing the strength-ductility trade-off [150,151,195]. This heterogeneous microstructure increases the interaction of dislocations during deformation and this leads to back-stress hardening. The increase in C-content changes the fully recrystallized microstructure to a bimodal microstructure [151]. A unique complex heterogeneous microstructure consisting of fine recrystallized grains, large non-recrystallized grains and nanoscale Cr_2N precipitates was obtained in a nitrogen-doped (0.3 wt. %) CoCrFeNiMn HEA [196]. Although the YS and UTS doubled by this process by comparison to those of the quinary alloy, it is apparent that an optimization of the processing conditions to reach a reasonable combination of strength and ductility needs further investigations.

According to the numerous reports on the effect of adding interstitial elements such as C and N on the tensile properties of the HEA [130,145,146,148–155,161,181–184,190,196–198], they can be assumed as good candidates for increasing the low strength level. Despite the beneficial effect of adding C or N on the strength level of the alloy, they have a different effect on elongation [130,154,190]. It was well established that their elongation value is preserved as far as the concentration of interstitials that are in their solubility limit but nevertheless the ductility degrades after the segregation and forming of precipitates. It was reported that adding C has a more severe effect on the deterioration of ductility by comparison with N. The elongation significantly decreased at room temperature from 65% to 38% by doping with only 0.5 at.% of C [154] but it changed slightly from 65% to 60% by increasing N from 0.5 to

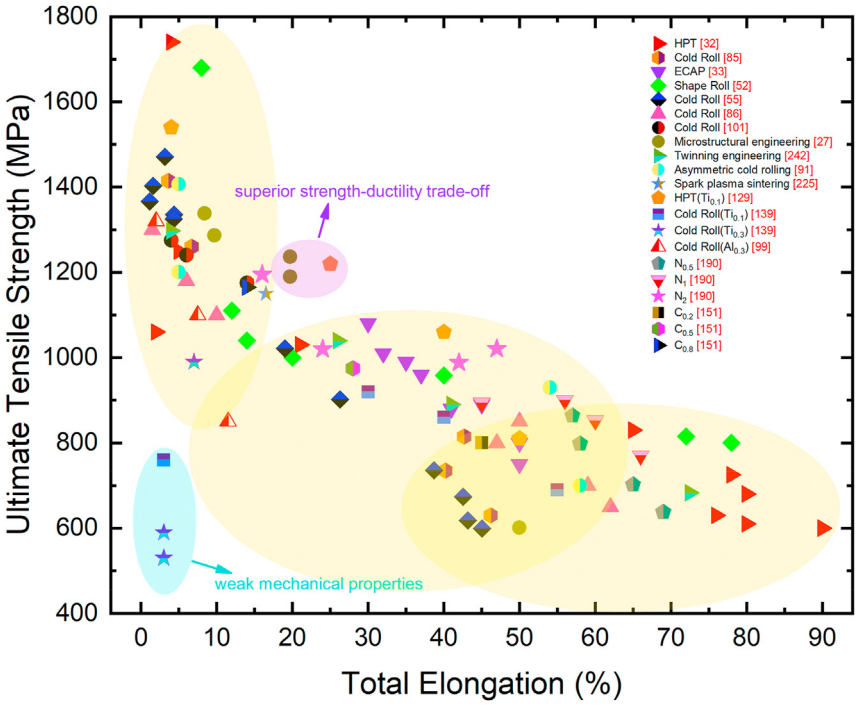

Fig. 38 – Ultimate tensile strength versus total elongation of the CoCrFeNiMn HEA for different processing.

~1% [190]. The addition of more of these elements (~3 at.%) significantly decreases the ductility [149].

5.2.3. *Hydrogen*

H with an atomic radius of ~53 pm is the smallest, lightest and most unwanted alloying element that can cause catastrophic failures in engineering metallic alloys [199]. The embrittlement that is induced by H has been under extensive investigation for more than a century [200]. In practice, hydrogen atoms are usually trapped at vacancies, dislocations and other lattice defects and they can cause damage by mechanisms such as hydrogen-enhanced localized plasticity [201],

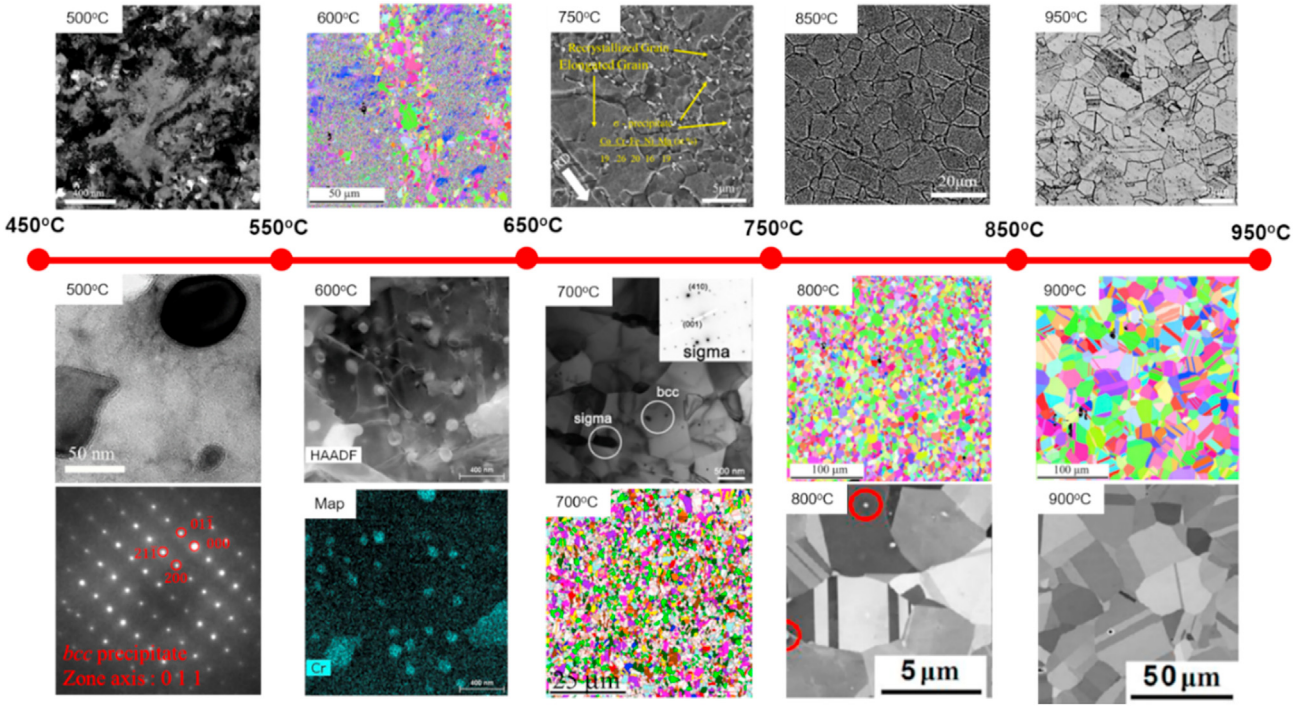

Fig. 39 – Microstructural evolution of deformed CoCrFeNiMn HEA during annealing at elevated temperatures [34,52,85–87,104,230].

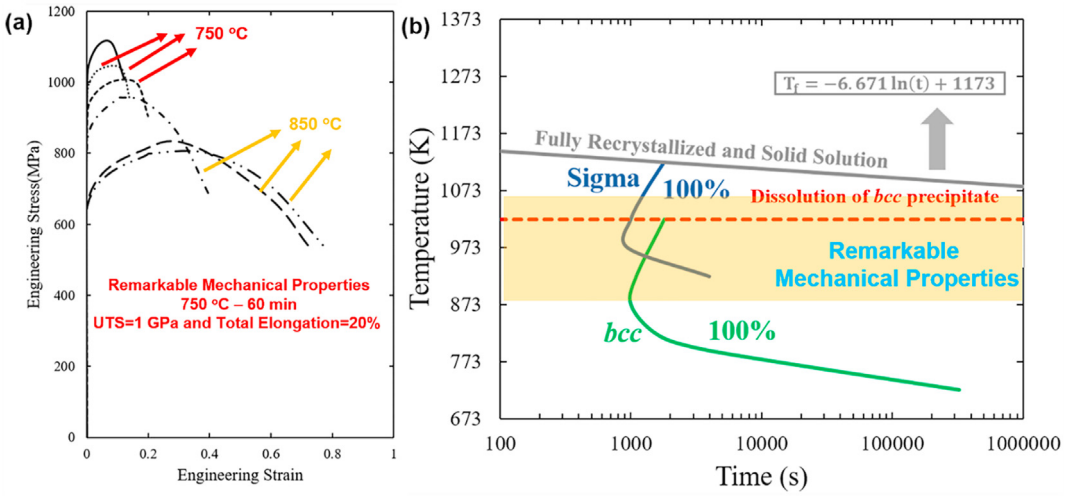

Fig. 40 – (a) Engineering stress versus engineering strain for different PDA conditions (at 750 and 850 °C from 10 to 60 min) and (b) Temperature-Time-Transformation (TTT) plot for deformed CoCrFeNiMn HEA [52].

hydrogen-enhanced decohesion [199] and hydride formation [202].

The effect of adding hydrogen to the Cantor alloy was also studied in recent years. Despite engineering alloys such as Inconel 718 and stainless steels that become brittle with the presence of hydrogen, a different behavior was observed when the CoCrFeNiMn HEA was pre-charged with hydrogen [157,159,160]. Thus, it was reported that the tensile strength and ductility of the alloy were enhanced simultaneously at low amounts of H (≤33.25 ppm) as shown in Fig. 29(a) [159]. Moreover, the hydrogen embrittlement resistance was maintained at 54 ppm of H even under cryogenic conditions [203,204]. It was reported that H promotes the formation of stacking faults and mechanical twinning during plastic deformation due to the decrease in the SFE [159,205] and these defects subsequently hinder the diffusion of hydrogen [206]. Even though hydrogen charging to 76 ppm decreases the elongation, it shows more ductility than stainless steels as shown in Fig. 29(b) under similar charging conditions [157,207]. Furthermore, the pre-straining that was reported as an accelerator of hydrogen embrittlement in stainless steels [208] shows no significant change in properties for the CoCrFeNiMn HEA containing 54 ppm of H [209].

As expected, grain refinement increases the diffusible hydrogen content in the CoCrFeNiMn HEA [158]. Although a high hydrogen content of ≥100 ppm degraded the tensile elongation, the grain refinement improved the strength-elongation balance in the pre-charged condition as demonstrated in Fig. 30(a). Basically, the reported results in Fig. 30 show clearly the effect of H addition on the mechanical properties of the Cantor alloy. It was suggested that the area of the brittle-fractured zone decreased and its fracture morphology changed from intergranular to transgranular with increasing annealing time or temperature and this indicates an improved hydrogen embrittlement resistance. The remaining dislocations along grain boundaries in the specimens annealed at lower temperatures were proposed as the reason for this intergranular fracture [210]. However, the slip bands and dislocations along a certain slip system are responsible for transgranular fracture in coarser grain structures.

It was suggested that the major site of diffusible hydrogen in the alloy is not grain boundaries so that hydrogen trapping at interstitial sites is the key factor. These sites were distorted by the large amount of solute atoms in the HEA [158]. The presence of a sigma phase can significantly decrease the work hardening rate and tensile strength in the H-charged ultrafine-grained Cantor alloy because hydrogen assists in producing cracking at the interfaces of the sigma and *fcc* phases [158,210]. Therefore, in order to improve the hydrogen embrittlement resistance through the grain refinement approach, an optimal annealing temperature and time must be selected.

It was reported that the diffusibility of hydrogen in the CoCrFeNi alloy is remarkably lower than in the CoCrFeNiMn alloy which confirms the role of the Mn–H interaction in the high diffusible hydrogen content of the Cantor alloy [158,211]. Decreasing the Mn content was also another attempt that was undertaken to improve the hydrogen embrittlement resistance of the CoCrFeNiMn alloying system [212]. The higher H content of the Cantor alloy by comparison with the CoCrFeNi alloy at similar charging conditions leads to an inferior hydrogen embrittlement resistance for the quinary alloy compared with the quaternary alloy [207,211]. The absence of the Mn–H interaction led to a nearly complete resistance to hydrogen embrittlement even after pre-charging by 100 MPa hydrogen gas both in the fine and coarse-grained CoCrFeNi alloy [212].

Despite the beneficial effects of adding H to the tensile behavior of the Cantor alloy, experiments showed that the fatigue crack growth was accelerated by adding H [213]. It was shown also that under *in situ* electrochemical hydrogen charging, deformation twinning at the high ΔK region and dislocation cells at the low ΔK region were enhanced in the presence of H. Thus, the active hydrogen embrittlement mechanisms changed from hydrogen-enhanced decohesion

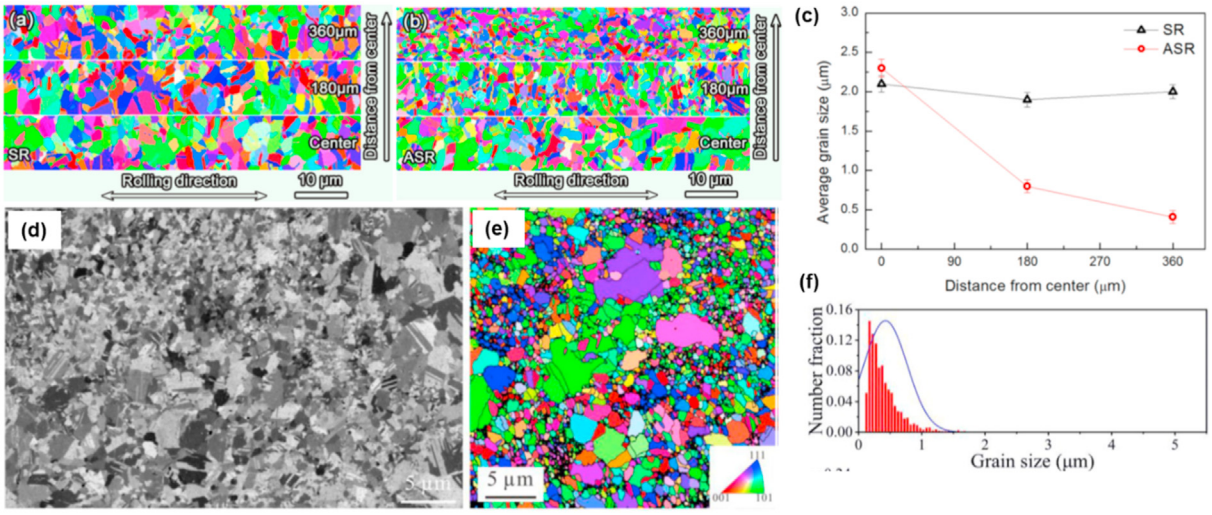

Fig. 41 – EBSD inverse pole figure images of CoCrFeNiMn HEA after (a) cold rolling and (b) asymmetric cold rolling followed by annealing [91], (c) the grain size distribution of CoCrFeNiMn HEA after cold rolling and asymmetric cold rolling followed by annealing [91], (d,e) Microstructure of CoCrFeNiMn after SPS [225] and (f) grain size distribution of CoCrFeNiMn after SPS [225].

under low stress conditions to a combination of hydrogen-enhanced localized plasticity and hydrogen-enhanced decohesion in the high stress state.

6. CoCrFeNiMn matrix composites or oxide dispersion strengthened HEAs

Metal matrix composites, reinforced with nano-particles, are promising materials that exhibit many interesting properties. The nano-particles, having typically physical and chemical properties drastically different from the matrix, have an effect on the mechanical strength, hardness, dimensional stability, ductility, wear resistance and/or fracture toughness at room and elevated temperatures. Very recently, there were many attempts to improve the mechanical properties of the CoCrFeNiMn HEA by adding particles to form an HEA matrix composite. The strengthening mechanism in these HEA matrix composites is mainly particle strengthening as in the Orowan mechanism and grain boundary strengthening as in the Hall-Petch effect. It is important to note that the presence of ceramic particles is very effective in preventing grain growth and improving the thermal stability of the HEA.

These composites are usually processed by the mechanical alloying (MA) method followed by consolidation procedures including hot isostatic pressing (HIP), spark plasma sintering

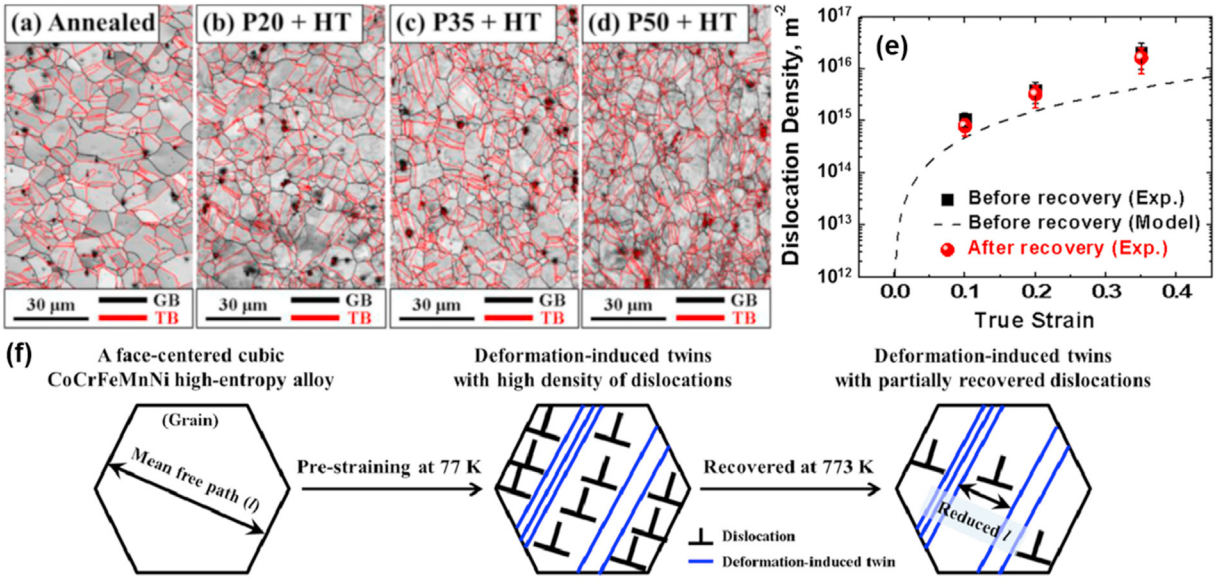

Fig. 42 – (a,b,c,d) The EBSD image quality of annealed and twinning engineered CoCrFeNiMn samples [242], (e) dislocation density versus applied strain [244] and (f) schematic of the microstructure during the twinning engineering [242].

(SPS) or hot extrusion (HE). It was well established that composites with ultrafine or nanoscale structures can be achieved by SPS because of its rapid heating and cooling rate [223]. A summary of the mechanical properties of the CoCrFeNiMn composites described in this section is given in Table 9.

6.1. *Oxides*

Experiments successfully produced HEA matrix nanocomposites with Al_2O_3 reinforcement particles using MA followed by HIP for consolidation [214] The microstructure obtained from this process was in the form of equiaxed grains with an average size of ~30–150 nm, nano-particles of Al_2O_3 having a size of ~5–35 nm and a small amount of $M_{23}C_7$ carbides as shown in Fig. 31. The presence of carbon was related to the dissolution of heptane which was used as a milling agent where this reacted afterwards with the Cr-enriched particles and formed carbides [214]. The mechanical properties showed that the presence of Al_2O_3 nanoparticles improved the YS from ~1180 to ~1600 MPa and the value of the Young's modulus reached ~210 GPa which is almost 25 GPa higher than for the particle-free HEA.

In another study, the effect on the properties of an addition of yttria-reinforcement particles of Y_2O_3 was considered for the CoCrFeNiMn HEA by producing through MA followed by SPS. It was reported that there was an ultra-grain growth resistance at 900 °C due to the high pinning effect of the yttria dispersions and the absence of a phase transformation at ≤900 °C as in Fig. 32(a, b) [215]. In another study on an oxide dispersion strengthened CoCrFeNiMn HEA using yttria particles [14], the results showed that the YS in tensile testing at room temperature increased from ~971 to ~1269 MPa and the YS in compression testing at room temperature increased from ~1005 to ~1232 MPa as in Fig. 32 (c, d) [14]. Additionally, the measured creep strain rates for the strengthened alloy were significantly lower, by three orders for a 30 MPa stress level, compared with the initial condition which confirmed the presence of very effective pinning [14]. In another study, the effect of the composite production method as *ex situ* or *in situ* was investigated [224] and this showed that the Y pre-alloying method was efficient in achieving fine coherent dispersoids with an ultrafine-grained microstructure leading to an incremental increase in the tensile strength of the CoCrFeNiMn HEA [224].

In another study, a CoCrFeNiMn HEA containing TiO(C) particles was produced using MA followed by SPS and a further HE process as in Fig. 33 [216]. The produced microstructure was inhomogeneous consisting of an area with ultrafine-grains and TiO(C) particles as well as an area containing coarse grains without TiO(C) particles [216]. This microstructure exhibited remarkable tensile mechanical properties including a YS of ~1300 MPa, UTS of ~1400 MPa and a uniform elongation of ~10% which showed better properties by comparison with other CoCrFeNiMn composites [14,216,225]. These mechanical properties demonstrate that a multilevel heterogeneous structure provides an influential strategy for overcoming the strength–ductility synergy of alloys [216]. It was indicated that this heterogeneous structure provides a strain gradient associated with the nanoparticles to thereby enhance the back stress. In addition, nanoparticles effectively increase the resistance to the forward stress, leading to a better strength–ductility synergy than may be achieved using a simple heterogeneous structure with only ultrafine-grains or a coarse-grained microstructure [216].

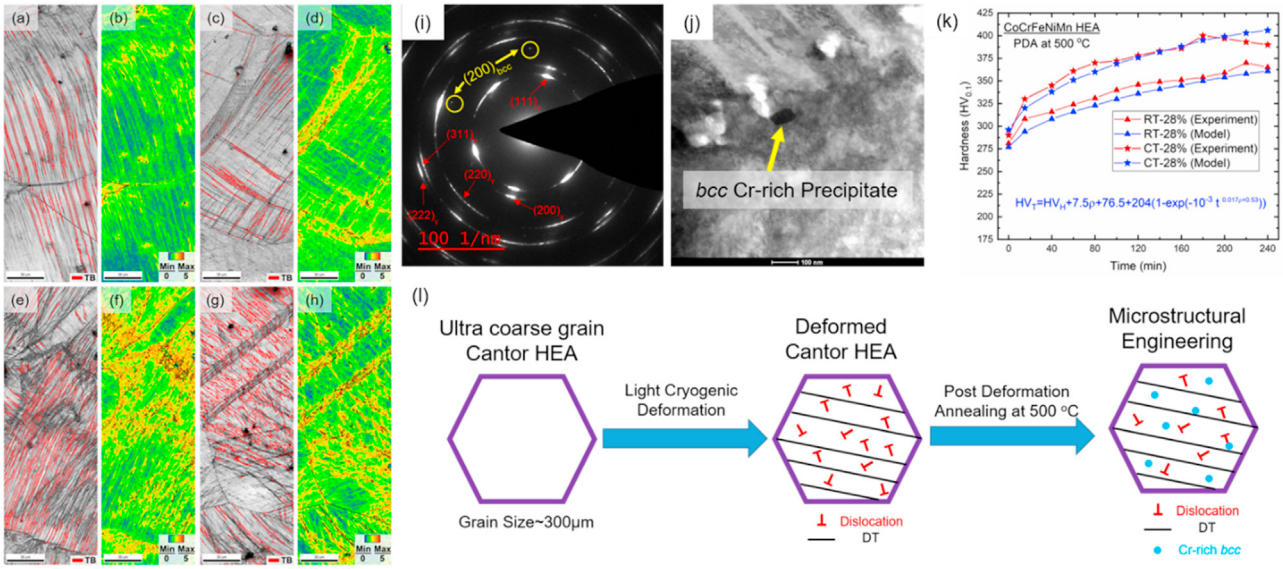

Fig. 43 – EBSD image quality, and EBSD kernel average misorientation for (a,b) room temperature rolling (28%), (c,d) room temperature rolling (28%) followed by annealing at 500 °C, (e,f) cryogenic temperature rolling (28%), and (g,h) cryogenic temperature rolling followed by annealing at 500 °C samples, (i) selected area electron diffraction of the sample after annealing at 500 °C, (j) presence of *bcc* Cr-rich in the bright-field STEM image, (k) dependence of hardness of the deformed samples on the annealing time and (l) schematic illustration of the microstructure during the microstructural engineering [27].

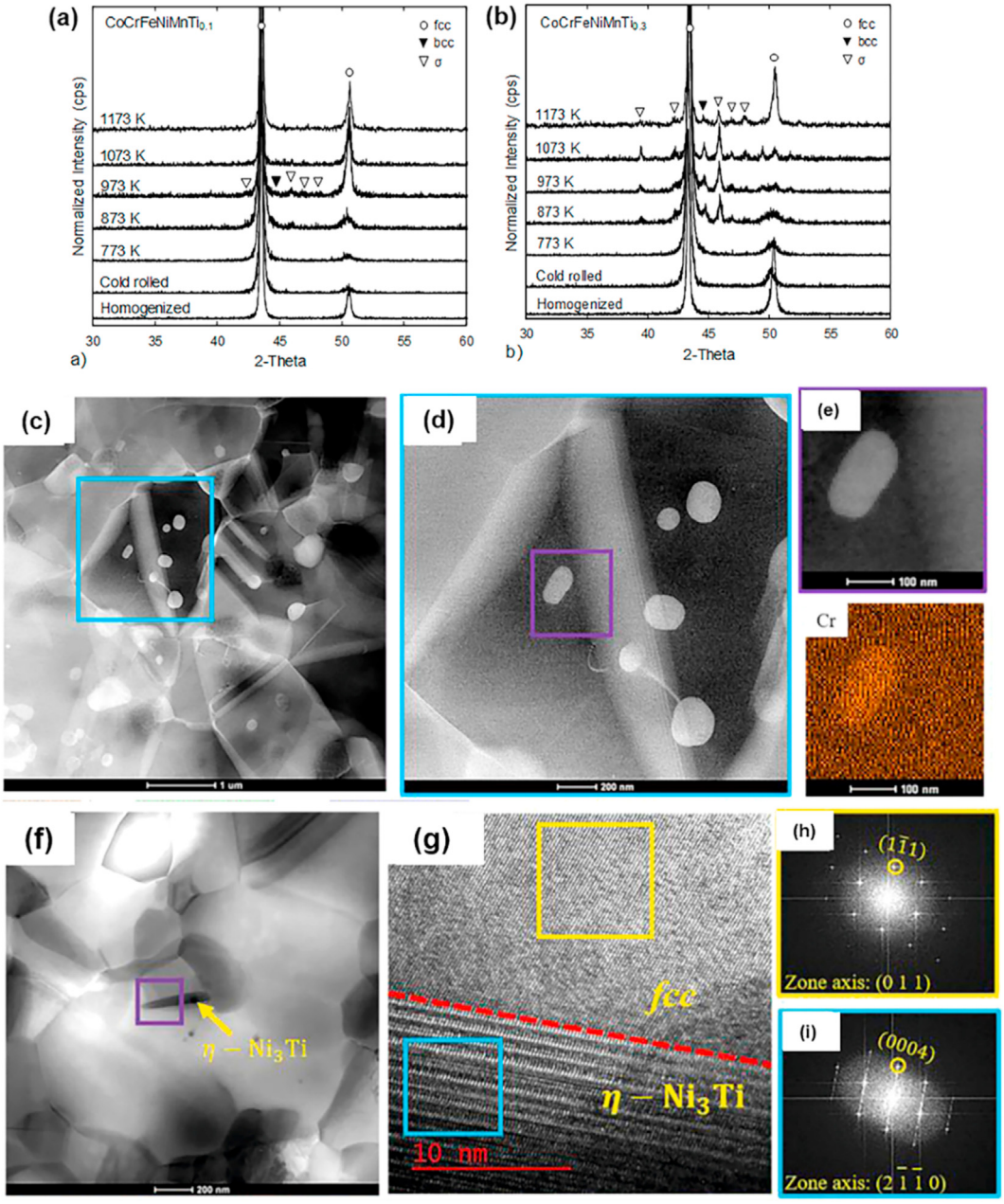

Fig. 44 – (a,b) X-ray diffraction patterns of $CoCrFeNiMnTi_x$ (x = 0.1 and 0.3) HEAs after homogenizing and cold rolling followed by annealing at different temperatures [139], (c,d) Microstructures (STEM images) of the $CoCrFeNiMnTi_{0.1}$ HEA after PDA at 800 °C [168], (e) EDS elemental map analyses [168], (f) Microstructures of the $CoCrFeNiMnTi_{0.3}$ HEA after PDA at 800 °C [168] and (g,h,i) HRTEM image, fast fourier transform (FFT) for the η-Ni_3Ti phase and the *fcc*-matrix, and EDS elemental map analyses [168].

6.2. *Carbides*

Basically, carbide particles similar to oxide particles can be produced *in situ* during the consolidation process in which the strength increases simultaneously with grain growth resistance in the matrix due to the Zener pinning effect [226]. An *in situ* CoCrFeNiMn composite was produced containing carbide and oxide particles using MA followed by HE for the consolidation operation [218] These experiments showed that the microstructure included an ultrafine-grained matrix of <1 μm, randomly distributed $M_{23}C_6$ particles which were Cr-rich and spinel $(Cr, Mn)_3O_4$ oxide particles after the consolidation process as shown in Fig. 34(a). It was demonstrated that the oxide particles coarsened, the $M_{23}C_6$ particles dissolved and plate-like carbides were precipitated at the grain boundaries after increasing the temperature of extrusion from 1000

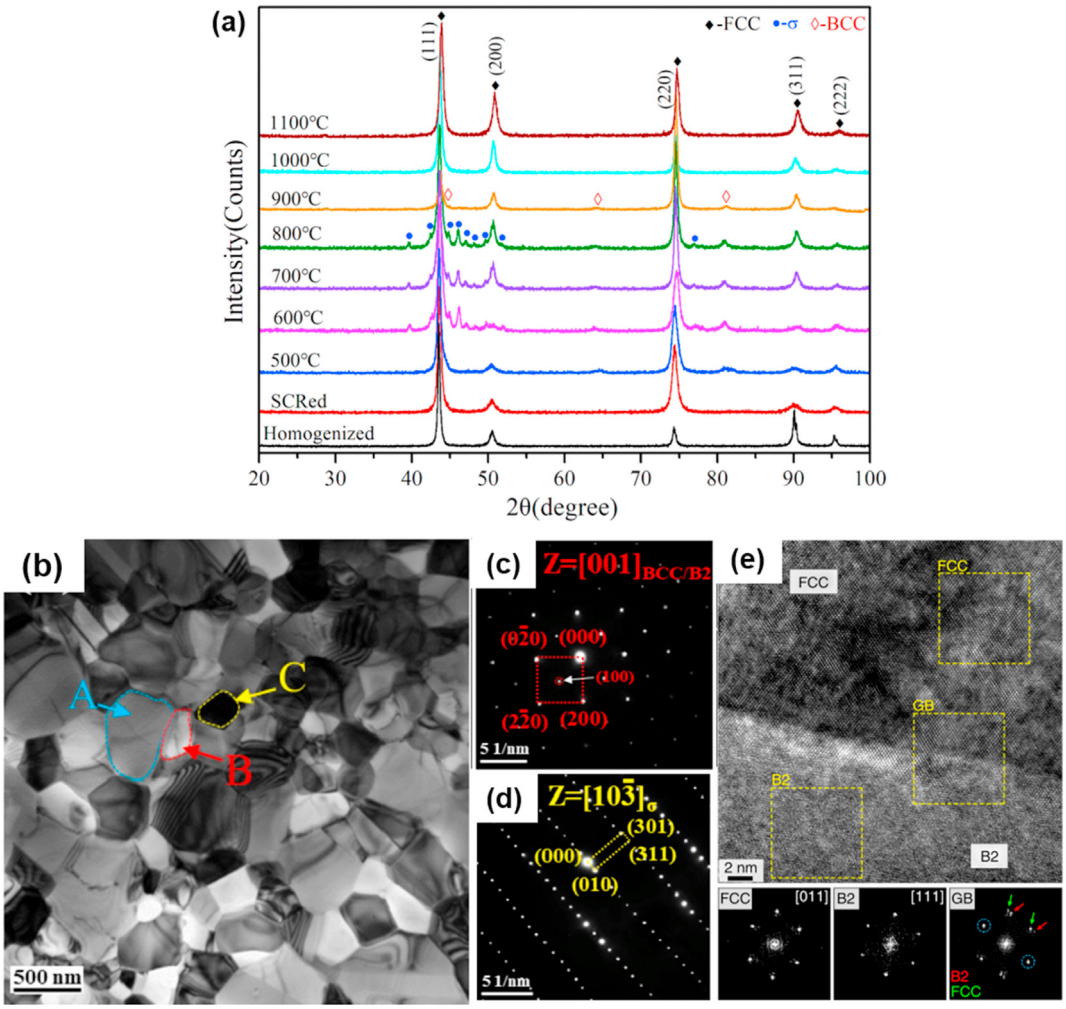

Fig. 45 – (a) X-ray diffraction patterns of the $Al_{0.3}$CoCrFeNiMn HEA after homogenizing and cold rolling followed by annealing at different temperatures [99], (b) bright-field TEM image for PDA at 800 °C [99], (c,d) corresponding selected area electron diffraction for *bcc-B2* and sigma particles [99] and (e) HRTEM image, Fast Fourier Transform (FFT) for the *bcc-B2* phase, the *fcc*-matrix, and the interface [133].

to 1150 °C. It is important to note that the C and O in this microstructure come from the process control agent. Thus, a good combination of strength and ductility including a YS of ~820 MPa, a UTS of ~980 MPa and a total elongation of ~11% were reported after HE at 1000 °C as shown in Fig. 34(b) [218].

There is a report of an investigation of the effect of adding different masses of Cr_2C_3 carbide to the CoCrFeNiMn HEA for creating a composite by SPS in which the microstructure included an *fcc* matrix and Cr_3C_2 or Cr_7C_3 before or after SPS, respectively, as in Fig. 35 [219]. It was claimed that the Cr_7C_3 carbide provides a higher hardness, more strength and excellent thermal stability which may enhance the wear resistance and strength of the CoCrFeNiMn matrix composite [227]. The compressive strength increased sharply by increasing the amount of Cr_3C_2 as in Fig. 35(c) but nevertheless the fracture toughness decreased. It was reported that the composite reinforced by Cr_7C_3 carbides exhibited outstanding performances including low density, high strength, excellent oxidation resistance and a wear resistance at high temperatures [219].

The effect of TiC carbide on the CoCrFeNiMn HEA was also investigated [220] and it was shown that the microstructure of this composite consisted of a fine-grained *fcc* of ~5 μm as the matrix, nano-TiC carbides of <100 nm along the grain boundaries and a small amount of oxide as in Fig. 36. It was suggested that the formation of a surface oxide during water atomization led to the observation of oxide peaks in the CoCrFeNiMn–TiC composite. Due to the high mixing enthalpy of TiC, it is the most stable carbide compared to all other carbides that were studied in the Cantor alloy [228]. An investigation of mechanical properties showed an increment in compressive strength with a fracture strength increase from ~1.5 to ~2.2 GPa and with no decrease in ductility through the addition of TiC of 5 wt. %. Additionally, the strain hardening rate was higher in the SPS HEA TiC composite. The high compressive strength and strain hardening rate were attributed to the higher volume fraction of interfaces. It is important to note that the TiC/matrix interfaces provide higher dislocation densities during deformation and the strain distribution after compressive deformation was not localized to

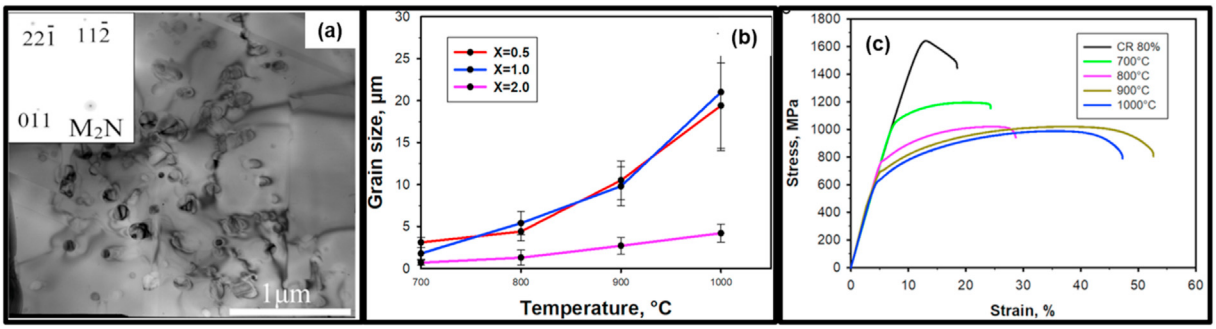

Fig. 46 – (a) TEM bright-field images of the $(CoCrFeNiMn)_{98}N_2$ HEA after post-deformation annealing at 900 °C [190], (b) grain growth curves for $(CoCrFeNiMn)_{100-x}N_x$ [190] and (c) room temperature tensile stress-strain curves of the $(CoCrFeNiMn)_{98}N_2$ HEA after and before post-deformation annealing [190].

the TiC/matrix interfaces leading to an enhanced strength without decreasing the ductility [220].

Another method to process this composite includes use of the MA and HPT procedures followed by post-deformation annealing [221]. The results from this approach show remarkable hardness together with a microstructure including an ultrafine-grained *fcc* of <1 μm, TiC carbides and also Cr-rich carbides [221].

The effect of SiC carbide on the mechanical properties and microstructure of the CoCrFeNiMn HEA was also investigated [222] where this composite is produced by MA followed by HIP [222,229]. The microstructure included an *fcc* solid solution, a sigma phase, *in situ* $M_{23}C_6/M_7C_3$ carbides and SiC particles of ~15–55 nm with the latter particles distributed along the grain boundaries of the *fcc* matrix as in Fig. 37 [222]. Additions of 5 wt.% of SiC nano-particles enhanced the compressive yield strength of the CoCrFeNiMn HEA from ~1180 to ~1480 MPa [222].

7. Excellent combinations of strength and ductility

Many attempts were conducted to fabricate the HEA with an excellent combination of strength and ductility. A summary of these results is illustrated in Fig. 38 which provides comprehensive data on the mechanical properties of the CoCrFeNiMn HEA after different strengthening processes as discussed in sections 4.3 and 5. These results suggest that the microstructure of the CoCrFeNiMn HEA has the potential for manipulation by changing the process parameters such as the amount of imposed strain, the annealing temperature and the time and deformation temperature in order to achieve an optimum condition that facilitates superior mechanical properties. The results show that an ultra-high tensile strength of ~1.8 GPa, a high ductility with a total elongation of ~90% and/or a good balance of mechanical properties including a UTS of ~1.25 GPa and total elongation of ~20% may be achieved in the CoCrFeNiMn HEA by microstructural engineering. Accordingly, this section focuses on the procedures which may be undertaken to improve the mechanical properties of the CoCrFeNiMn HEA.

7.1. *Heavy straining or SPD followed by annealing at 600–800 °C*

In section 4.3 it was stated that the benefits of the presence of precipitates can be used to increase the strength of the CoCrFENiMn HEA by applying heavy straining or SPD followed by annealing at <600 °C. However, this leads to a sharp increment in strength at the expense of a significant decrease of the ductility due to the lack of recrystallization at temperatures below 600 °C together with a high volume fraction of precipitates. Therefore, in order to optimize the mechanical properties, it is necessary to understand the microstructural evolution of the heavily deformed samples during annealing.

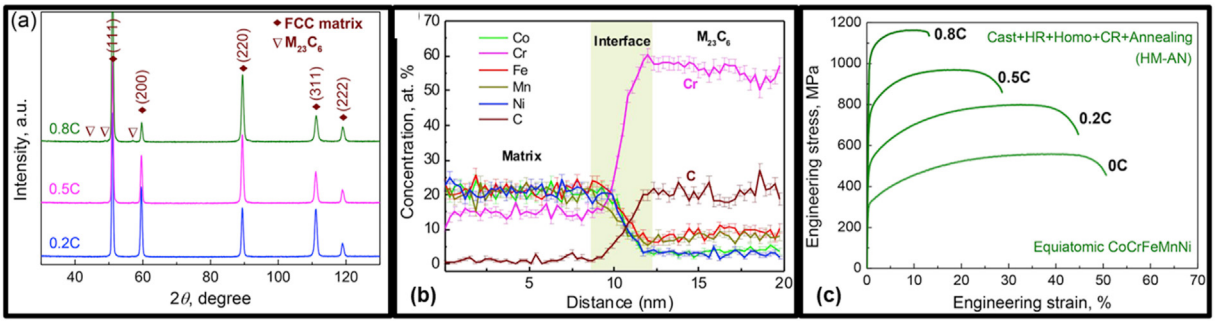

Fig. 47 – (a) X-ray diffraction patterns of the annealed interstitial HEAs in different amounts of carbon [151], (b) atomic probe tomography analysis revealing elemental distributions across a particle-matrix interface in $(CoCrFeNiMn)_{99.2}C_{0.8}$ HEA [151] and (c) room temperature tensile stress-strain curves of the $(CoCrFeNiMn)_{100-x}C_x$ HEAs (x = 0-0.8) after annealing at 900 °C [151].

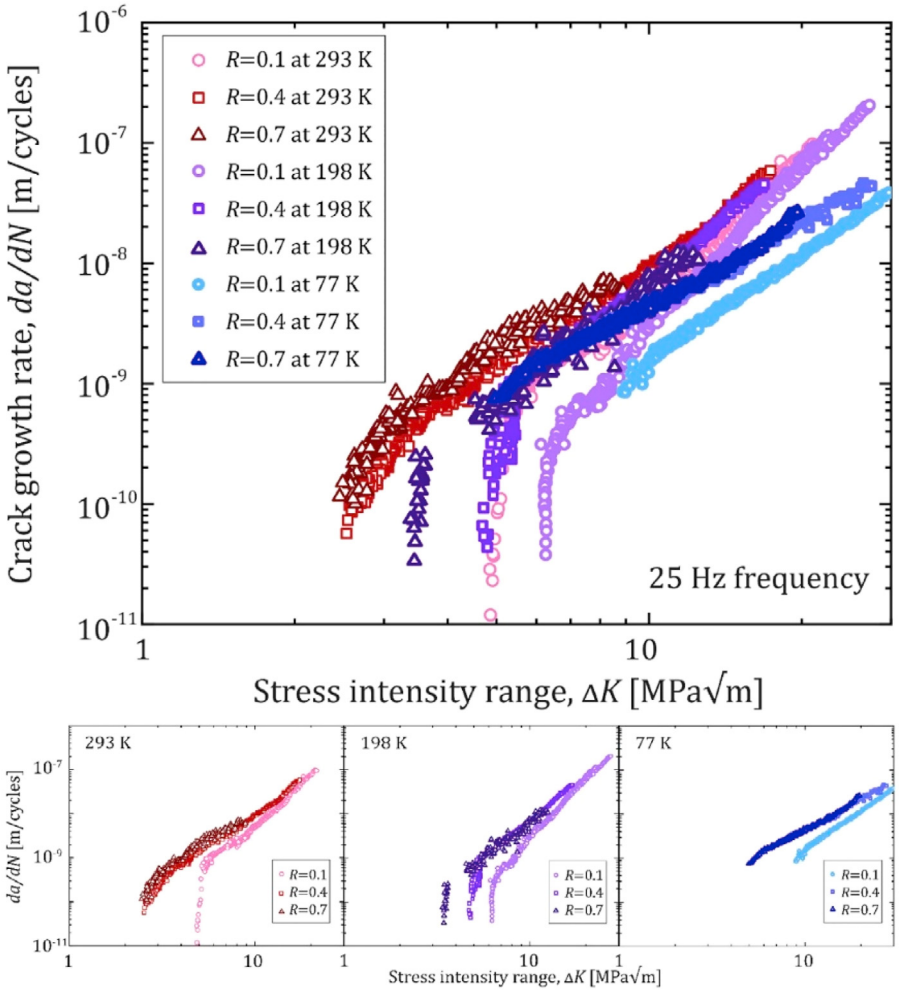

Fig. 48 – Fatigue-crack growth behaviour of the Cantor alloy tested at room temperature, 198 and 77 K [251].

This microstructural evolution is represented in Fig. 39 which determines the thermal stability of a heavily deformed CoCrFeNiMn HEA [34,52,85–87,104,230]. The results suggest there is no recrystallization in the temperature range of 450–550 °C [52,104]. In addition, *bcc* Cr-rich precipitates are formed even though sigma Cr-rich precipitates are not observed [104]. In the temperature range of 550–650 °C, partial recrystallization occurs together with a brittle sigma Cr-rich phase and *bcc* Cr-rich precipitates [86]. Some studies reported complete recrystallization and the formation of an ultrafine-grained microstructure in the temperature range between 650 and 750 °C [230] but nevertheless there are also some studies confirming partial recrystallization at these temperatures [34]. It was suggested that the recrystallization temperature is very high in this HEA at ~700 °C due to the sluggish diffusion, high lattice distortion energy and the low SFE [18,230–232]. In addition, in this temperature range most of the *bcc* Cr-rich precipitates are dissolved and only some sigma Cr-rich precipitates are present at the grain boundaries [34]. There are many reports which confirm the dissolution of precipitates, the existence of a single *fcc* phase and the activation of grain growth at temperatures above 800 °C [52,86,87,233].

Accordingly, the temperature range of 600–800 °C is mainly recommended in order to achieve remarkable mechanical properties with a good combination of strength and ductility [32,33,52,85,86]. The microstructure in this temperature range contains fine recrystallized grains, non-recrystallized regions in the deformed areas and also the presence of some Cr-rich precipitates where this is known as a heterogeneous microstructure. Figure 40(a) shows a plot of engineering stress versus engineering strain in different post-deformation annealing conditions of 750 and 850 °C which presents a good balance between strength and ductility at 750 °C due to preventing grain growth and the low volume fraction of brittle precipitates such as Cr-rich *bcc* precipitates [52]. The Temperature-Time-Transformation (TTT) diagram illustrated in Fig. 40(b) suggests that short-term annealing in the temperature range of 600–800 °C provides a microstructure containing an appropriate volume fraction of Cr-rich precipitates, fine recrystallized grain and also a non-recrystallized area which leads to superior mechanical properties [52].

Table 10 shows a summary of the mechanical properties of the CoCrFeNiMn HEA in different post-deformation annealing conditions to achieve optimal mechanical properties [32,33,52,55,85,86]. The results clearly confirm the importance

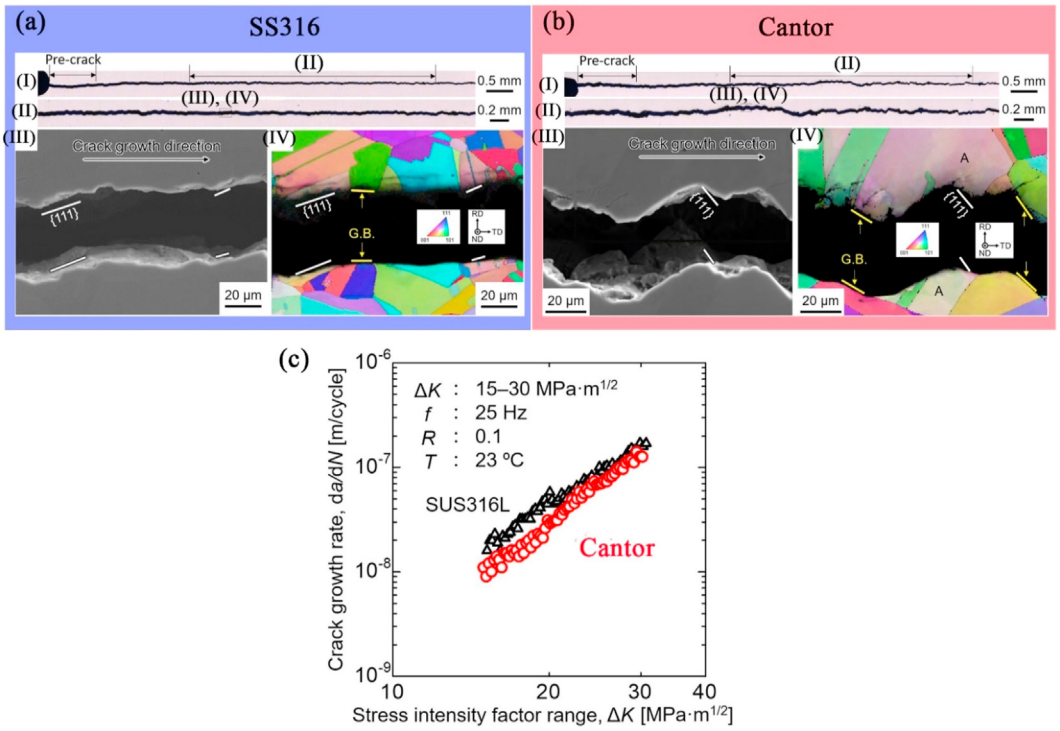

Fig. 49 – The deflection in fatigue crack of (a) SS316 and (b) the CoCrFeNiMn HEA in addition to (c) comparison of their fatigue crack growth rates plotted with respect to the stress intensity factor [254].

of the temperature range of 600–800 °C for post-deformation annealing in order to achieve superior mechanical properties. For example, the heavily cold-rolled alloy followed by annealing at 700 °C led to a tensile strength of ~1 GPa, a yield stress of ~930 MPa and a total elongation (TE) of ~20%. In this condition, a significant value of UTS*TE, a representative of

Table 10 – Summary of the available data for the CoCrFeNiMn HEA in different conditions.

Processing	Condition	T (°C)	Time (min)	YS (MPa)	UTS (MPa)	TE (%)	UTS*TE (MPa.%)	Ref.
HPT	5 turn/6 GPa/1 rpm	600	60	1010	1060	2	2120	[32]
		700	60	950	1030	21	21,630	
		800	10	680	830	65	53,950	
			30	570	725	78	56,550	
			60	530	680	80	54,400	
Shape Roll	97%	750	10	1020	1110	12	13,320	[52]
			30	970	1040	14	14,560	
			60	920	1000	20	20,000	
ECAP	2 passes/B_c route	600	60	820	880	41	36,080	[33]
		700	60	530	750	50	37,500	
	4 passes/B_c route	600	60	890	1010	6	6060	
		700	60	560	800	26	20,800	
Cold Roll	80%	600	60	1135	1260	6.7	8442	[85]
			3000	–	890	22	19,580	
		700	60	585	815	42.7	34,800	
		800	60	425	735	52.5	38,587	
Cold Roll	90%	600	60	1050	1080	10	10,800	[86]
		650	60	560	820	50	41,000	
		700	60	520	770	47	36,190	
		800	60	320	680	59	40,120	
Cold Roll	95%	600	60	1242	1325	4.4	5830	[55]
		650	60	930	1021	19	19,399	
		700	60	729	902	26.3	23,722	
		800	60	495	736	38.7	28,483	
Cold Roll	60%	600	30	1210	1250	7	8750	[235]

tensile toughness [52,234], can be achieved by this designated procedure on the CoCrFeNiMn HEA [55].

7.2. Significance of a bimodal microstructure

In sections 5.1 and 5.2 there are demonstrations of the importance of thermomechanical treatment including severe/heavy cold working followed by annealing at 600–800 °C to achieve remarkable mechanical properties. However, there are also many studies that demonstrate a deterioration effect of the brittle sigma phase formation at these temperatures [27,32]. As discussed in a previous sections, one way to achieve a good balance between strength and ductility is through the formation of heterogeneous microstructures and bimodal microstructures. A bimodal grain structure is defined as a composite structure in which different strengths and workabilities are carried by the coarse and fine grain regions [236]. In fact, high strength is provided by the fine grain regions but strain hardening arises from the coarser grains that are capable of accommodating many dislocations and improving the workability.

Fig. 41(a-c) represents the microstructures of a cold-rolled sample and an asymmetric cold-rolled sample after post-deformation annealing at 800 °C. The results show that the microstructure of the cold-rolled sample is fully homogeneous but a heterogeneous microstructure is observed in the microstructure of the asymmetric cold-rolled sample. The results of the mechanical properties show that the asymmetric cold-rolled sample has a tensile strength of ~930 MPa and an elongation to fracture of ~50%, whereas in the cold-rolled sample there is a tensile strength of ~700 MPa and an elongation to fracture of ~40%. This superior combination of strength and ductility for the asymmetric cold-rolled CoCrFeNiMn HEA implies the formation of a heterogeneous microstructure [91]. It was well established that plastic deformation firstly occurs in the large grains due to the lower yield strength during plastic deformation in heterogeneous microstructural materials so that, accordingly, larger plastic strains are accommodated in these regions [236–238]. The strain gradient due to a heterogeneous microstructure could constrain the geometrically-necessary dislocations that pile up at the interfaces, leading to a long-range back stress [239]. This back stress significantly increases the yield strength of the gradient microstructure materials [240,241]. Figure 41(d-f) shows a bimodal microstructure in a CoCrFeNiMn HEA fabricated by SPS [225]. The grain size distribution shows that 56% and 44% of the microstructure contains grains of sizes between 100 nm and 1 μm (ultrafine grain) and 1–5 μm (coarse grain), respectively. The results of tensile testing show significant mechanical properties including a UTS of ~1.1 GPa and a total elongation of ~20% [225]. It is important to note also that the coarse-grained CoCrFeNiMn HEAs have high ductility and low yield strength but nevertheless nanostructured CoCrFeNiMn HEAs exhibit high yield strength but low ductility. Accordingly, the production of ultrafine-grained HEAs or using a bimodal approach provide a better strength and ductility trade-off.

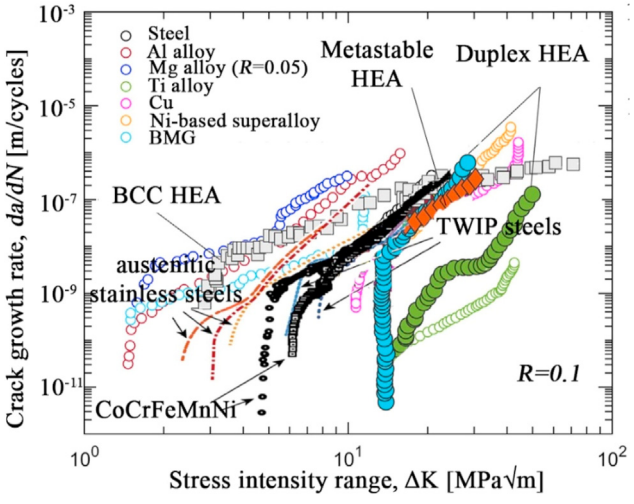

Fig. 50 – Comparison of the fatigue crack growth behaviour of the CoCrFeNiMn alloy with other engineering metals [250,259].

7.3. Light plastic deformation followed by low temperature annealing

Very recently, a new strategy was introduced to provide a good combination of strength and ductility in the Cantor alloy where a light plastic deformation was applied followed by annealing at low temperatures. The results show that this method is one of the simplest, and also one of the best, methods for achieving extraordinary mechanical properties. Fig. 42(a-d) shows the microstructure of a CoCrFeNiMn HEA after thermomechanical treatment, including a pre-strain using a tensile machine at a cryogenic temperature which led to the formation of deformation-induced twins, followed by a heat treatment at 500 °C [242]. Basically, deformation-induced twins can act as strong barriers against dislocation movement and this leads to an increase in the strength of the alloys [243]. Fig. 42(e) shows the dislocation density plot in terms of the value of the applied strain [244]. It was reported that the dislocation density decreases slightly and there is only partial recovery after annealing at 500 °C. A schematic of the resultant microstructure is shown in Fig. 42(f). The ability to increase the dislocation density in the recovered microstructure facilitates a significant strain hardening rate capability which ensures good tensile ductility. It was claimed that there was a good balance between the mechanical properties by applying a strain of 20% at a cryogenic temperature and post-deformation annealing at 500 °C including a yield stress of ~820 MPa and a uniform elongation of ~20% [242].

Figure 43 illustrates the microstructure after light cryogenic rolling followed by post-deformation annealing at 500 °C [27]. The results show that by applying a small strain of 28% area reduction at a cryogenic temperature (CT) many more deformation-induced twins are produced by comparison with similar straining at room temperature, where the ratios for these two procedures were ~7% and ~16%, respectively. Lowering the deformation temperature is beneficial by decreasing the SFE from ~21 mJ m^{-2} at RT to ~10 mJ m^{-2} at CT and this encourages deformation-induced twins rather than dislocation slip [20,40]. It is important to note that deformation-induced twins remain after annealing at 500 °C.

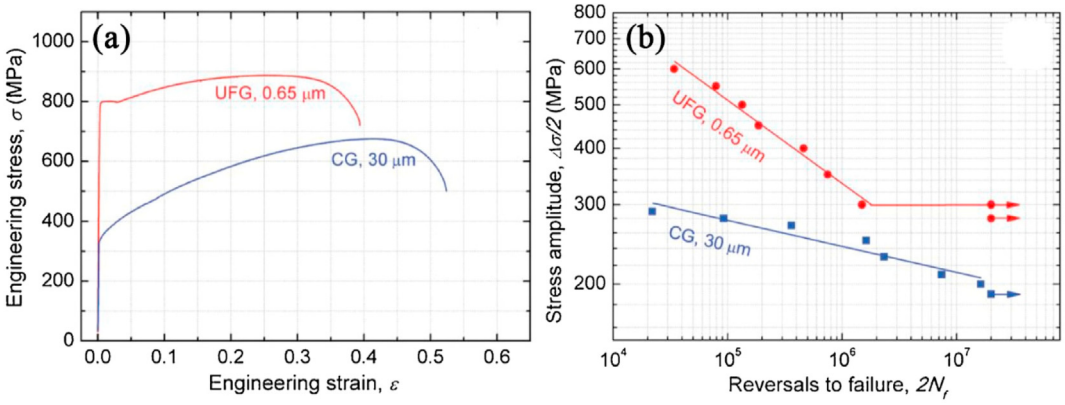

Fig. 51 – (a) Tensile stress-strain curves and (b) S–N curves of the ultrafine-grained CoCrFeNiMn alloy and its coarse-grained counterparts [162].

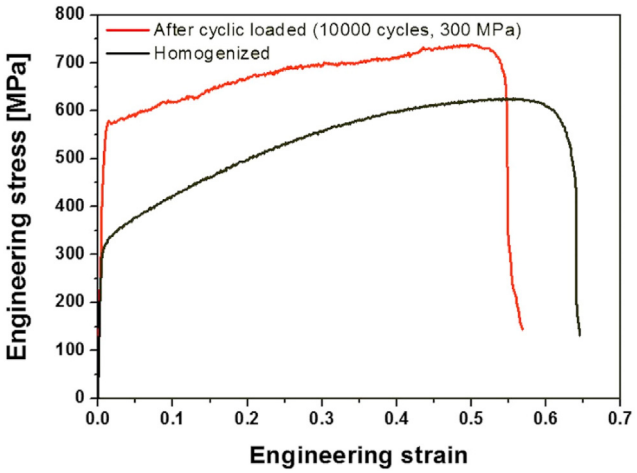

Fig. 52 – Engineering tensile stress-strain curves of the CoCrFeNiMn HEA before cyclic loading and after 10,000 cycles at σ_{max} = 300 MPa [98].

The results presented in Fig. 43(i,j) clearly show the formation of *bcc* Cr-rich precipitates after thermomechanical treatment which lead to the hardness increment (Fig. 43(k)). The peak hardening reveals that the particles have an optimum size and volume fraction in such a way that both dislocations cutting through particles or dislocations bowing around particles are active hardening mechanisms that contribute essentially evenly to the hardness peak value [104]. It is worth noting also that no sigma precipitates were detected in the microstructure.

Precipitates such as Cr-rich *bcc* and brittle sigma phases play the most important role in the mechanical behavior where, as already discussed, the latter is formed at higher temperatures of 600–800 °C than *bcc* precipitates. Fig. 43(l) illustrates schematically the microstructure after this procedure which displays different microstructural features including (a) sustained deformation-induced twins, (b) the prevention of the introduction of too many defects, (c) partial recovery, (d) the formation of nano Cr-rich *bcc* precipitates under optimum precipitation conditions and (e) the avoidance of the formation of the brittle sigma Cr-rich precipitates. This tailored microstructure provides extraordinary mechanical

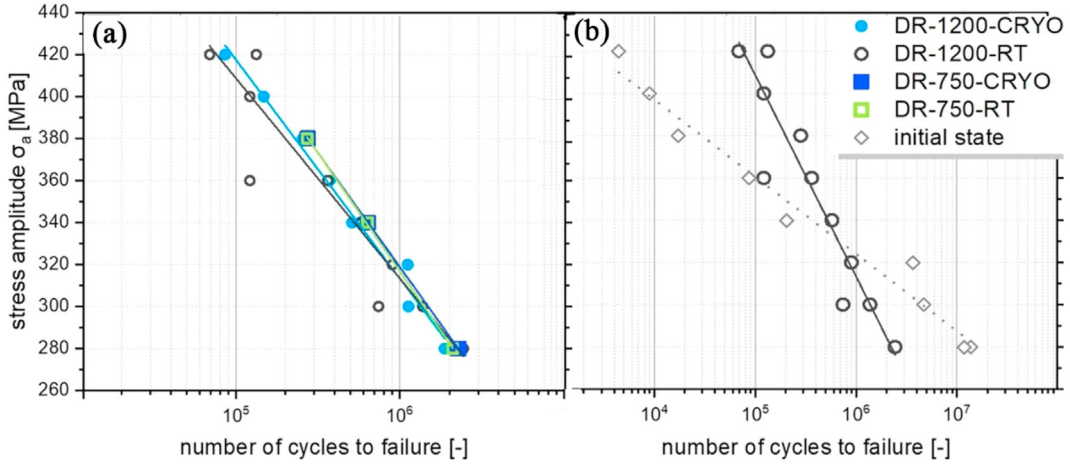

Fig. 53 – (a) The S–N curves of the untreated CoCrFeNiMn alloy (initial state) in comparison with that of deep rolled at room temperature with a load of 1200 N and (b) the S–N curves of surface-treated specimens under different conditions [263].

properties including a UTS of ~1.25 GPa and a total elongation of ~20%.

7.4. *The addition of a minor element followed by appropriate thermomechanical processing*

Another method of optimizing the mechanical properties of the CoCrFeNiMn HEA is by adding a minor element to the CoCrFeNiMn HEA, as discussed in section 5, followed by an appropriate thermomechanical process. It is important to note that the nature of the element added and the amount of the addition both have a significant effect on the type and the volume fraction of the secondary phases which play a key role in determining the mechanical properties of the material [139,168,245].

$CoCrFeNiMnTi_x$ (x = 0.1 and 0.3) alloys were processed by thermomechanical treatment including heavy cold rolling followed by post-deformation annealing at 500–900 °C for up to 60 min. The results suggested a significant enhancement in the mechanical properties with a combination of high

Table 11 – Mechanical properties of $(CoCrFeNiMn)_{100-x}E_x$ HEAs after different thermomechanical processing.

Alloying element		Processing	Annealing		Mechanical Properties			Ref.
E	X		T (°C)	Time (min)	YS (MPa)	UTS (MPa)	δ (%)	
Ti	2	Homogenized	–	–	320	540	80	[139]
		80% CR	600	60	650	760	3	[139]
			700	60	590	920	30	
			800	60	530	860	40	
			900	60	373	690	55	
		HPT	700	60	1490	1540	4	[129]
			750	60	1190	1220	25	
			800	60	910	1060	40	
			850	60	620	810	50	
	5.5	Homogenized	–	–	340	565	55	[139]
		80% CR	700	60	590	590	3	[139]
			800	60	530	530	3	
			900	60	618	990	7	
Al	5.5	80% CR	700	60	–	1320	2	[99]
			800	60	–	1100	7.5	
			900	60	–	850	11.5	
	9.1		1000	15	730	968	29.1	[135]
			1100	10	409	755	43.9	
			1200	5	278	619	60.4	
Nd	0.1	80% CR	900	60	219	590	56	[142]
	0.5		900	60	270	700	46	
	1		900	60	322	820	35	
N	0.5	80% CR	700	60	579	864	57	[190]
			800	60	464	798	58	
			900	60	326	702	65	
			1000	60	248	638	69	
	1		700	60	604	894	45	
			800	60	539	900	56	
			900	60	453	852	60	
			1000	60	336	770	66	
	2		700	60	985	1195	16	
			800	60	726	1020	24	
			900	60	673	1021	47	
			1000	60	570	988	42	
N	0.5	80% CR	900	2	–	840	43	[184]
			900	30	–	730	48	
N	1	60% CR	500	60	1125	1150	7	[145]
			600	60	1100	1120	5	
			700	60	875	1020	20	
			800	60	450	800	42	
			900	60	400	770	50	
N	2	90% CR	750	60	706	920	46	[246]
			850	60	556	840	51	
			900	60	444	798	60	
			950	60	362	744	68	
			1000	60	254	710	69	
C	0.2	60% CR	900	3	–	800	45	[151]
	0.5		900	3	–	975	28	
	0.8		900	3	–	1165	14	

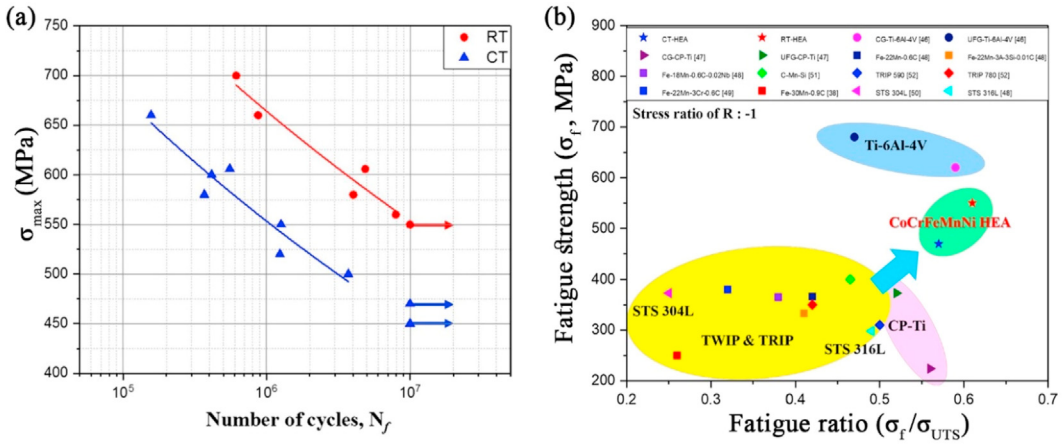

Fig. 54 – (a) The S–N diagram of the cryogenic (CT) and room temperature (RT) pre-strained CoCrFeNiMn alloy and (b) their fatigue strength by comparison with other engineering alloys [261].

strength and ductility. The initial microstructures of senary alloys consisted of a single *fcc* phase while post-deformation annealing led to the formation of a complicated microstructure due to precipitation and recrystallization. It was reported that adding Ti promoted the thermal stability of precipitates as in Fig. 44 and postponed recrystallization and grain growth by solute drag and Zener pinning. Fig. 44(c-i) shows the microstructure of $CoCrFeNiMnTi_{0.1}$ and $CoCrFeNiMnTi_{0.3}$ alloys after post-deformation annealing at 800 °C in which Cr-rich precipitates are distributed in the fully recrystallized microstructure of the $CoCrFeNiMnTi_{0.1}$ HEA [168]. Nevertheless, the microstructure of the $CoCrFeNiMnTi_{0.3}$ alloy after a similar procedure indicates the formation of η-Ni_3Ti precipitates due to a high ΔH_{mix} between Ni and Ti (-34.5 kJ mol^{-1}) together with Cr-rich precipitates [138,168]. Fig. 44(g) shows a representative HRTEM image corresponding to the matrix and Ni_3Ti precipitates and Fig. 44(h,i) illustrates Fast Fourier Transforms (FFT) of the two phases. The results indicate an orientation relationship of $(1\bar{1}1)$ *fcc* $\|(0001)_\eta$ and 011 *fcc* $\|2\bar{1}\bar{1}0_\eta$ between the precipitate and the matrix which suggests a coherent interface between the two phases [168].

The presence of coherent precipitates in the microstructure can have a significant impact on the mechanical properties. The $CoCrFeNiMnTi_{0.3}$ alloy presented high strength even after annealing at 900 °C due to the stability of the Cr-rich precipitates at this elevated temperature. However, a similar procedure led to the dissolution of precipitates which facilitated coarsening and reduced the strength significantly in the alloy with the lower amount of Ti. The latter alloy showed remarkable mechanical properties with a tensile strength and total elongation of ~900 MPa and ~30%, respectively, after annealing at 700 °C [139,168]. It is important to note that the *fcc* phase of the Cantor alloy is capable of dissolving substantial amounts of titanium up to 5.5 at.% ($CoCrFeNiMnTi_{0.3}$) and the matrix repulses extra titanium to encourage the formation of the brittle sigma phase in the $CoCrFeNiMnTi_{0.4}$ alloy [138].

A $CoCrFeNiMnAl_{0.3}$ HEA was subjected to thermomechanical processing to develop a material with superior mechanical properties [99,133]. Fig. 45(a) shows the XRD patterns of the $CoCrFeNiMnAl_{0.3}$ HEA in homogenized, heavily deformed, and post-deformation annealing conditions. In this material, sigma and *bcc* precipitates appeared at 600 °C and these phases are stable up to 900 °C. These phases are shown in Fig. 45(b,c,d) after annealing at 800 °C. Chemical analyses suggest that the *bcc* precipitates are Ni and Al in the NiAl

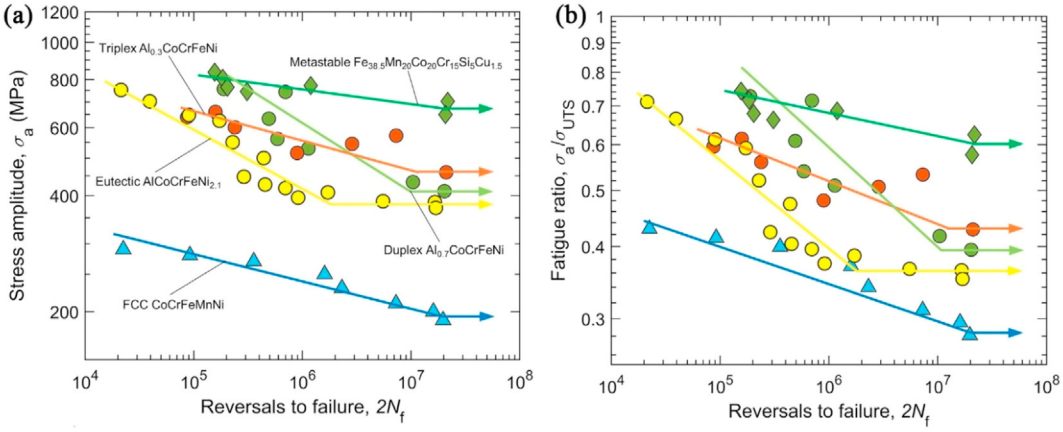

Fig. 55 – (a) The stress amplitude and (b) fatigue ratio versus number of reversals to failure of the Cantor alloy by comparison to other HEAs [259].

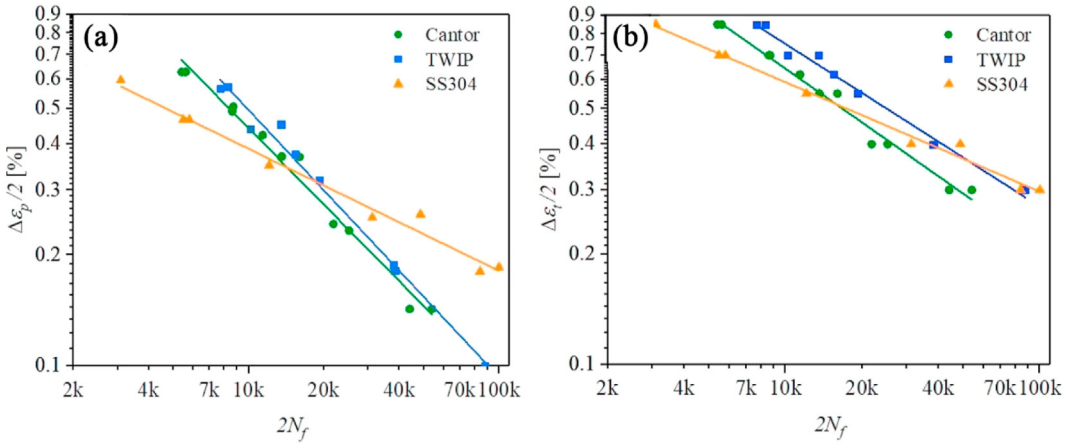

Fig. 56 – LCF life of the Cantor alloy compared with TWIP steel and SS304 based on (a) plastic strain amplitude and (b) total strain amplitude [264].

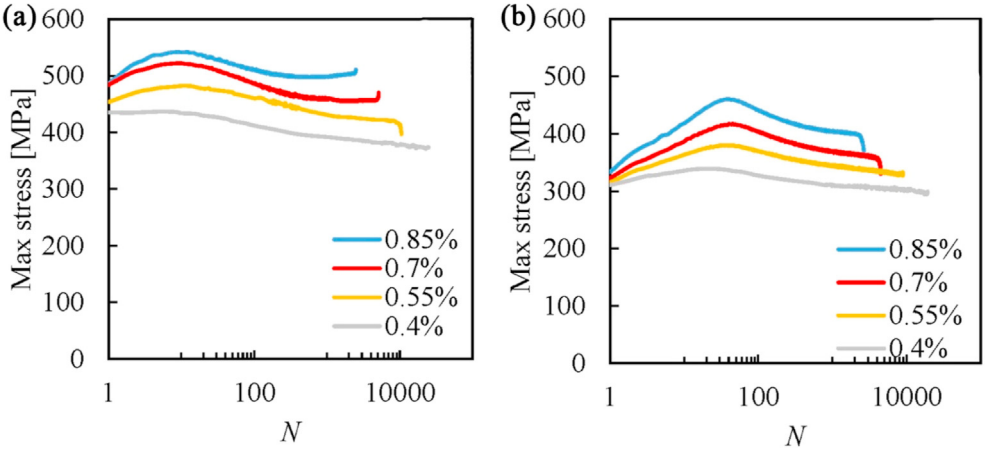

Fig. 57 – Cyclic stress response at different strain amplitudes of the Cantor alloy with grain sizes of (a) ~10 μm and (b) ~66 μm [265].

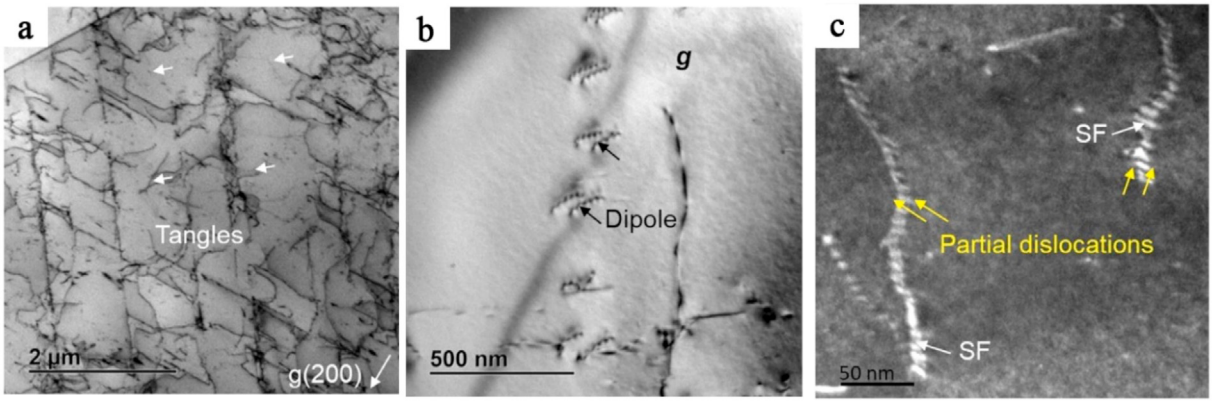

Fig. 58 – TEM micrographs revealing (a) dislocation tangles, (b) dipoles, and (c) stacking faults in the Cantor alloy (GS ~ 6 μm) after 20 cycles at $\frac{\Delta\varepsilon_t}{2} = 0.5$ % [267].

phase [99]. The formation of this phase is expected due to the high ΔH_{mix} between Ni and Al of −22.3 kJ mol^{-1}. In another study it was shown that NiAl precipitates in a $(CoCrFeNiMn)_{91}Al_9$ HEA after post-deformation annealing at 800 °C have a coherent interface with the matrix and their orientation relationship is Kurdjumov–Sachs as shown in Fig. 45(e) [133]. In another investigation, a $CoCrFeNiMnAl_{0.32}$ HEA (6 at.% Al) alloy was subjected to thermomechanical processing including cold rolling of 80% followed by annealing at 900 °C for 5 min which provided a heterogeneous microstructure containing 60% recrystallized grains and 40% non-recrystallized grains, *B2* and sigma precipitates. This heterogeneous microstructure exhibited remarkable mechanical properties including a UTS of ~1.2 GPa and a uniform elongation of ~10% [136]. It was claimed that the remarkable strengthening of the heterogeneous microstructure was due to the deformed area of non-recrystallized grains [136].

Recently, there was an investigation of the effect of the synergistic addition of both Al and Ti and thermomechanical processing of the CoCrFeNiMn HEA [137]. Microstructural analyses showed the formation of sigma Cr-rich and *B2* precipitates during thermomechanical processing in the $(CoCrFeNiMn)_{95.2}Al_{3.2}Ti_{1.6}$, which is similar to the effect of Al. Remarkable mechanical properties including a UTS of ~1050 MPa and a total elongation of ~15% were reported after post-deformation annealing at 800 °C. The mechanisms behind these mechanical properties are the partially recrystallized microstructure, precipitation hardening and maintaining a moderate ductility due to the less brittle character of the *B2* phase by Ti alloying [137].

Recently, a new method was used to increase the strength of the CoCrFeNiMn HEA by the addition of an interstitial element, as for example *N* and *C*, and thermomechanical processing [151,177,184,190]. Fig. 46(a) shows the microstructure of a nitrogen-containing CoCrFeNiMn HEA ($(CoCrFeNiMn)_{98}N_2$) after thermomechanical processing including heavy cold rolling followed by annealing at 900 °C [190]. The results demonstrate the formation of M_2N (M: Cr, Fe, Mn, Co and Ni) particles during thermomechanical processing, and the volume fraction of these phases increases as the amount of nitrogen is increased. The strong affinity and high solubility of N with Cr were responsible for the formation of Cr–N type nitrides in the N-containing CoCrFeNiMn HEA [246]. It is important to note that nitrides in the form of Cr_2N are formed more favorably in the Co–Cr–Fe–Ni–Mn system because of the lower Gibbs free energy of formation of Cr_2N compared to that of CrN [193,247]. These particles prevent grain growth due to their strong pinning effect as shown in Fig. 46(b) [190]. It was reported that post-deformation annealing at 700 °C led to a remarkable UTS of ~1.2 GPa and an acceptable total elongation of ~20% in the $(CoCrFeNiMn)_{98}N_2$ HEA as shown in Fig. 46(c) [190]. It was also noted that the addition of N significantly increases the strength of the alloy without significantly decreasing the ductility by increasing lattice frictional forces and maintaining planar slip and twinning [184]. In addition, it was reported

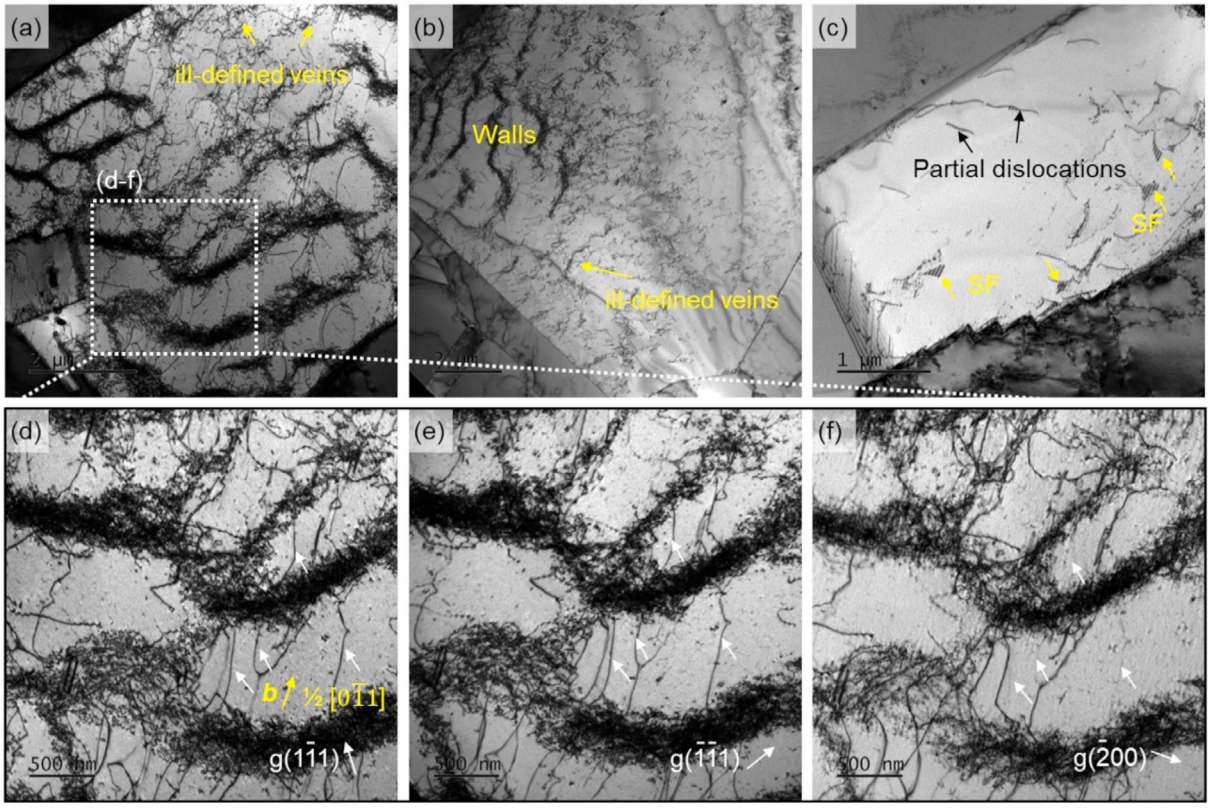

Fig. 59 – Microstructure of the Cantor alloy with a grain size of ~6 μm after 500 cycles at $\frac{\Delta\varepsilon_t}{2} = 0.5$ % [267].

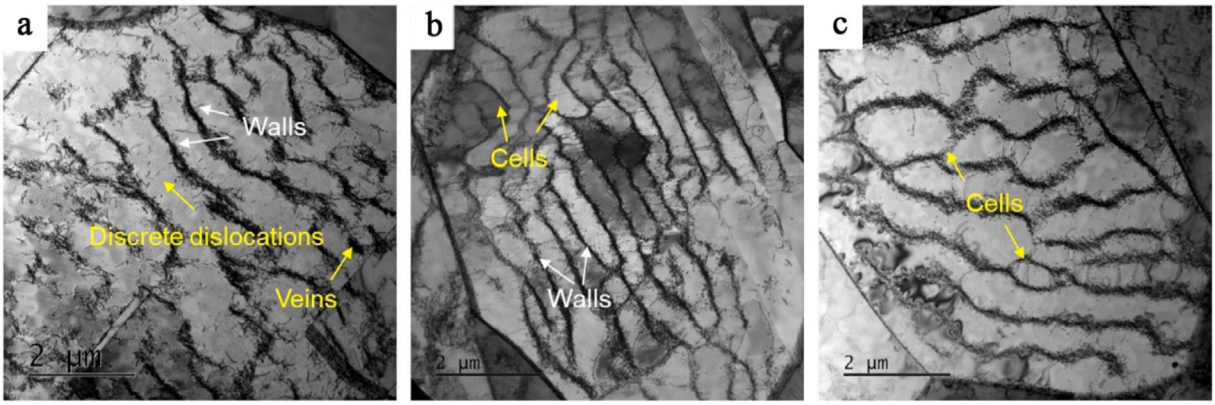

Fig. 60 – Microstructure of the Cantor alloy with a grain size of ~6 μm after fatigue failure at $\frac{\Delta\varepsilon_t}{2} = 0.5$ % [267].

that the presence of N in the CoCrFeNiMn HEA can prevent the formation of undesirable brittle sigma phases in the low temperature annealing [177].

Fig. 47 illustrates information on the $(CoCrFeNiMn)_{100-x}C_x$ (x = 0.2–0.8) HEAs subjected to thermomechanical treatment [151]. These results indicate the formation of nano $M_{23}C_6$ carbides (M: Cr, Fe, Mn, Co, and Ni) during post-deformation annealing in which increasing amounts of carbon improve the strength at the expense of decreasing ductility [151].

Table 11 summarizes the effect of different interstitial and substituents elements and subsequent thermomechanical treatment on the mechanical properties of the CoCrFeNiMn HEA [99,129,139,142,151,184,190]. The results demonstrate that a wide range of strength and ductility can be achieved by

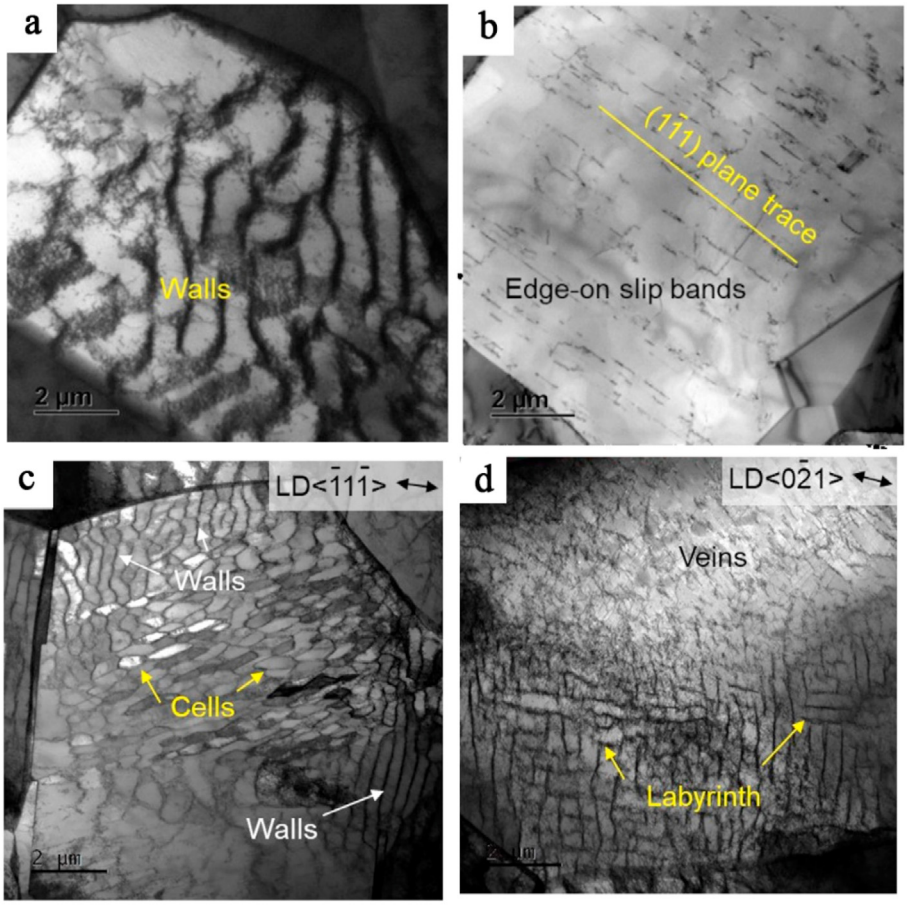

Fig. 61 – TEM micrographs after fatigue failure of the Cantor alloy with a grain size of ~6 μm at (a–b) $\frac{\Delta\varepsilon_t}{2} = 0.3\%$ and (c–d) $\frac{\Delta\varepsilon_t}{2} = 0.7$ % [267].

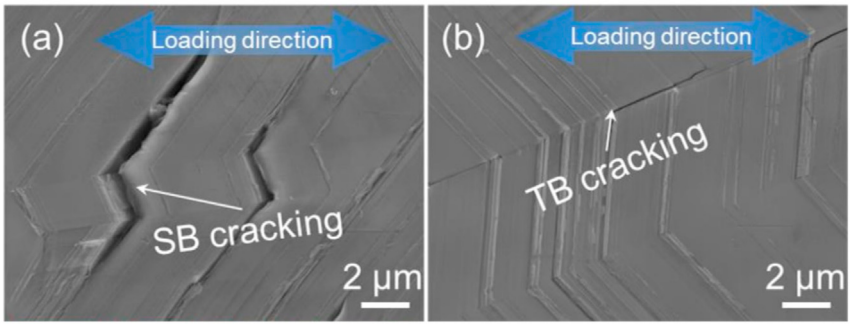

Fig. 62 – Fatigue crack initiation along (a) slip-bands and (b) TBs during LCF test in the CoCrFeNiMn alloy [272].

adding an element and conducting appropriate thermo-mechanical treatment in the CoCrFeNiMn HEA.

8. Cyclic deformation behaviour and fatigue resistance

Most materials generally experience cyclic loading rather than monotonic loading in typical engineering applications and the accumulated damage because of this cyclic loading is then the main reason for failure. Therefore, the cyclic deformation behaviour is a very important area of study for HEAs and in practice research on the fatigue behaviour of HEAs was commenced less than a decade after their discovery [248]. The initial studies showed that HEAs had an encouraging fatigue endurance limit under cyclic bending loads [248,249] and high fatigue thresholds, ΔK_{th}, in fatigue-crack growth tests.

8.1. *Fatigue-crack growth*

The first study of fatigue behaviour in the Cantor alloy was conducted by fatigue-crack growth tests with a constant load ratio of $R = 0.1$ at −75 and 20 °C [250] and this study was

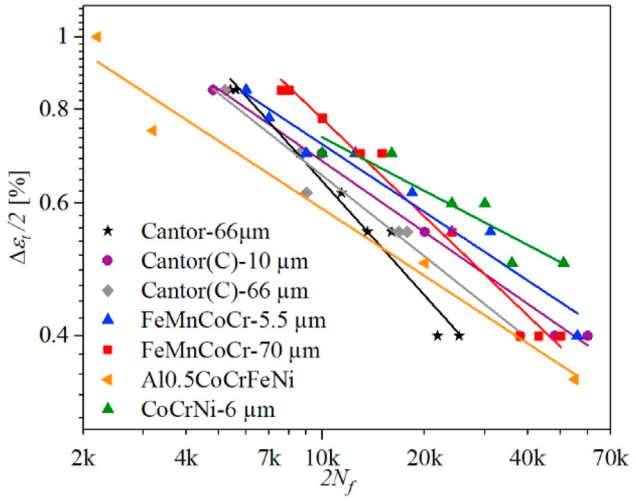

Fig. 63 – Comparing the LCF life of the Cantor alloy with other studied HEAs [264–266,276].

further developed at other stress ratios and at a lower temperature of −196 °C [251]. Although the fatigue-crack growth rate at the high stress intensity ranges showed no change by decreasing the temperature from 20 to −75 °C, it was decelerated significantly at −196 °C as shown in Fig. 48. Moreover, changing the test temperature from 20 to −75 °C enhanced ΔK_{th} by 30% from ~4.8 to ~6.3 MPa $\sqrt{}$ m at $R = 0.1$. Increasing the load ratio, as in other materials, led to faster fatigue-crack propagation in the alloy at all testing temperatures as shown in Fig. 48. Geometrically-necessary dislocations emitted from the crack tip during cyclic loading can result in plastic deformation in the grains that neighbour the crack path. Furthermore, local deviations from a straight crack path and a physical contact of the mating crack surfaces can produce a plastically-deformed area. This phenomenon, which was named roughness-induced fatigue crack closure, can decrease the crack growth driving force at the tip of the crack especially near threshold levels [252]. Despite a lower yield strength at room temperature than at 198 K, the physical contact of the crack mating surfaces flattens more the crack path locally and this leads to faster crack growth at room temperature as in Fig. 48 [253].

The occurrence of deflection is the other feature of fatigue-crack propagation during its progress. Thus, although the fatigue-crack followed a transgranular path in the alloy at room temperature, an intergranular character was detected at a temperature of 198 K [250]. Thus, there is a greater deviation in the crack path because of intergranular crack propagation and this significantly promotes a roughness-induced fatigue crack closure at lower temperatures. This can be the main reason for an enhanced ΔK_{TH} value at 198 K compared with 293 K.

The observed deflection in fatigue-cracks of the CoCrFeNiMn HEA was more significant than in an austenitic stainless steel (SS316) as shown in Fig. 49(a-b) [254]. Furthermore, the fatigue-crack path in the Cantor alloy was along the dislocation cell structure boundaries and this was different from that of the SS316 steel in which blunting/re-sharpening was the dominant mechanism [254]. Therefore, the better fatigue-crack growth resistance of the Cantor alloy than SS316 in Fig. 49(c), despite the lower SFE of the latter, is related to the greater activation of the roughness-induced fatigue crack closure effect in the CoCrFeNiMn HEA.

Deformation twinning was considered the main mechanism for fracture toughness resistance of the Cantor alloy [12]

but it was not detected either at room temperature or at −75 °C at $R = 0.1$ and it was claimed that the imposed cyclic stress was not sufficiently high to activate deformation-induced twins [250]. However, decreasing the test temperature to −196 °C and increasing the load ratio to $R = 0.7$ led to deformation twinning near fatigue cracks [251]. In addition, the fracture surfaces were mostly occupied by periodic striations that were associated with cyclic slip steps due to the advent of planar slip. Therefore, despite some deformation twins observed at cryogenic temperatures, the main cyclic deformation mechanism of the Cantor alloy is planar slip and the improved fatigue-crack growth resistance of the alloy at lower temperatures relates to an enhancement of the roughness-induced fatigue crack closure effect [251].

The Cantor alloy exhibits a high planarity of dislocation slip during monotonic loading [255] and this characteristic can delay the self-accommodation of local stress which increases the stored strain energy and prevents further motion and multiplication of dislocations [256]. The planarity of slip hampers dislocation annihilation and facilitates fatigue-crack nucleation on a single slip plane and leads to a higher volume fraction of cracks in the Cantor alloy than in a stainless steel with a similar SFE [257]. However, the fatigue-crack initiation time was longer in the CoCrFeNiMn HEA than in stainless steel due to the higher proof stress and the greater work hardening effect of the HEA [257]. Nevertheless, slip planarity led to better fatigue-crack propagation resistance in the Cantor alloy than in stainless steel due to the activation of a different mechanism. The damage accumulation fatigue-crack propagation mechanism (Mode II) was more prevalent in the HEA than the usual plastic deformation crack growth mechanism (Mode I) [258]. In contrast to Mode I that is driven by dislocation emission from the crack tip, the Mode II type is associated with an accumulation of dislocations on limited slip planes [257]. However, as the fatigue-crack becomes longer so the effect of slip planarity is weakened, the crack is propagated in Mode I and fatigue striations appear on the fracture surface.

The fatigue-crack growth resistance of the Cantor alloy is compared with other engineering alloys and HEAs in Fig. 50 [250,259]. Although the fatigue-crack growth resistance of the CoCrFeNiMn HEA outperforms that of austenitic stainless steels, single-phase BCC HEAs, and Al and Mg alloys, it was similar to those of TWIP steel and less than for the Ni-base superalloy, copper, titanium alloy and duplex and metastable HEAs as shown in Fig. 50 [250,254]. Accordingly, the CoCrFeNiMn alloy exhibits an intermediate fatigue-crack growth resistance and therefore, in order to reach a superior fatigue resistance, duplex and metastable HEAs should be developed.

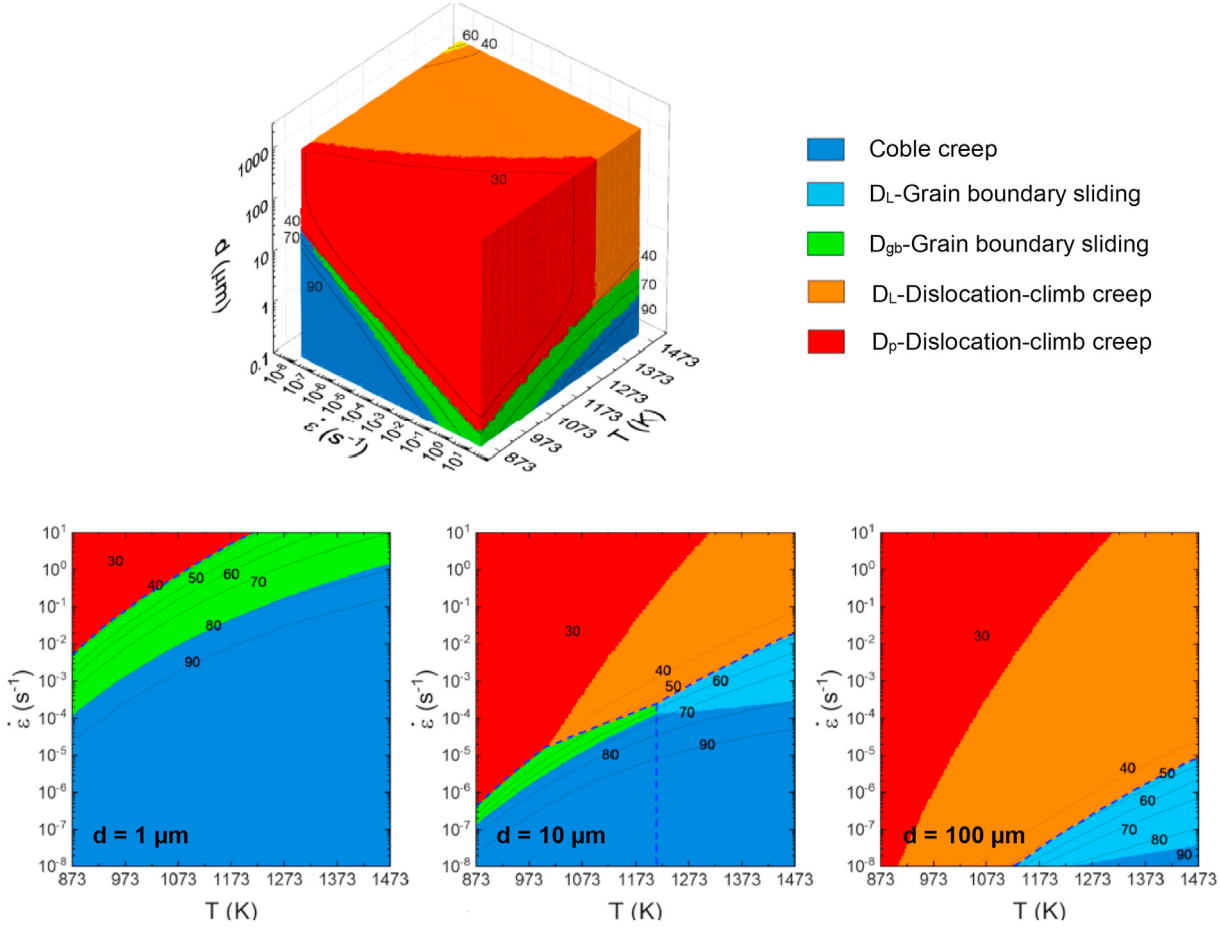

Fig. 64 – A 3D processing map plotted as a function of grain size (upper) and processing maps constructed at different grain sizes of 1 μm, 10 μm and 100 μm in 2D (lower) for the CoCrFeNiMn HEA [284].

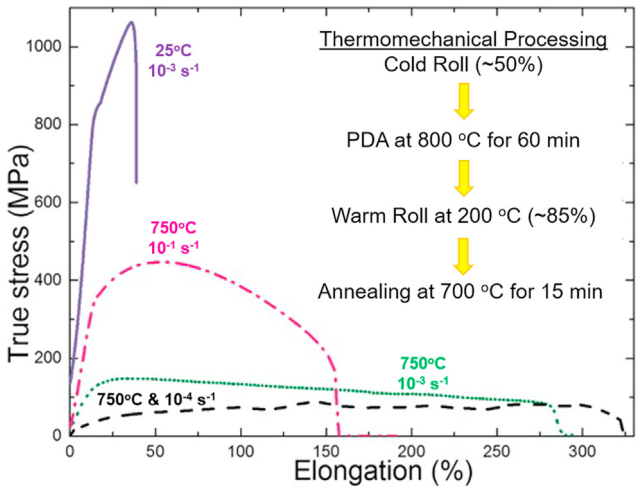

Fig. 65 – True stress–elongation (%) curve at room temperature and 750 °C for different strain rates [295].

8.2. *High-cycle fatigue*

When the imposed cyclic stress is predominantly elastic and the material can survive more than 10^4 cycles, loading is located in the high-cycle fatigue (HCF) region. The stress-life approach, as in the conventional S–N curve, that is usually employed at this loading condition uses the Basquin equation to compare the behaviour of materials [260] so that

$$\frac{\Delta\sigma}{2} = \sigma_f'(2N_f)^B \tag{9}$$

where $\Delta\sigma$ is the imposed stress amplitude, N_f is the number of reversals, and σ_f' and B are the fatigue-strength coefficient and exponent, respectively.

In the first reported HCF test of the CoCrFeNiMn alloy, the fatigue behaviour of an ultrafine-grained structure with d = 0.65 μm was compared with its coarse-grained counterpart with d = 30 μm as shown in Fig. 51 [162]. The uniform grain size distribution of the ultrafine-grained microstructure with its higher strength level in Fig. 51(a) led to a superior HCF resistance than for the coarse-grained structure. The unexpectedly lower B value of the ultrafine-grained structure

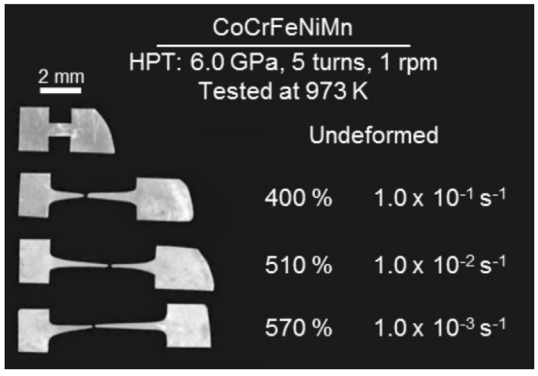

Fig. 66 – Examples of superplasticity in the Cantor alloy after processing by HPT and then testing in tension at a temperature of 700 °C [294].

where $B = -0.187$ compared with a value of $B = -0.058$ for the coarse-grained structure at $R = -1$ was attributed to the pre-existing cracks that were developed during the cold-rolling process.

A similar fatigue strength exponent to the coarse-grained microstructure, with −0.08 <B < −0.09, was achieved by HCF testing on the CoCrFeNiMn alloy with a grain size of 10–15 μm in another study [261]. Although, the fatigue strength, σ_f, of the coarse-grained structure at 190 MPa was less than for the ultrafine-grained structure where the value is 280 MPa, they had comparable fatigue ratios, defined as $r = \frac{\sigma_f}{\sigma_{UTS}}$. However, another HCF study with $R = 0.1$ reported $\sigma_f = 280$ MPa and $B = -0.19$ for a grain size of ~245 μm [98].

The role of deformation twins in the fatigue is another debate. Deformation twins unexpectedly formed during HCF tests [98,262] at stress levels that were below the critical stress for the initiation of deformation twins in monotonic loading [23]. Stacking faults were proposed as the nuclei for the formation of deformation twins in metals with an *fcc* crystal structure [69]. Therefore, the formation of stacking faults that is possible at cyclic stress levels less than the critical stress for deformation twins in monotonic loading was suggested as the reason for observing deformation twins during the HCF tests [98]. The much higher tensile strength that was achieved by interrupting the HCF after 10,000 cycles at $\sigma_{max} = 300$ MPa was attributed to mechanical twins that were formed during cyclic loading as represented in Fig. 52. Thus, it was claimed that these mechanical twins contributed to the HCF resistance of the CoCrFeNiMn alloy.

In a more recent study [263], it was shown that the HCF life of a CoCrFeNiMn alloy that was surface-treated by deep rolling at cryogenic or room temperatures was similar as in Fig. 53(a). Although the deformation twins were absent before HCF in the latter, large numbers of deformation twins were detected on the surface of the former. Therefore, deformation twins near the surface made no contribution to either improving or reducing the fatigue life in this condition. The residual compressive stress that is imposed by a surface treatment may delay fatigue at high stress values by changing the crack initiation sites from the surface to the interior as in Fig. 53(b). However, a surface treatment is harmful for the fatigue-crack growth resistance at lower stress levels because the fatigue cracks are already initiated in the interior at low stresses in the untreated specimen and deep-rolling produces residual tensile stresses in the interior [263].

The deteriorating effect of deformation twins on HCF of the CoCrFeNiMn alloy was reported in another study performed by rotational bending fatigue testing [261]. A pre-straining at room temperature and cryogenic conditions were chosen as the methods to make a dislocation cell structure and deformation twins in the CoCrFeNiMn alloy, respectively. A similar strength level was achieved in both conditions by controlling the value of the imposed pre-strains. A large quantity of voids was formed during HCF testing at the intersection of deformation twins and grain boundaries in the specimens pre-strained at −196 °C. Therefore, deformation twins that prevented reversibility of dislocations during HCF tests also accelerated the fatigue-crack initiation and this led to a lower fatigue life as in Fig. 54(a). Moreover, the wider striation

spacing on the fracture surface showed that the fatigue-crack growth rate was much higher in the specimen pre-strained at −196 °C than in the specimen tested at room temperature. Although pre-straining at cryogenic conditions decreased the HCF resistance of the CoCrFeNiMn alloy, it showed a much better fatigue limit than most other engineering alloys such as stainless steels, TWIP steels and pure titanium as demonstrated in Fig. 54(b). However, the Cantor alloy has inferior fatigue resistance as in Fig. 55(a) and fatigue ratio as in Fig. 55(b) by comparison to duplex and metastable HEAs and this is similar to the fatigue-crack growth test results in Fig. 50 [261].

8.3. *Low-cycle fatigue*

When the cyclic loading leads to significant plastic deformation, the material fails by low-cycle fatigue (LCF). Since it is easier in practice to maintain a specific strain than stress at each cycle of an LCF test, this experiment is usually conducted in a strain-controlled mode. The Coffin-Manson equation is then used to compare the fatigue behaviour in the strain-life approach [260] so that

$$\frac{\Delta\varepsilon_p}{2} = \varepsilon_f'(2N_f)^C \tag{10}$$

where $\Delta\varepsilon_p$ is the plastic strain amplitude, N_f is the number of reversals, ε_f' is fatigue-ductility coefficient and C is the exponent. Equation (10) and the following equation (11) deal with the elastic and plastic parts of the cyclic loads, respectively, and they are combined to reach a relationship that is useful over a wide range of loads so that

$$\frac{\Delta\varepsilon_t}{2} = \frac{\Delta\varepsilon_e}{2} + \frac{\Delta\varepsilon_p}{2} = \frac{\sigma_f'}{E}(2N_f)^B + \varepsilon_f'(2N_f)^C \tag{11}$$

where E is the elastic modulus and $\Delta\varepsilon_t$ and $\Delta\varepsilon_e$ are the total and elastic strain amplitudes, respectively. The reported fatigue parameters for the CoCrFeNiMn alloy with different grain sizes and test temperatures in the Coffin-Manson equation were given by $-0.46 \le C \le 0.55$ and $0.31 \le \varepsilon_f' \le 0.61$ [264–268].

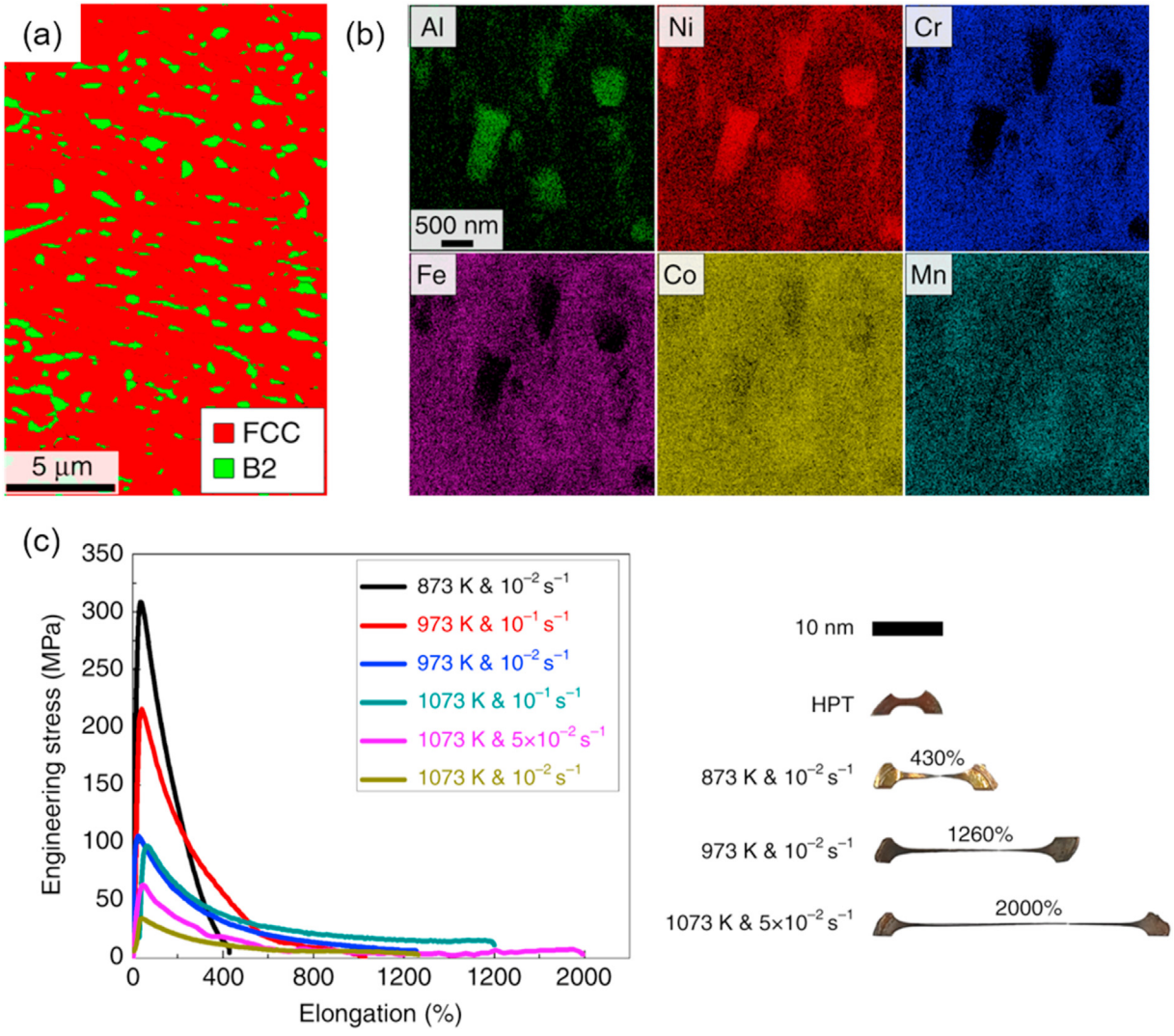

Fig. 67 – (a, b) Initial microstructure and elemental map chemical analysis of $Al_9(CoCrFeNiMn)_{91}$ HEA and (c) Tensile stress-strain curves with different strain rates for HPT-processed $Al_9(CoCrFeNiMn)_{91}$ HEAs [133].

In the first published study on LCF life for the CoCrFeNiMn alloy, its fatigue life and cyclic deformation mechanism were compared with those of two conventional counterparts, namely stainless steel 304 (SS304) and a TWIP steel [264]. As with the results of fatigue crack growth testing in Fig. 47, the LCF behaviour of the CoCrFeNiMn alloy was analogous to TWIP steel at the same grain size of ~65 μm in the Coffin-Manson plot as shown in Fig. 56(a). However, the cyclic strength of the CoCrFeNiMn alloy was lower than for TWIP steel and this led to an inferior performance based on $\Delta\varepsilon_t$ as in Fig. 56(b). When the amount of plastic strain increases, the strain-induced α'-martensite in SS304 significantly decreases its fatigue life by comparison to that of the HEA [264]. The higher yield strength and cyclic hardening ability of the CoCrFeNiMn alloy also led to a better LCF resistance than in SS316 with a similar SFE [267].

The cyclic stress response of the CoCrFeNiMn alloy with two different grain sizes are presented in Fig. 57. According to these plots, the cyclic deformation behaviour of the alloy can be divided into different stages. The first stage is hardening that is active for less than 100 cycles and becomes more significant at higher strain amplitudes. This initial hardening in metals with an *fcc* structure usually deals with interactions of statically stored dislocations [269]. TEM micrographs of the alloy with a grain size of ~6 μm at the end of this stage at an intermediate strain amplitude of $\frac{\Delta\varepsilon_t}{2} = 0.5$ % are shown in Fig. 58. Stacking faults, dipoles and dislocations are arranged in the form of tangles with planar slip bands formed in this condition. The dislocations in tangles have different Burgers vectors, *b*, suggesting that multiple slip systems are activated at this strain amplitude. However, planar slip bands consist of arrays of undissociated dislocations on primary slip systems [267].

The next stage of the cyclic stress response is softening in which dislocations are arranged into a substructure, such as ill-defined walls and veins as in Fig. 59(a-b). Stacking faults are also detected rarely at this stage in Fig. 59(c). There are different values of the Burgers vector in these substructures that became apparent by using a conventional *g.b* analysis as in Fig. 59(d-f) and this makes it clear that, in addition to cross-slip, multiple-slip is also active [267].

Microstructural evaluations after fatigue failure at $\frac{\Delta\varepsilon_t}{2} = 0.5$ % in Fig. 60 show well-developed dislocation substructures such as walls, veins and cells that indicate an activation of wavy slip at the last stage [267]. The near saturation state of the dislocations led to a dynamic equilibrium between the multiplication and annihilation of dislocations and a near steady-state condition at this last stage of cyclic stress as in Fig. 57. A secondary hardening is observed at high strain amplitudes in the fine-grained microstructure as in Fig. 57(a). The large number of grain boundaries in the fine-grained microstructures led to an increase in density of geometrically-necessary dislocations at the cell walls as the numbers of cycles increased. This may activate more dislocation cross-slip that will change cells to sub-grains and produce hardening in finer grain size microstructures [265,270].

The microstructures observed in Figs. 58–60 belong to an intermediate strain amplitude where $\frac{\Delta\varepsilon_t}{2} = 0.5$ %. Although dislocation walls rarely form during cyclic loading at low strain amplitudes of $\frac{\Delta\varepsilon_t}{2} = 0.3$ % as in Fig. 61(a), the microstructure mostly consists of planar slip bands as in Fig. 61(b) that show the dominant cyclic deformation mechanism in this condition is the planar slip of dislocations. By increasing the strain amplitudes to $\frac{\Delta\varepsilon_t}{2} = 0.7\%$, the more condensed dislocation cells and labyrinth structure in Fig. 61(c-d) indicate prominent wavy slip. Therefore, increasing $\frac{\Delta\varepsilon_t}{2}$ from 0.3% to 0.7% produces a change in the slip mode from planar to wavy.

Deformation twins were not detected in the CoCrFeNiMn alloy with an average grain size of ~15 μm even at a high strain amplitude of $\frac{\Delta\varepsilon_t}{2} = 0.85\%$ d ue to a stress level lower than the critical stress [265]. Increasing the grain size to ~66 μm or the strain amplitude to 1% led to the formation of deformation twins in grains with their <111> axes parallel to the loading direction [264,265,267,270]. Although, the small volume fraction of deformation twins at $\frac{\Delta\varepsilon_t}{2} \leq 0.7\%$ seems to have no significant effect on the overall LCF life [267], the twinning-dominated cyclic deformation was reported to have a positive effect on extending the fatigue life of the CoCrFeNiMn alloy with a grain size of ~184 μm at $\frac{\Delta\varepsilon_t}{2} = 1\%$ [270].

An interstitial carbon added to enhance the planarity of slip could improve the fatigue life of the CoCrFeNiMn alloy at $\frac{\Delta\varepsilon_t}{2} \leq 0.55\%$ [265]. However, this strategy was not applicable at $\frac{\Delta\varepsilon_t}{2} \geq 0.7\%$ where the formation of distinct dislocation cells shows the activation of wavy slip. Moreover, the coarse carbides that may form during the thermomechanical process can stimulate fatigue crack initiation and decrease the fatigue life [265]. In other research it was also claimed that the higher planarity of slip in a CoCrNi medium entropy alloy compared with the CoCrFeNiMn alloy could produce a superior LCF life at all studied ranges of $\frac{\Delta\varepsilon_t}{2}$ [266].

Decreasing the grain size either by conventional rolling and heat treatment to ~10 μm [265] or by ECAP to ≤ 1 μm [271] was beneficial at low $\frac{\Delta\varepsilon_t}{2}$ due to the impact on the strength. However, a microstructure with a coarser grain size exhibited a better fatigue life when the plastic part became more significant in cyclic loading. The other effect of decreasing the grain size is stimulating the fatigue crack initiation at annealing twin boundaries (TBs) rather than in slip bands (Fig. 62) [272]. Although the main fatigue-crack initiation sites are slip bands, the critical difference in Schmid factor between the matrix and the twinned area is decreased by reducing the grain size that produces more cracks at TBs [272].

The LCF behaviour of the CoCrFeNiMn alloy with a grain size of ~6.4 μm was also studied at 550 °C [268]. This microstructure was achieved by cold rolling and annealing at 800 °C for 1 h and it was a single phase before LCF. Although the cyclic stress response and microstructural evolutions were similar to those at RT [268], a high temperature produced a serrated plastic flow in the initial cycle hysteresis loops at 550 °C. It was proven that these serrations were due to cyclic load-stimulated precipitation of Cr-rich and NiMn-rich phases

near the grain boundaries. Since dynamic strain aging in SS316 reduced the fatigue life [273], these precipitates also appear to have a detrimental effect on the LCF life of the CoCrFeNiMn alloy. However, due to the simultaneous activation of oxidation at a high temperature and precipitation, more studies are now needed to clarify the exact effect of these precipitates on the fatigue life.

The LCF life of the CoCrFeNiMn alloy is compared with other HEAs in Fig. 63 and it is noted that different efforts were made recently to investigate the LCF behaviour of HEAs [265–268,270–272,274–277]. Although multiple deformation mechanisms are active in cyclic loading of $Al_{0.5}$CoCrFeNi [276] with a duplex *fcc-B2* microstructure, its durability was inferior to that of the HEAs with an initial single *fcc* phase. Increasing the planarity of slip by engineering the chemical composition from the CoCrFeNiMn to the CoCrNi alloy was the most effective way at low strain amplitudes [266]. It is noted also that the activation of a reversible *fcc* to *hcp* martensitic phase transformation at high strain amplitudes helps to maintain an improved planarity of slip in the *fcc* phase and this produces the best fatigue behaviour in the coarse-grained metastable HEAs (FeMnCoCr) [274,277,278]. Therefore, instructions for reaching a better LCF life can be developed by increasing the planarity of slip under different loading conditions.

9. Creep and superplasticity

9.1. *Creep*

For high temperature applications, the CoCrFeNiMn HEA shows superior oxidation and corrosion resistance and lower cost compared to their *bcc* refractory counterparts. Nevertheless, their inadequate strength tends to inhibit their direct utility for these specific applications. Understanding and predicting the creep behavior of HEAs is important for their use in industrial applications in high temperature services. Some investigators evaluated the high temperature properties of the CoCrFeNiMn HEA using different tests over a wide range of grain sizes and it is important to examine these results.

It is well known that the correlation of the steady-state creep rate $\dot{\varepsilon}$ in metallic materials with the applied stress σ can be described by a power-law equation of the form [279]:

$$\dot{\varepsilon} = \frac{AD_0Gb}{kT}\left(\frac{b}{d}\right)^p\left(\frac{\sigma}{G}\right)^n \exp\left(-\frac{Q}{RT}\right) \quad (12)$$

where A is a dimensionless material-dependent constant, G is the shear modulus, D_0 is the frequency factor, k is Boltzmann's constant, Q is the activation energy for creep deformation, and p and n are the inverse grain size and stress exponents, respectively. The values of n and Q are determined by plotting $\dot{\varepsilon}$ against σ on a double logarithmic scale and against $1/T$ at constant stress levels on a semi-logarithmic scale, respectively. It is important to note that the anticipated strain rate sensitivity, m, is equal to $1/n$.

Compression tests on a coarse-grained CoCrFeNiMn alloy with a grain size of ~420 μm at 750–1050 °C and in the strain rate range of 10^{-3} to 10 s^{-1} gave an n value of ~5 at low strain rates and power-law breakdown at high strain rates [30]. A fine-grained CoCrFeNiMn HEA with a grain size of ~25 μm led to $n \approx 5$–6 at 500–600 °C below 10^{-7} s^{-1} [280] and n close to ~3.7 at 750–900 °C [80] during creep tests.

The tensile creep behavior of the CoCrFeNiMn HEA was investigated over the temperature range of 500–600 °C under applied stresses of 140–400 MPa. The alloy exhibited two distinct regions with a stress-dependent transition from a low stress to a high stress region. This transition was observed under an applied stress of 350 MPa at 500 °C and it decreased to 200 MPa by increasing the temperature to 600 °C. The values of n and Q were reported as ~5–6 and ~268 kJ mol^{-1}, respectively, for the former region and ~8.9–14 and ~380 kJ mol^{-1}, respectively, for the latter region. It was suggested that stress-assisted dislocation climb controlled by lattice diffusion is the operative creep mechanism in the low stress region [280]. The activation energies for lattice diffusion of the constituent elements in the CoCrFeNiMn HEA are within the range of ~288–317 kJ mol^{-1} [74]. The high stress exponents and activation energy in the high stress region was related to the occurrence of dynamic recrystallization together with the formation of nano precipitates at grain boundaries during testing under higher stress. It was claimed that dislocation climb controlled by lattice diffusion is responsible for the deformation mechanism under higher stresses [280].

A stress exponent of ~3 was also reported in another fine-grained Cantor alloy with a grain size of ~12 μm. This alloy was processed by a thermomechanical treatment including cold rolling followed by an annealing treatment. Strain rate change tensile testing was used over the temperature range of 750–850 °C at low strain rates of 6.41×10^{-7}–6.41×10^{-6} s^{-1} [76]. It was proposed that solute drag creep [76,281,282] or dislocation climb creep [30,282] may operate as the rate-controlling deformation process in the fine and coarse grained CoCrFeNiMn HEA at elevated temperatures. Solute drag creep most likely governs the creep behaviour when $n = 3$.

It was suggested in another investigation that the creep mechanisms in the CoCrFeNiMn HEA are controlled by dislocation-lattice interactions due to the concentrated solid solution hardening and dislocation-dislocation interactions that arise from forest dislocation hardening. These mechanisms were confirmed by observing extensive lattice pinning and dislocation junctions in the microstructure [80]. The microstructure of the alloy after deformation at elevated temperatures and long-term creep at intermediate temperatures revealed a high density distribution of curved and entangled dislocations within the grain interiors with no evidence for any subgrain formation [78,80,283].

A systematic investigation was conducted by calculating and constructing deformation mechanism and processing maps for the CoCrFeNiMn HEA over a wide range of grain sizes at 600–1200 °C as illustrated in Fig. 64. It was proposed that in the typical strain rate range for hot working between 10^{-3} and 10 s^{-1} creep by dislocation climb is the dominant mechanism in the coarse-grained Cantor alloy with a grain size of ~100 μm. Grain boundary sliding appears at high temperatures and low strain rates in material with a grain size of ~10 μm and at a grain size of ~1 μm Coble creep and grain boundary sliding are the operative mechanisms. At lower strain rates of 10^{-4}

s^{-1}, which is within the range of typical creep strain rates, grain boundary sliding and Coble creep domains expand as the grain size decreases, and Coble creep is dominant over almost the entire temperature range when the grain size is ~1 μm. It is important to note that grain refinement due to dynamic recrystallization leads to an increase in the contribution of grain boundary sliding [284].

9.2. *Superplasticity*

Superplasticity refers to the exceptionally high strains that may be achieved in materials before failure during pulling in tension under a constant rate of straining and this is an important feature of materials that are used for industrial superplastic forming operations where complex curved shapes are fabricated for use in a range of applications [285]. Basically, two essential requirements for attaining superplasticity in bulk metals include a very small grain size of <10 μm and deformation at elevated temperatures of at least ~0.5T_m since superplastic flow is a diffusion-controlled process [286].

Thermomechanical treatment is a typical industrial method that is generally capable of reducing the grain size to ~2–5 μm. Nevertheless, the application of SPD was demonstrated to have a great potential for achieving ultrafine-grained materials and therefore providing superplasticity during plastic deformation [287] and this approach is now used extensively for achieving excellent superplastic forming capabilities [288].

There is a definitive criterion for the occurrence of superplastic flow in which the measured tensile elongation should be at least 400% with a strain rate sensitivity of $m \approx 0.5$ [289] and the main mechanism of this behaviour is the occurrence of grain boundary sliding [290]. A theoretical model based on grain boundary sliding accommodated by intragranular glide and climb leads to a superplastic strain rate, $\dot{\varepsilon}_{sp}$, which is given by a power-low relationship as represented in Eq. (12) where $D_{gb} = D_0 \exp(-Q/RT)$ is the coefficient for grain boundary

Table 12 – Summary of results for superplasticity and near-superplasticity in the Cantor alloy.

Minor element	Processing	T (°C)	Strain rate (s^{-1})	Elongation (%)	Ref.
–	Thermomechanical processing[a]	750	0.1	160	[295]
			0.001	280	
			0.0001	320	
	Thermomechanical processing[b]	1000	0.1	85	[284]
			0.05	89	
			0.01	84	
			0.005	85	
			0.001	70	
			0.0005	61	
	HPT	500	0.001	160	[296]
		600	0.1	340	
			0.01	400	
			0.001	510	
		700	0.1	425	
			0.01	500	
			0.001	610	
		800	0.1	320	
			0.01	370	
			0.001	400	
2 at.% Ti	HPT	600	0.01	460	[167]
		700	0.1	630	
			0.01	830	
			0.001	650	
		800	0.01	570	
9 at.% Al	Thermomechanical processing[c]	1000	0.1	108	[284]
			0.05	146	
			0.01	251	
			0.005	309	
			0.001	330	
			0.0005	290	
9 at.% Al	HPT	600	0.01	~400	[133]
		700	0.1	~1000	
			0.01	~1250	
		800	0.01	~1600	
			0.05	~2000	
			0.01	~1250	

[a] Cold rolling (reduction of thickness~50%), post deformation annealing at 800 °C for 1 h, warm rolling at 200 °C (reduction of thickness~85%) and finally annealing at 700 °C for 15 min to reach the average grain size of 1.4 μm.
[b] High-ratio differential speed rolling followed by annealing at 1000 °C for 1 h to reach the average grain size of 2.6 μm.
[c] High-ratio differential speed rolling followed by annealing at 1000 °C for 5 min to reach the average grain size of 16.3 μm.

diffusion, p and n are both equal to 2 and $A \approx 10$ [279]. This equation provides an excellent description of the superplastic flow of fine and ultrafine-grained materials [291–293] and it was shown that there is very good agreement between published data and the predictions of the equation with the above values for p and n for HEAs [294].

There is a report of an attempt to achieve superplasticity in the CoCrFeNiMn HEA where, after vacuum arc melting and homogenization, a fine-grained HEA with a grain size of ~1.4 μm was achieved by thermomechanical processing [295]. This thermomechanical processing included cold rolling with a reduction in thickness of ~50%, post-deformation annealing at 800 °C for 1 h, warm rolling at 200 °C with a reduction in thickness of ~85% and finally annealing at 700 °C for 15 min. The results showed that with increasing temperature until 750 °C the flow stress dropped significantly. Furthermore, it was not possible to reach a high ductility at a strain rate of 0.1 s^{-1} where the elongation was only ~150%. Additionally, it was shown that by decreasing the strain rate from 0.1 to 0.0001 s^{-1} the total elongation increased from ~150% to ~325% as shown in Fig. 65 [295]. It is important to note that these results do not meet the criterion of an elongation of at least 400% for true superplastic flow.

Nano-grained CoCrFeNiMn HEA with a grain size of <50 nm was processed by HPT and then subjected to tensile testing at 600–800 °C under strain rates of 10^{-3}–10^{-1} s^{-1}. The results revealed superplastic behavior at temperatures of 600 and 700 °C in which the maximum total elongation was 570% at 700 °C under a strain rate of 10^{-3} s^{-1} as shown in Fig. 66 with grain boundary sliding as the operating mechanism during deformation. This remarkable superplasticity is related to the presence of second phases of bcc and sigma Cr-rich precipitates which are effective for preventing grain growth by the Zener pinning mechanism [296]. The reported values for the stress exponent and the activation energy were ~3.3 so that $m \approx 0.3$ and ~113 kJ mol^{-1}, respectively. This value of m is not consistent with the predicated value where m corresponds to the inverse of the stress exponent and $n \approx 2$ so that the anticipated strain rate sensitivity is $m \approx 0.5$. Nevertheless, it is important to note that the m value of 0.3 suggests that deformation is controlled by an intragranular dislocation glide process [15] which is clearly not capable of achieving elongations up to 500%. It was suggested instead that this anomalously low strain rate sensitivity was attained due to the occurrence of significant grain growth during tensile testing where the grains in the CoCrFeNiMn alloy grew from <50 nm after HPT processing to ~1.0 μm after tensile testing at 700 °C [296].

As already noted, the second phase plays a very important role in grain growth because it can prevent the growth of grains by the Zener pinning method. Therefore, the second phase can improve the occurrence of superplasticity in the alloys. For improving the superplasticity, attempts were undertaken to improve the superplasticity of the Cantor HEA by adding 2 at.% Ti [167]. The results showed that nanocrystalline $CoCrFeNiMnTi_{0.1}$ HEA, processed by HPT, had a higher total elongation at 700 °C than a Ti-free Cantor HEA. The reason for this result is the higher volume fraction of the second phase at 700 °C which is ~12% compared with ~6% and the smaller grain size of ~0.6 μm compared with ~1 μm in the Ti-containing CoCrFeNiMn HEA [167]. This result highlights again the exceptional importance of minor additions of alloying elements in dictating the mechanical properties of HEAs.

As noted in section 6.1, the superplasticity of the Cantor HEA was improved by adding 9 at.% Al. Specifically, a dual-phase $Al_9(CoCrFeNiMn)_{91}$ HEA was developed where the microstructure included *fcc* grains and Ni- and Al-rich *B2* particles as shown in Fig. 67(a,b) and then a nanocrystalline $Al_9(CoCrFeNiMn)_{91}$ HEA was formed by the HPT technique [133]. The results showed that an extraordinary superplasticity of ~2000% was achieved in the $Al_9(CoCrFeNiMn)_{91}$ HEA at a high strain rate of 0.05 s^{-1} at 800 °C as in Fig. 67(c). It was concluded that the presence of the *B2* phase due to the presence of Al and the newly formed sigma phase during superplastic testing served to prevent grain growth and this was the reason for the superplasticity [133]. Table 12 summarizes the results now available for superplasticity in the Cantor alloy.

10. Summary and conclusions

1. The CoCrFeNiMn HEA alloy has a great potential for future industrial applications due to an excellent strain hardening capability, exceptional ductility at ambient and cryogenic temperatures and a promising fracture toughness at cryogenic temperatures. A relatively low yield stress at room temperature has led to many efforts to make modifications by microstructure engineering during thermomechanical treatments.
2. The thermomechanical processing, including cold working followed by annealing or deformation at a controlled elevated temperature, is a typical procedure to control the grain size and achieve fine-grained materials to improve the strength of the alloy. It was confirmed that the recrystallized microstructure after severe plastic deformation with a grain size of <1 μm revealed an excellent balance of strength and ductility in the alloy.
3. One of the most important ways to overcome the strength-ductility trade-off in the alloy is the use of post-deformation annealing at 600–800 °C where this can lead to remarkable mechanical properties. The resultant heterogeneous microstructures consist of a series of precipitates, recrystallized regions and deformed regions which promote the mechanical properties.
4. The strategy of adding minor amounts of a sixth interstitial, such as C, N, B and H or substitutional elements Al, Ti, Sn, Nb, Mo and V, was widely considered for improving the strength by solid solution or precipitation hardening mechanisms.
5. This alloy shows a much better fatigue limit than most other engineering alloys such as stainless steels, TWIP steels and pure titanium. Additionally, its fatigue-crack growth resistance outperforms that of austenitic stainless steels, Al and Mg alloys.
6. Dislocation-climb creep is the dominant mechanism in the coarse-grained alloy and with a grain size of ~1 μm. Coble creep and grain boundary sliding are also operative mechanisms. Grain boundary sliding appears at high temperatures and low strain rates in materials with grain

sizes of <10 μm and this facilitates superplasticity with elongation >600% for quandary alloys and senary alloys containing Ti or Al.

Declaration of Competing Interest

The authors declare that they have no known competing financial interests or personal relationships that could have appeared to influence the work reported in this paper.

Acknowledgements

This work was supported by the National Elites Foundation of the Islamic Republic of Iran and in part by the European Research Council under Grant Agreement No. 267464-SPDMETALS (HS and TGL).

REFERENCES

[1] Cantor B, Chang I, Knight P, Vincent A. Microstructural development in equiatomic multicomponent alloys. Mater Sci Eng, A 2004;375:213–8.
[2] Yeh JW, Chen SK, Lin SJ, Gan JY, Chin TS, Shun TT, et al. Nanostructured high-entropy alloys with multiple principal elements: novel alloy design concepts and outcomes. Adv Eng Mater 2004;6(5):299–303.
[3] Takeuchi A, Inoue A. Mixing enthalpy of liquid phase calculated by miedema's scheme and approximated with sub-regular solution model for assessing forming ability of amorphous and glassy alloys. Intermetallics 2010;18(9):1779–89.
[4] Sheng G, Liu CT. Phase stability in high entropy alloys: formation of solid-solution phase or amorphous phase. Prog Nat Sci: Mater Int 2011;21(6):433–46.
[5] Massalski TB. Comments concerning some features of phase diagrams and phase transformations. Mater Trans 2010;51(4):583–6.
[6] Yang X, Zhang Y. Prediction of high-entropy stabilized solid-solution in multi-component alloys. Mater Chem Phys 2012;132(2–3):233–8.
[7] Egami T, Waseda Y. Atomic size effect on the formability of metallic glasses. J Non-Cryst Solids 1984;64(1–2):113–34.
[8] Zhang Y, Zhou YJ, Lin JP, Chen GL, Liaw PK. Solid-solution phase formation rules for multi-component alloys. Adv Eng Mater 2008;10(6):534–8.
[9] Dong Y, Lu Y, Jiang L, Wang T, Li T. Effects of electro-negativity on the stability of topologically close-packed phase in high entropy alloys. Intermetallics 2014;52:105–9.
[10] Gali A, George EP. Tensile properties of high-and medium-entropy alloys. Intermetallics 2013;39:74–8.
[11] Otto F, Dlouhý A, Somsen C, Bei H, Eggeler G, George EP. The influences of temperature and microstructure on the tensile properties of a CoCrFeMnNi high-entropy alloy. Acta Mater 2013;61(15):5743–55.
[12] Gludovatz B, Hohenwarter A, Catoor D, Chang EH, George EP, Ritchie RO. A fracture-resistant high-entropy alloy for cryogenic applications. Science 2014;345(6201):1153–8.
[13] Otto F, Hanold NL, George EP. Microstructural evolution after thermomechanical processing in an equiatomic, single-phase CoCrFeMnNi high-entropy alloy with special focus on twin boundaries. Intermetallics 2014;54:39–48.
[14] Hadraba H, Chlup Z, Dlouhy A, Dobes F, Roupcova P, Vilemova M, et al. Oxide dispersion strengthened CoCrFeNiMn high-entropy alloy. Mater Sci Eng, A 2017;689:252–6.
[15] Laplanche G, Gadaud P, Horst O, Otto F, Eggeler G, George E. Temperature dependencies of the elastic moduli and thermal expansion coefficient of an equiatomic, single-phase CoCrFeMnNi high-entropy alloy. J Alloys Compd 2015;623:348–53.
[16] Laplanche G, Kostka A, Horst O, Eggeler G, George E. Microstructure evolution and critical stress for twinning in the CrMnFeCoNi high-entropy alloy. Acta Mater 2016;118:152–63.
[17] De Cooman BC, Estrin Y, Kim SK. Twinning-induced plasticity (TWIP) steels. Acta Mater 2018;142:283–362.
[18] Bhattacharjee P, Sathiaraj G, Zaid M, Gatti J, Lee C, Tsai C-W, et al. Microstructure and texture evolution during annealing of equiatomic CoCrFeMnNi high-entropy alloy. J Alloys Compd 2014;587:544–52.
[19] Suzuki H. Segregation of solute atoms to stacking faults. J Phys Soc Jpn 1962;17(2):322–5.
[20] Huang S, Li W, Lu S, Tian F, Shen J, Holmström E, et al. Temperature dependent stacking fault energy of FeCrCoNiMn high entropy alloy. Scripta Mater 2015;108:44–7.
[21] Stepanov N, Tikhonovsky M, Yurchenko N, Zyabkin D, Klimova M, Zherebtsov S, et al. Effect of cryo-deformation on structure and properties of CoCrFeNiMn high-entropy alloy. Intermetallics 2015;59:8–17.
[22] Joo S-H, Kato H, Jang M, Moon J, Tsai C, Yeh J, et al. Tensile deformation behavior and deformation twinning of an equimolar CoCrFeMnNi high-entropy alloy. Mater Sci Eng, A 2017;689:122–33.
[23] Sun S, Tian Y, Lin H, Yang H, Dong X, Wang Y, et al. Transition of twinning behavior in CoCrFeMnNi high entropy alloy with grain refinement. Mater Sci Eng, A 2018;712:603–7.
[24] Cheng Q, Xu X, Li X, Li Y, Nieh T, Chen M. Solid solution softening in a Al0. 1CoCrFeMnNi high-entropy alloy. Scripta Mater 2020;186:63–8.
[25] Ma X, Chen J, Wang X, Xu Y, Xue Y. Microstructure and mechanical properties of cold drawing CoCrFeMnNi high entropy alloy. J Alloys Compd 2019;795:45–53.
[26] Laplanche G, Horst O, Otto F, Eggeler G, George E. Microstructural evolution of a CoCrFeMnNi high-entropy alloy after swaging and annealing. J Alloys Compd 2015;647:548–57.
[27] Mehranpour MS, Shahmir H, Asghari-Rad P, Hosseinzadeh M, Rasooli N, Kim HS, et al. Upgrading of superior strength–ductility trade-off of CoCrFeNiMn high-entropy alloy by microstructural engineering. Materialia 2022;22:101394.
[28] Otto F, Yang Y, Bei H, George EP. Relative effects of enthalpy and entropy on the phase stability of equiatomic high-entropy alloys. Acta Mater 2013;61(7):2628–38.
[29] Jang MJ, Joo S-H, Tsai C-W, Yeh J-W, Kim HS. Compressive deformation behavior of CrMnFeCoNi high-entropy alloy. Met Mater Int 2016;22(6):982–6.
[30] Jeong H, Park H, Park K, Na T, Kim W. High-temperature deformation mechanisms and processing maps of equiatomic CoCrFeMnNi high-entropy alloy. Mater Sci Eng, A 2019;756:528–37.
[31] Schuh B, Mendez-Martin F, Völker B, George EP, Clemens H, Pippan R, et al. Mechanical properties, microstructure and thermal stability of a nanocrystalline CoCrFeMnNi high-

entropy alloy after severe plastic deformation. Acta Mater 2015;96:258–68.
[32] Shahmir H, He J, Lu Z, Kawasaki M, Langdon TG. Effect of annealing on mechanical properties of a nanocrystalline CoCrFeNiMn high-entropy alloy processed by high-pressure torsion. Mater Sci Eng, A 2016;676:294–303.
[33] Shahmir H, Mousavi T, He J, Lu Z, Kawasaki M, Langdon TG. Microstructure and properties of a CoCrFeNiMn high-entropy alloy processed by equal-channel angular pressing. Mater Sci Eng, A 2017;705:411–9.
[34] Mehranpour MS, Shahmir H, Nili-Ahmadabadi M. Microstructure and excess free volume of severely cold shape rolled CoCrFeNiMn high entropy alloy. J Alloys Compd 2020;840:155672.
[35] Valiev R. Nanomaterial advantage. Nature 2002;419(6910):887–9.
[36] Valiev R. Nanostructuring of metals by severe plastic deformation for advanced properties. Nat Mater 2004;3(8):511.
[37] Valiev RZ, Straumal B, Langdon TG. Using severe plastic deformation to produce nanostructured materials with superior properties. Annu Rev Mater Res 2022;52:14.1–14.26.
[38] Valiev RZ, Islamgaliev RK, Alexandrov IV. Bulk nanostructured materials from severe plastic deformation. Prog Mater Sci 2000;45(2):103–89.
[39] Valiev R, Sergueeva A, Mukherjee A. The effect of annealing on tensile deformation behavior of nanostructured SPD titanium. Scripta Mater 2003;49(7):669–74.
[40] Shahmir H, Asghari-Rad P, Mehranpour MS, Forghani F, Kim HS, Nili-Ahmadabadi M. Evidence of FCC to HCP and BCC-martensitic transformations in a CoCrFeNiMn high-entropy alloy by severe plastic deformation. Mater Sci Eng, A 2021;807:140875.
[41] Huang C, Gao Y, Yang G, Wu S, Li G, Li S. Bulk nanocrystalline stainless steel fabricated by equal channel angular pressing. J Mater Res 2006;21(7):1687–92.
[42] Zhilyaev AP, Langdon TG. Using high-pressure torsion for metal processing: fundamentals and applications. Prog Mater Sci 2008;53(6):893–979.
[43] Valiev RZ, Langdon TG. Principles of equal-channel angular pressing as a processing tool for grain refinement. Prog Mater Sci 2006;51(7):881–981.
[44] Koch C. Optimization of strength and ductility in nanocrystalline and ultrafine grained metals. Scripta Mater 2003;49(7):657–62.
[45] Christian JW, Mahajan S. Deformation twinning. Prog Mater Sci 1995;39(1–2):1–157.
[46] Salishchev G, Mironov S, Zherebtsov S, Belyakov A. Changes in misorientations of grain boundaries in titanium during deformation. Mater Char 2010;61(7):732–9.
[47] Zherebtsov S, Dyakonov G, Salem A, Sokolenko V, Salishchev G, Semiatin S. Formation of nanostructures in commercial-purity titanium via cryorolling. Acta Mater 2013;61(4):1167–78.
[48] Lu K, Lu L, Suresh S. Strengthening materials by engineering coherent internal boundaries at the nanoscale. Science 2009;324(5925):349–52.
[49] Valiev RZ, Langdon TG. Achieving exceptional grain refinement through severe plastic deformation: new approaches for improving the processing technology. Metall Mater Trans 2011;42(10):2942–51.
[50] Langdon TG. Twenty-five years of ultrafine-grained materials: achieving exceptional properties through grain refinement. Acta Mater 2013;61(19):7035–59.
[51] Steyskal E-M, Oberdorfer B, Sprengel W, Zehetbauer M, Pippan R, Würschum R. Direct experimental determination of grain boundary excess volume in metals. Phys Rev Lett 2012;108(5):055504.
[52] Mehranpour MS, Shahmir H, Nili-Ahmadabadi M. CoCrFeNiMn high entropy alloy microstructure and mechanical properties after severe cold shape rolling and annealing. Mater Sci Eng, A 2020;793:139884.
[53] Lapovok R, Tomus D, Mang J, Estrin Y, Lowe TC. Evolution of nanoscale porosity during equal-channel angular pressing of titanium. Acta Mater 2009;57(10):2909–18.
[54] Divinski SV, Padmanabhan K, Wilde G. Microstructure evolution during severe plastic deformation. Phil Mag 2011;91(36):4574–93.
[55] Li Z, Fu L, Zheng H, Yu R, Lv L, Sun Y, et al. Effect of annealing temperature on microstructure and mechanical properties of a severe cold-rolled FeCoCrNiMn high-entropy alloy. Metall Mater Trans 2019;50(7):3223–37.
[56] Huang S, Li W, Li X, Schönecker S, Bergqvist L, Holmström E, et al. Mechanism of magnetic transition in FeCrCoNi-based high entropy alloys. Mater Des 2016;103:71–4.
[57] Tracy CL, Park S, Rittman DR, Zinkle SJ, Bei H, Lang M, et al. High pressure synthesis of a hexagonal close-packed phase of the high-entropy alloy CrMnFeCoNi. Nat Commun 2017;8(1):1–6.
[58] Yu P, Zhang L, Tang H, Fan J, Liaw PK, Li G, et al. Formation, reverse transformation, and properties of ε-martensite phase in the CoCrFeMnNi high-entropy alloy under high-pressure. J Alloys Compd 2019;779:1–6.
[59] Furukawa M, Iwahashi Y, Horita Z, Nemoto M, Langdon TG. The shearing characteristics associated with equal-channel angular pressing. Mater Sci Eng, A 1998;257(2):328–32.
[60] Qu S, An X, Yang H, Huang C, Yang G, Zang Q, et al. Microstructural evolution and mechanical properties of Cu–Al alloys subjected to equal channel angular pressing. Acta Mater 2009;57(5):1586–601.
[61] Li Y, Tao N, Lu K. Microstructural evolution and nanostructure formation in copper during dynamic plastic deformation at cryogenic temperatures. Acta Mater 2008;56(2):230–41.
[62] Zaddach A, Niu C, Koch C, Irving D. Mechanical properties and stacking fault energies of NiFeCrCoMn high-entropy alloy. JOM 2013;65(12):1780–9.
[63] Moon J, Qi Y, Tabachnikova E, Estrin Y, Choi W-M, Joo S-H, et al. Deformation-induced phase transformation of Co20Cr26Fe20Mn20Ni14 high-entropy alloy during high-pressure torsion at 77 K. Mater Lett 2017;202:86–8.
[64] Podolskiy AV, Shapovalov YO, Tabachnikova ED, Tortika AS, Tikhonovsky MA, Joni B, et al. Anomalous evolution of strength and microstructure of high-entropy alloy CoCrFeNiMn after high-pressure torsion at 300 and 77 K. Adv Eng Mater 2020;22(1):1900752.
[65] Skrotzki W, Pukenas A, Odor E, Joni B, Ungar T, Völker B, et al. Microstructure, texture, and strength development during high-pressure torsion of CrMnFeCoNi high-entropy alloy. Crystals 2020;10(4):336.
[66] Picak S, Yilmaz H, Karaman I. Simultaneous deformation twinning and martensitic transformation in CoCrFeMnNi high entropy alloy at high temperatures. Scripta Mater 2021;202:113995.
[67] Zhao S, Li Z, Zhu C, Yang W, Zhang Z, Armstrong DE, et al. Amorphization in extreme deformation of the CrMnFeCoNi high-entropy alloy. Sci Adv 2021;7(5):eabb3108.
[68] Fujita H, Ueda S. Stacking faults and fcc (γ)→ hcp (ε) transformation in 188-type stainless steel. Acta Metall 1972;20(5):759–67.
[69] Fujita H, Mori T. A formation mechanism of mechanical twins in FCC Metals. Scripta Metall 1975;9(6):631–6.
[70] Picak S, Liu J, Hayrettin C, Nasim W, Canadinc D, Xie K, et al. Anomalous work hardening behavior of Fe40Mn40Cr10Co10 high entropy alloy single crystals deformed by twinning and slip. Acta Mater 2019;181:555–69.

[71] Yapici G, Karaman I, Luo Z, Maier H, Chumlyakov Y. Microstructural refinement and deformation twinning during severe plastic deformation of 316L stainless steel at high temperatures. J Mater Res 2004;19(8):2268–78.
[72] Humphreys FJ, Hatherly M. Recrystallization and related annealing phenomena. Elsevier; 2012.
[73] Stepanov N, Shaysultanov D, Yurchenko NY, Zherebtsov S, Ladygin A, Salishchev G, et al. High temperature deformation behavior and dynamic recrystallization in CoCrFeNiMn high entropy alloy. Mater Sci Eng, A 2015;636:188–95.
[74] Tsai K-Y, Tsai M-H, Yeh J-W. Sluggish diffusion in Co–Cr–Fe–Mn–Ni high-entropy alloys. Acta Mater 2013;61(13):4887–97.
[75] Liu W, Wu Y, He J, Nieh T, Lu Z. Grain growth and the Hall–Petch relationship in a high-entropy FeCrNiCoMn alloy. Scripta Mater 2013;68(7):526–9.
[76] He J, Zhu C, Zhou D, Liu W, Nieh T, Lu Z. Steady state flow of the FeCoNiCrMn high entropy alloy at elevated temperatures. Intermetallics 2014;55:9–14.
[77] Eleti RR, Bhattacharjee T, Zhao L, Bhattacharjee PP, Tsuji N. Hot deformation behavior of CoCrFeMnNi FCC high entropy alloy. Mater Chem Phys 2018;210:176–86.
[78] Zhang M, George E, Gibeling J. Elevated-temperature deformation mechanisms in a CrMnFeCoNi high-entropy alloy. Acta Mater 2021;218:117181.
[79] Laplanche G, Bonneville J, Varvenne C, Curtin W, George EP. Thermal activation parameters of plastic flow reveal deformation mechanisms in the CrMnFeCoNi high-entropy alloy. Acta Mater 2018;143:257–64.
[80] Zhang M, George E, Gibeling J. Tensile creep properties of a CrMnFeCoNi high-entropy alloy. Scripta Mater 2021;194:113633.
[81] Sun S, Tian Y, Lin H, Dong X, Wang Y, Zhang Z, et al. Enhanced strength and ductility of bulk CoCrFeMnNi high entropy alloy having fully recrystallized ultrafine-grained structure. Mater Des 2017;133:122–7.
[82] Sun S, Tian Y, Lin H, Dong X, Wang Y, Wang Z, et al. Temperature dependence of the Hall–Petch relationship in CoCrFeMnNi high-entropy alloy. J Alloys Compd 2019;806:992–8.
[83] Shahmir H, Mehranpour MS, Shams S, Lee CS, Langdon TG. Grain size tailoring to control strain hardening and improve the mechanical properties of a CoCrFeNiMn high-entropy alloy. High Entropy Alloys & Materials 2022:1–12.
[84] Sohrabi MJ, Mirzadeh H, Dehghanian C. Significance of martensite reversion and austenite stability to the mechanical properties and transformation-induced plasticity effect of austenitic stainless steels. J Mater Eng Perform 2020;5.
[85] Klimova M, Shaysultanov D, Zherebtsov S, Stepanov N. Effect of second phase particles on mechanical properties and grain growth in a CoCrFeMnNi high entropy alloy. Mater Sci Eng, A 2019;748:228–35.
[86] Gu J, Ni S, Liu Y, Song M. Regulating the strength and ductility of a cold rolled FeCrCoMnNi high-entropy alloy via annealing treatment. Mater Sci Eng, A 2019;755:289–94.
[87] Stepanov N, Shaysultanov D, Ozerov M, Zherebtsov S, Salishchev G. Second phase formation in the CoCrFeNiMn high entropy alloy after recrystallization annealing. Mater Lett 2016;185:1–4.
[88] Zhang Y, Zuo TT, Tang Z, Gao MC, Dahmen KA, Liaw PK, et al. Microstructures and properties of high-entropy alloys. Prog Mater Sci 2014;61:1–93.
[89] Won JW, Lee S, Park SH, Kang M, Lim KR, Park CH, et al. Ultrafine-grained CoCrFeMnNi high-entropy alloy produced by cryogenic multi-pass caliber rolling. J Alloys Compd 2018;742:290–5.
[90] Singh A, Basha D, Matsushita Y, Tsuchiya K, Lu Z, Nieh T-G, et al. Domain structure and lattice effects in a severely plastically deformed CoCrFeMnNi high entropy alloy. J Alloys Compd 2020;812:152028.
[91] Han Z, Liang S, Yang J, Wei R, Zhang C. A superior combination of strength-ductility in CoCrFeNiMn high-entropy alloy induced by asymmetric rolling and subsequent annealing treatment. Mater Char 2018;145:619–26.
[92] Podolskiy A, Schafler E, Tabachnikova E, Tikhonovsky M, Zehetbauer M. Thermally activated deformation of nanocrystalline and coarse grained CoCrFeNiMn high entropy alloy in the temperature range 4.2–350 K. Low Temp Phys 2018;44(9):976–82.
[93] Kwon YJ, Won JW, Park SH, Lee JH, Lim KR, Na YS, et al. Ultrahigh-strength CoCrFeMnNi high-entropy alloy wire rod with excellent resistance to hydrogen embrittlement. Mater Sci Eng, A 2018;732:105–11.
[94] Zhou W, Fu L, Liu P, Xu X, Chen B, Zhu G, et al. Deformation stimulated precipitation of a single-phase CoCrFeMnNi high entropy alloy. Intermetallics 2017;85:90–7.
[95] Otto F, Dlouhý A, Pradeep KG, Kuběnová M, Raabe D, Eggeler G, et al. Decomposition of the single-phase high-entropy alloy CrMnFeCoNi after prolonged anneals at intermediate temperatures. Acta Mater 2016;112:40–52.
[96] Stepanov N, Shaysultanov D, Salishchev G, Tikhonovsky M, Oleynik E, Tortika A, et al. Effect of V content on microstructure and mechanical properties of the CoCrFeMnNiVx high entropy alloys. J Alloys Compd 2015;628:170–85.
[97] Pickering E, Muñoz-Moreno R, Stone HJ, Jones NG. Precipitation in the equiatomic high-entropy alloy CrMnFeCoNi. Scripta Mater 2016;113:106–9.
[98] Kim Y-K, Ham G-S, Kim HS, Lee K-A. High-cycle fatigue and tensile deformation behaviors of coarse-grained equiatomic CoCrFeMnNi high entropy alloy and unexpected hardening behavior during cyclic loading. Intermetallics 2019;111:106486.
[99] Li Z, Fu L, Peng J, Zheng H, Shan A. Effect of annealing on microstructure and mechanical properties of an ultrafine-structured Al-containing FeCoCrNiMn high-entropy alloy produced by severe cold rolling. Mater Sci Eng, A 2020;786:139446.
[100] Ondicho I, Choi M, Choi W-M, Jeon JB, Jafarian HR, Lee B-J, et al. Experimental investigation and phase diagram of CoCrMnNi–Fe system bridging high-entropy alloys and high-alloyed steels. J Alloys Compd 2019;785:320–7.
[101] Li L, Li Z. Aging induced segregation and nanoprecipitation in a severely deformed equiatomic high-entropy alloy. Mater Char 2020;165:110369.
[102] Chou T, Huang J, Yang C, Lin S, Nieh T. Consideration of kinetics on intermetallics formation in solid-solution high entropy alloys. Acta Mater 2020;195.
[103] Zhang Y, Gao M, Yeh J, Liaw P, Zhang Y. High-Entropy alloys: fundamentals and applications. 2016.
[104] Mehranpour MS, Shahmir H, Nili-Ahmadabadi M. Precipitation kinetics in heavily deformed CoCrFeNiMn high entropy alloy. Mater Lett 2021;288:129359.
[105] Tsai C-W, Chen Y-L, Tsai M-H, Yeh J-W, Shun T-T, Chen S-K. Deformation and annealing behaviors of high-entropy alloy Al0. 5CoCrCuFeNi. J Alloys Compd 2009;486(1–2):427–35.
[106] Hsu C-Y, Juan C-C, Wang W-R, Sheu T-S, Yeh J-W, Chen S-K. On the superior hot hardness and softening resistance of AlCoCrxFeMo0. 5Ni high-entropy alloys. Mater Sci Eng, A 2011;528(10–11):3581–8.
[107] Senkov ON, Wilks G, Scott J, Miracle DB. Mechanical properties of Nb25Mo25Ta25W25 and

V20Nb20Mo20Ta20W20 refractory high entropy alloys. Intermetallics 2011;19(5):698–706.
[108] Tsai M-H, Wang C-W, Tsai C-W, Shen W-J, Yeh J-W, Gan J-Y, et al. Thermal stability and performance of NbSiTaTiZr high-entropy alloy barrier for copper metallization. J Electrochem Soc 2011;158(11):H1161.
[109] Tsai M-H, Yeh J-W, Gan J-Y. Diffusion barrier properties of AlMoNbSiTaTiVZr high-entropy alloy layer between copper and silicon. Thin Solid Films 2008;516(16):5527–30.
[110] Shun T-T, Hung C-H, Lee C-F. Formation of ordered/disordered nanoparticles in FCC high entropy alloys. J Alloys Compd 2010;493(1–2):105–9.
[111] Juan C-C, Hsu C-Y, Tsai C-W, Wang W-R, Sheu T-S, Yeh J-W, et al. On microstructure and mechanical performance of AlCoCrFeMo0. 5Nix high-entropy alloys. Intermetallics 2013;32:401–7.
[112] Tong C-J, Chen Y-L, Yeh J-W, Lin S-J, Chen S-K, Shun T-T, et al. Microstructure characterization of Al x CoCrCuFeNi high-entropy alloy system with multiprincipal elements. Metall Mater Trans 2005;36(4):881–93.
[113] Laurent-Brocq M, Akhatova A, Perrière L, Chebini S, Sauvage X, Leroy E, et al. Insights into the phase diagram of the CrMnFeCoNi high entropy alloy. Acta Mater 2015;88:355–65.
[114] Ma L, Li C, Jiang Y, Zhou J, Wang L, Wang F, et al. Cooling rate-dependent microstructure and mechanical properties of AlxSi0. 2CrFeCoNiCu1− x high entropy alloys. J Alloys Compd 2017;694:61–7.
[115] Lewis M. Precipitation of (Fe, Cr) sigma phase from austenite. Acta Metall 1966;14(11):1421–8.
[116] Daniel R, Zalesak J, Matko I, Baumegger W, Hohenwarter A, George EP, et al. Microstructure-dependent phase stability and precipitation kinetics in equiatomic CrMnFeCoNi high-entropy alloy: role of grain boundaries. Acta Mater 2022;223:117470.
[117] Laplanche G, Berglund S, Reinhart C, Kostka A, Fox F, George E. Phase stability and kinetics of σ-phase precipitation in CrMnFeCoNi high-entropy alloys. Acta Mater 2018;161:338–51.
[118] Lee KH, Hong S-K, Hong SI. Precipitation and decomposition in CoCrFeMnNi high entropy alloy at intermediate temperatures under creep conditions. Materialia 2019;8:100445.
[119] Cahn JW. The kinetics of grain boundary nucleated reactions. Acta Metall 1956;4(5):449–59.
[120] Lee U, Straumal B, Park N. Dynamic precipitation of σ-phase and element partitioning in equiatomic CoCrFeMnNi high-entropy alloy. Mater Sci Eng, A 2021;804:140739.
[121] Sohrabi M, Mirzadeh H, Mehranpour M, Heydarinia A, Razi R. Aging kinetics and mechanical properties of copper-bearing low-carbon HSLA-100 microalloyed steel. Arch Civ Mech Eng 2019;19(4):1409–18.
[122] The theory of transformations in metals and alloys, 1st Edition - December 10, 2002.
[123] Vaidya M, Pradeep K, Murty B, Wilde G, Divinski S. Radioactive isotopes reveal a non sluggish kinetics of grain boundary diffusion in high entropy alloys. Sci Rep 2017;7(1):1–11.
[124] Monroe FC. Effects of phase decomposition on the strength of CoCrFeMnNi high entropy alloy. Clemson University; 2020.
[125] LaRosa CR, Shih M, Varvenne C, Ghazisaeidi M. Solid solution strengthening theories of high-entropy alloys. Mater Char 2019;151:310–7.
[126] Okamoto NL, Yuge K, Tanaka K, Inui H, George EP. Atomic displacement in the CrMnFeCoNi high-entropy alloy–A scaling factor to predict solid solution strengthening. AIP Adv 2016;6(12):125008.
[127] Roy A, Sreeramagiri P, Babuska T, Krick B, Ray PK, Balasubramanian G. Lattice distortion as an estimator of solid solution strengthening in high-entropy alloys. Mater Char 2021;172:110877.
[128] He J, Wang H, Huang H, Xu X, Chen M, Wu Y, et al. A precipitation-hardened high-entropy alloy with outstanding tensile properties. Acta Mater 2016;102:187–96.
[129] Shahmir H, Nili-Ahmadabadi M, Shafiee A, Andrzejczuk M, Lewandowska M, Langdon TG. Effect of Ti on phase stability and strengthening mechanisms of a nanocrystalline CoCrFeMnNi high-entropy alloy. Mater Sci Eng, A 2018;725:196–206.
[130] Klimova M, Shaysultanov D, Semenyuk A, Zherebtsov S, Salishchev G, Stepanov N. Effect of nitrogen on mechanical properties of CoCrFeMnNi high entropy alloy at room and cryogenic temperatures. J Alloys Compd 2020;849:156633.
[131] He J, Liu W, Wang H, Wu Y, Liu X, Nieh T, et al. Effects of Al addition on structural evolution and tensile properties of the FeCoNiCrMn high-entropy alloy system. Acta Mater 2014;62:105–13.
[132] Shahmir H, Nili-Ahmadabadi M, Shafie A, Langdon TG. Hardening and thermal stability of a nanocrystalline CoCrFeNiMnTi0. 1 high-entropy alloy processed by high-pressure torsion. In: IOP conference series: materials science and engineering. IOP Publishing; 2017, 012017.
[133] Nguyen NT-C, Asghari-Rad P, Sathiyamoorthi P, Zargaran A, Lee CS, Kim HS. Ultrahigh high-strain-rate superplasticity in a nanostructured high-entropy alloy. Nat Commun 2020;11(1):1–7.
[134] Qin G, Li Z, Chen R, Zheng H, Fan C, Wang L, et al. CoCrFeMnNi high-entropy alloys reinforced with Laves phase by adding Nb and Ti elements. J Mater Res 2019;34(6):1011–20.
[135] Park JM, Moon J, Bae JW, Jung J, Lee S, Kim HS. Effect of annealing heat treatment on microstructural evolution and tensile behavior of Al0. 5CoCrFeMnNi high-entropy alloy. Mater Sci Eng, A 2018;728:251–8.
[136] Hachet D, Gorsse S, Godet S. Microstructure study of cold rolled Al0. 32CoCrFeMnNi high-entropy alloy: interactions between recrystallization and precipitation. Mater Sci Eng, A 2021;802:140452.
[137] Kang J, Park N, Kim J-K, Park JH. Role of recrystallization and second phases on mechanical properties of (CoCrFeMnNi) 95.2 Al3. 2Ti1. 6 high entropy alloy. Mater Sci Eng, A 2021;814:141249.
[138] Shahmir H, Derakhshandeh A, Hallstedt B, Nili-Ahmadabadi M. Microstructural evolution and mechanical properties of CoCrFeNiMnTix high-entropy alloys. Mater Werkst 2021;52(4):441–51.
[139] Shahmir H, Mehranpour MS, Derakhshandeh A, Nili-Ahmadabadi M. Microstructure tailoring to enhance mechanical properties in CoCrFeNiMn high-entropy alloy by Ti addition and thermomechanical treatment. Mater Char 2021;182:111513.
[140] Yamanaka S, Ikeda K-I, Miura S. The effect of titanium and silicon addition on phase equilibrium and mechanical properties of CoCrFeMnNi-based high entropy alloy. J Mater Res 2021;36(10):2056–70.
[141] Yao X, Wei J, Li T. Effects of Mo element on microstructure and mechanical properties of CoCrFeMnNi high entropy alloys. In: IOP conference series: materials science and engineering. IOP Publishing; 2019, 012019.
[142] Wang C, Li T-H, Liao Y-C, Li C-L, Jang JS-C, Hsueh C-H. Hardness and strength enhancements of CoCrFeMnNi high-entropy alloy with Nd doping. Mater Sci Eng, A 2019;764:138192.

[143] Gu X, Dong Y, Zhuang Y, Wang J. Microstructure and mechanical properties of CoCrFeMnNiSn x high-entropy alloys. Met Mater Int 2020;26(3):292–301.
[144] Seol JB, Bae JW, Li Z, Han JC, Kim JG, Raabe D, et al. Boron doped ultrastrong and ductile high-entropy alloys. Acta Mater 2018;151:366–76.
[145] Xiong F, Fu R, Li Y, Xu B, Qi X. Influences of nitrogen alloying on microstructural evolution and tensile properties of CoCrFeMnNi high-entropy alloy treated by cold-rolling and subsequent annealing. Mater Sci Eng, A 2020;787:139472.
[146] Xiong F, Fu R-D, Li Y-J, Sang D-l. Effects of nitrogen alloying and friction stir processing on the microstructures and mechanical properties of CoCrFeMnNi high-entropy alloys. J Alloys Compd 2020;822:153512.
[147] Astafurova E, Panchenko MY, Reunova K, Mikhno A, Moskvina V, Melnikov E, et al. The effect of nitrogen alloying on hydrogen-assisted plastic deformation and fracture in FeMnNiCoCr high-entropy alloys. Scripta Mater 2021;194:113642.
[148] Chen J, Yao Z, Wang X, Lu Y, Wang X, Liu Y, et al. Effect of C content on microstructure and tensile properties of as-cast CoCrFeMnNi high entropy alloy. Mater Chem Phys 2018;210:136–45.
[149] Astafurova E, Reunova K, Melnikov E, Panchenko MY, Astafurov S, Maier G, et al. On the difference in carbon-and nitrogen-alloying of equiatomic FeMnCrNiCo high-entropy alloy. Mater Lett 2020;276:128183.
[150] Guo L, Ou X, Ni S, Liu Y, Song M. Effects of carbon on the microstructures and mechanical properties of FeCoCrNiMn high entropy alloys. Mater Sci Eng, A 2019;746:356–62.
[151] Li Z. Interstitial equiatomic CoCrFeMnNi high-entropy alloys: carbon content, microstructure, and compositional homogeneity effects on deformation behavior. Acta Mater 2019;164:400–12.
[152] Peng J, Li Z, Fu L, Ji X, Pang Z, Shan A. Carbide precipitation strengthening in fine-grained carbon-doped FeCoCrNiMn high entropy alloy. J Alloys Compd 2019;803:491–8.
[153] Ko JY, Hong SI. Microstructural evolution and mechanical performance of carbon-containing CoCrFeMnNi-C high entropy alloys. J Alloys Compd 2018;743:115–25.
[154] Wu Z, Parish C, Bei H. Nano-twin mediated plasticity in carbon-containing FeNiCoCrMn high entropy alloys. J Alloys Compd 2015;647:815–22.
[155] Cheng H, Wang H, Xie Y, Tang Q, Dai P. Controllable fabrication of a carbide-containing FeCoCrNiMn high-entropy alloy: microstructure and mechanical properties. Mater Sci Technol 2017;33(17):2032–9.
[156] Guo L, Gu J, Gong X, Li K, Ni S, Liu Y, et al. Short-range ordering induced serrated flow in a carbon contained FeCoCrNiMn high entropy alloy. Micron 2019;126:102739.
[157] Zhao Y, Lee D-H, Seok M-Y, Lee J-A, Phaniraj M, Suh J-Y, et al. Resistance of CoCrFeMnNi high-entropy alloy to gaseous hydrogen embrittlement. Scripta Mater 2017;135:54–8.
[158] Koyama M, Ichii K, Tsuzaki K. Grain refinement effect on hydrogen embrittlement resistance of an equiatomic CoCrFeMnNi high-entropy alloy. Int J Hydrogen Energy 2019;44(31):17163–7.
[159] Luo H, Li Z, Raabe D. Hydrogen enhances strength and ductility of an equiatomic high-entropy alloy. Sci Rep 2017;7(1):1–7.
[160] Pu Z, Chen Y, Dai L. Strong resistance to hydrogen embrittlement of high-entropy alloy. Mater Sci Eng, A 2018;736:156–66.
[161] Li J, Gao B, Wang Y, Chen X, Xin Y, Tang S, et al. Microstructures and mechanical properties of nano carbides reinforced CoCrFeMnNi high entropy alloys. J Alloys Compd 2019;792:170–9.
[162] Tian Y, Sun S, Lin H, Zhang Z. Fatigue behavior of CoCrFeMnNi high-entropy alloy under fully reversed cyclic deformation. J Mater Sci Technol 2019;35(3):334–40.
[163] Kumar J, Kumar N, Das S, Gurao N, Biswas K. Effect of Al addition on the microstructural evolution of equiatomic CoCrFeMnNi alloy. Trans Indian Inst Met 2018;71(11):2749–58.
[164] Moon J, Bae JW, Jang MJ, Baek SM, Yim D, Lee B-J, et al. Effects of homogenization temperature on cracking during cold-rolling of Al0. 5CoCrFeMnNi high-entropy alloy. Mater Chem Phys 2018;210:187–91.
[165] Sun X, Zhang H, Li W, Ding X, Wang Y, Vitos L. Generalized stacking fault energy of Al-doped CrMnFeCoNi high-entropy alloy. Nanomaterials 2020;10(1):59.
[166] Lin L, Xian X, Zhong Z, Chen C, Zhu Z, Wu Y, et al. A multi-phase CrMnFeCoNiAl0. 75 high-entropy alloy with high strength at intermediate temperature. Intermetallics 2020;120:106744.
[167] Shahmir H, Nili-Ahmadabadi M, Shafiee A, Langdon TG. Effect of a minor titanium addition on the superplastic properties of a CoCrFeNiMn high-entropy alloy processed by high-pressure torsion. Mater Sci Eng, A 2018;718:468–76.
[168] Mehranpour MS, Shahmir H, Derakhshandeh A, Nili-Ahmadabadi M. Significance of Ti addition on precipitation in CoCrFeNiMn high-entropy alloy. J Alloys Compd 2021;888:161530.
[169] Liu K, Nene S, Frank M, Sinha S, Mishra R. Metastability-assisted fatigue behavior in a friction stir processed dual-phase high entropy alloy. Mater Res Lett 2018;6(11):613–9.
[170] Qin G, Chen R, Zheng H, Fang H, Wang L, Su Y, et al. Strengthening FCC-CoCrFeMnNi high entropy alloys by Mo addition. J Mater Sci Technol 2019;35(4):578–83.
[171] Simmons J. Overview: high-nitrogen alloying of stainless steels. Mater Sci Eng, A 1996;207(2):159–69.
[172] He M, Shen Y, Jia N, Liaw P. C and N doping in high-entropy alloys: a pathway to achieve desired strength-ductility synergy. Appl Mater Today 2021;25:101162.
[173] Wu R, Freeman AJ, Olson GB. First principles determination of the effects of phosphorus and boron on iron grain boundary cohesion. Science 1994;265(5170):376–80.
[174] Raabe D, Herbig M, Sandlöbes S, Li Y, Tytko D, Kuzmina M, et al. Grain boundary segregation engineering in metallic alloys: a pathway to the design of interfaces. Curr Opin Solid State Mater Sci 2014;18(4):253–61.
[175] Park J, Lee Y, Nb (C. N) precipitation kinetics in the bainite region of a low-carbon Nb-microalloyed steel. Scripta Mater 2007;57(2):109–12.
[176] Scott C, Remy B, Collet J-L, Cael A, Bao C, Danoix F, et al. Precipitation strengthening in high manganese austenitic TWIP steels. Int J Mater Res 2011;102(5):538–49.
[177] Jodi DE, Park J, Park N. Strengthening of ultrafine-grained equiatomic CoCrFeMnNi high-entropy alloy by nitrogen addition. Mater Lett 2020;258:126772.
[178] Stepanov N, Yurchenko NY, Tikhonovsky M, Salishchev G. Effect of carbon content and annealing on structure and hardness of the CoCrFeNiMn-based high entropy alloys. J Alloys Compd 2016;687:59–71.
[179] Lu Y, Mazilkin A, Boll T, Stepanov N, Zherebtzov S, Salishchev G, et al. Influence of carbon on the mechanical behavior and microstructure evolution of CoCrFeMnNi processed by high pressure torsion. Materialia 2021;16:101059.
[180] Moravcik I, Cizek J, Gouvea LdA, Cupera J, Guban I, Dlouhy I. Nitrogen interstitial alloying of CoCrFeMnNi high entropy alloy through reactive powder milling. Entropy 2019;21(4):363.
[181] Stepanov N, Shaysultanov D, Chernichenko R, Yurchenko NY, Zherebtsov S, Tikhonovsky M, et al. Effect of

thermomechanical processing on microstructure and mechanical properties of the carbon-containing CoCrFeNiMn high entropy alloy. J Alloys Compd 2017;693:394–405.
[182] Xie Y, Cheng H, Tang Q, Chen W, Chen W, Dai P. Effects of N addition on microstructure and mechanical properties of CoCrFeNiMn high entropy alloy produced by mechanical alloying and vacuum hot pressing sintering. Intermetallics 2018;93:228–34.
[183] Chmielak L, Mujica Roncery L, Niederhofer P, Weber S, Theisen W. CrMnFeCoNi high entropy alloys with carbon and nitrogen: mechanical properties, wear and corrosion resistance. SN Appl Sci 2021;3(11):1–12.
[184] Han Y, Li H, Feng H, Li K, Tian Y, Jiang Z. Enhancing the strength and ductility of CoCrFeMnNi high-entropy alloy by nitrogen addition. Mater Sci Eng, A 2020;789:139587.
[185] Ikeda Y, Körmann F. Impact of N on the stacking fault energy and phase stability of FCC CrMnFeCoNi: an ab initio study. J Phase Equilibria Diffus 2021;42(5):551–60.
[186] Ikeda Y, Tanaka I, Neugebauer J, Körmann F. Impact of interstitial C on phase stability and stacking-fault energy of the CrMnFeCoNi high-entropy alloy. Phys Review Mater 2019;3(11):113603.
[187] Chen L, Wei R, Tang K, Zhang J, Jiang F, He L, et al. Heavy carbon alloyed FCC-structured high entropy alloy with excellent combination of strength and ductility. Mater Sci Eng, A 2018;716:150–6.
[188] Klimova M, Semenyuk A, Shaysultanov D, Salishchev G, Zherebtsov S, Stepanov N. Effect of carbon on cryogenic tensile behavior of CoCrFeMnNi-type high entropy alloys. J Alloys Compd 2019;811:152000.
[189] Wang Z, Baker I, Guo W, Poplawsky JD. The effect of carbon on the microstructures, mechanical properties, and deformation mechanisms of thermo-mechanically treated Fe40. 4Ni11. 3Mn34. 8Al7. 5Cr6 high entropy alloys. Acta Mater 2017;126:346–60.
[190] Semenyuk A, Klimova M, Shaysultanov D, Salishchev G, Zherebtsov S, Stepanov N. Effect of nitrogen on microstructure and mechanical properties of the CoCrFeMnNi high-entropy alloy after cold rolling and subsequent annealing. J Alloys Compd 2021;888:161452.
[191] Jung Y-S, Kang S, Jeong K, Jung J-G, Lee Y-K. The effects of N on the microstructures and tensile properties of Fe–15Mn–0.6 C–2Cr–xN twinning-induced plasticity steels. Acta Mater 2013;61(17):6541–8.
[192] He Z, Jia N, Yan H, Shen Y, Zhu M, Guan X, et al. Multi-heterostructure and mechanical properties of N-doped FeMnCoCr high entropy alloy. Int J Plast 2021;139:102965.
[193] Jodi DE, Park J, Straumal B, Park N. Investigation on the precipitate formation and behavior in nitrogen-containing equiatomic CoCrFeMnNi high-entropy alloy. Mater Lett 2020;258:126806.
[194] Klimova M, Shaysultanov D, Chernichenko R, Sanin V, Stepanov N, Zherebtsov S, et al. Recrystallized microstructures and mechanical properties of a C-containing CoCrFeNiMn-type high-entropy alloy. Mater Sci Eng, A 2019;740:201–10.
[195] Kim JG, Park JM, Seol JB, Choe J, Yu J-H, Yang S, et al. Nano-scale solute heterogeneities in the ultrastrong selectively laser melted carbon-doped CoCrFeMnNi alloy. Mater Sci Eng, A 2020;773:138726.
[196] Zhang J, Yoon K-N, Kim M-S, Ahn H-S, Kim J-Y, Ryu W-H, et al. Manipulation of microstructure and mechanical properties in N-doped CoCrFeMnNi high-entropy alloys. Metals 2021;11(9):1487.
[197] Astafurova E, Melnikov E, Astafurov S, Reunova K, Panchenko M, Moskvina V, et al. A comparative study of a solid solution hardening in carbon-alloyed FeMnCrNiCo0. 95C0. 05 high-entropy alloy subjected to different thermal–mechanical treatments. Mater Lett 2021;285:129073.
[198] Gao N, Lu D, Zhao Y, Liu X, Liu G, Wu Y, et al. Strengthening of a CrMnFeCoNi high-entropy alloy by carbide precipitation. J Alloys Compd 2019;792:1028–35.
[199] Oriani R. Hydrogen embrittlement of steels. Annu Rev Mater Sci 1978;8(1):327–57.
[200] Johnson II WH. On some remarkable changes produced in iron and steel by the action of hydrogen and acids. Proc Roy Soc Lond 1875;23(156–163):168–79.
[201] Birnbaum HK, Sofronis P. Hydrogen-enhanced localized plasticity—a mechanism for hydrogen-related fracture. Mater Sci Eng, A 1994;176(1–2):191–202.
[202] Shih D, Robertson I, Birnbaum H. Hydrogen embrittlement of α titanium: in situ TEM studies. Acta Metall 1988;36(1):111–24.
[203] Luo H, Lu W, Fang X, Ponge D, Li Z, Raabe D. Beating hydrogen with its own weapon: nano-twin gradients enhance embrittlement resistance of a high-entropy alloy. Mater Today 2018;21(10):1003–9.
[204] Lee J, Park H, Kim M, Kim H-J, Suh J-y, Kang N. Role of hydrogen and temperature in hydrogen embrittlement of equimolar CoCrFeMnNi high-entropy alloy. Met Mater Int 2021;27(1):166–74.
[205] Xie Z, Wang Y, Lu C, Dai L. Sluggish hydrogen diffusion and hydrogen decreasing stacking fault energy in a high-entropy alloy. Mater Today Commun 2021;26:101902.
[206] Zhu T, Zhong Z, Ren X, Song Y, Ye F, Wang Q, et al. Influence of hydrogen behaviors on tensile properties of equiatomic FeCrNiMnCo high-entropy alloy. J Alloys Compd 2022;892:162260.
[207] Nygren K, Bertsch K, Wang S, Bei H, Nagao A, Robertson I. Hydrogen embrittlement in compositionally complex FeNiCoCrMn FCC solid solution alloy. Curr Opin Solid State Mater Sci 2018;22(1):1–7.
[208] Ji H, Park I-J, Lee S-M, Lee Y-K. The effect of pre-strain on hydrogen embrittlement in 310S stainless steel. J Alloys Compd 2014;598:205–12.
[209] Zhao Y, Lee D-H, Kim W-J, Seok M-Y, Kim J-Y, Han HN, et al. Influence of pre-strain on the gaseous hydrogen embrittlement resistance of a high-entropy alloy. Mater Sci Eng, A 2018;718:43–7.
[210] Fu Z, Yang B, Chen M, Gou G, Chen H. Effect of recrystallization annealing treatment on the hydrogen embrittlement behavior of equimolar CoCrFeMnNi high entropy alloy. Int J Hydrogen Energy 2021;46(9):6970–8.
[211] Nygren KE, Wang S, Bertsch KM, Bei H, Nagao A, Robertson IM. Hydrogen embrittlement of the equi-molar FeNiCoCr alloy. Acta Mater 2018;157:218–27.
[212] Koyama M, Wang H, Verma VK, Tsuzaki K, Akiyama E. Effects of Mn content and grain size on hydrogen embrittlement susceptibility of face-centered cubic high-entropy alloys. Metall Mater Trans 2020;51(11):5612–6.
[213] Xiao H, Zeng Q, Xia L, Fu Z, Zhu S. Hydrogen-assisted fatigue crack propagation behavior of equiatomic Co–Cr–Fe–Mn–Ni high-entropy alloy. Mater Corrosion 2021.
[214] Rogal Ł, Kalita D, Litynska-Dobrzynska L. CoCrFeMnNi high entropy alloy matrix nanocomposite with addition of Al2O3. Intermetallics 2017;86:104–9.
[215] Zhang X, Wang F, Yan X, Li X-Z, Hattar K, Cui B. Nanostructured oxide-dispersion-strengthened CoCrFeMnNi high-entropy alloys with high thermal stability. Adv Eng Mater 2021;23(9):2100291.
[216] Xie Y, Liang J, Zhang D, Luo Y, Zhang Z, Liu Y, et al. Sustaining strength–ductility synergy of CoCrFeNiMn high

entropy alloy by a multilevel heterogeneity associated with nanoparticles. Scripta Mater 2020;187:390–4.
[217] Gwalani B, Pohan RM, Waseem OA, Alam T, Hong SH, Ryu HJ, et al. Strengthening of Al0. 3CoCrFeMnNi-based ODS high entropy alloys with incremental changes in the concentration of Y2O3. Scripta Mater 2019;162:477–81.
[218] Xie Y, Zhou D, Luo Y, Xia T, Zeng W, Li C, et al. Fabrication of CoCrFeNiMn high entropy alloy matrix composites by thermomechanical consolidation of a mechanically milled powder. Mater Char 2019;148:307–16.
[219] Guo Z, Zhang A, Han J, Meng J. Microstructure, mechanical and tribological properties of CoCrFeNiMn high entropy alloy matrix composites with addition of Cr3C2. Tribol Int 2020;151:106436.
[220] Yim D, Sathiyamoorthi P, Hong S-J, Kim HS. Fabrication and mechanical properties of TiC reinforced CoCrFeMnNi high-entropy alloy composite by water atomization and spark plasma sintering. J Alloys Compd 2019;781:389–96.
[221] Asghari-Rad P, Nguyen NT-C, Kim Y, Zargaran A, Sathiyamoorthi P, Kim HS. TiC-reinforced CoCrFeMnNi composite processed by cold-consolidation and subsequent annealing. Mater Lett 2021;303:130503.
[222] Rogal Ł, Kalita D, Tarasek A, Bobrowski P, Czerwinski F. Effect of SiC nano-particles on microstructure and mechanical properties of the CoCrFeMnNi high entropy alloy. J Alloys Compd 2017;708:344–52.
[223] Orru R, Licheri R, Locci AM, Cincotti A, Cao G. Consolidation/synthesis of materials by electric current activated/assisted sintering. Mater Sci Eng R Rep 2009;63(4–6):127–287.
[224] Chung S, Lee B, Lee SY, Do C, Ryu HJ. The effects of Y pre-alloying on the in-situ dispersoids of ODS CoCrFeMnNi high-entropy alloy. J Mater Sci Technol 2021;85:62–75.
[225] Jiang F, Zhao C, Liang D, Zhu W, Zhang Y, Pan S, et al. In-situ formed heterogeneous grain structure in spark-plasma-sintered CoCrFeMnNi high-entropy alloy overcomes the strength-ductility trade-off. Mater Sci Eng, A 2020;771:138625.
[226] Praveen S, Basu J, Kashyap S, Kottada RS. Exceptional resistance to grain growth in nanocrystalline CoCrFeNi high entropy alloy at high homologous temperatures. J Alloys Compd 2016;662:361–7.
[227] Yang M-S, Liu X-B, Fan J-W, He X-M, Shi S-H, Fu G-Y, et al. Microstructure and wear behaviors of laser clad NiCr/Cr3C2–WS2 high temperature self-lubricating wear-resistant composite coating. Appl Surf Sci 2012;258(8):3757–62.
[228] Takeuchi A, Inoue A. Calculations of mixing enthalpy and mismatch entropy for ternary amorphous alloys. Mater Trans, JIM 2000;41(11):1372–8.
[229] Szklarz Z, Lekki J, Bobrowski P, Szklarz MB, Rogal Ł. The effect of SiC nanoparticles addition on the electrochemical response of mechanically alloyed CoCrFeMnNi high entropy alloy. Mater Chem Phys 2018;215:385–92.
[230] Sathiaraj GD, Bhattacharjee PP. Effect of cold-rolling strain on the evolution of annealing texture of equiatomic CoCrFeMnNi high entropy alloy. Mater Char 2015;109:189–97.
[231] Sathiaraj G, Tsai C, Yeh J, Jahazi M, Bhattacharjee PP. The effect of heating rate on microstructure and texture formation during annealing of heavily cold-rolled equiatomic CoCrFeMnNi high entropy alloy. J Alloys Compd 2016;688:752–61.
[232] Sathiaraj GD, Bhattacharjee PP, Tsai C-W, Yeh J-W. Effect of heavy cryo-rolling on the evolution of microstructure and texture during annealing of equiatomic CoCrFeMnNi high entropy alloy. Intermetallics 2016;69:1–9.
[233] Park N, Lee B-J, Tsuji N. The phase stability of equiatomic CoCrFeMnNi high-entropy alloy: comparison between experiment and calculation results. J Alloys Compd 2017;719:189–93.
[234] Heydarinia A, Koushki A, Rasooli N, Hosseinzadeh MR, Sohrabi MJ, Mehranpour MS. Synergistic investigations of post-deformation annealing and initial microstructure on the mechanical properties of high strength low alloy (HSLA)-100 steel. Steel Res Int 2021;92:2000627.
[235] Sun S, Tian Y, Lin H, Yang H, Dong X, Wang Y, et al. Achieving high ductility in the 1.7 GPa grade CoCrFeMnNi high-entropy alloy at 77 K. Mater Sci Eng, A 2019;740:336–41.
[236] Patra S, Hasan SM, Narasaiah N, Chakrabarti D. Effect of bimodal distribution in ferrite grain sizes on the tensile properties of low-carbon steels. Mater Sci Eng, A 2012;538:145–55.
[237] Mehranpour MS, Heydarinia A, Emamy M, Mirzadeh H, Koushki A, Razi R. Enhanced mechanical properties of AZ91 magnesium alloy by inoculation and hot deformation. Mater Sci Eng, A 2020;802:140667.
[238] Chakravarthy SS, Curtin W. Stress-gradient plasticity. Proc Natl Acad Sci USA 2011;108(38):15716–20.
[239] Wu X, Jiang P, Chen L, Zhang J, Yuan F, Zhu Y. Synergetic strengthening by gradient structure. Mater Res Lett 2014;2(4):185–91.
[240] Park HK, Ameyama K, Yoo J, Hwang H, Kim HS. Additional hardening in harmonic structured materials by strain partitioning and back stress. Mater Res Lett 2018;6(5):261–7.
[241] Ma X, Huang C, Xu W, Zhou H, Wu X, Zhu Y. Strain hardening and ductility in a coarse-grain/nanostructure laminate material. Scripta Mater 2015;103:57–60.
[242] Moon J, Bouaziz O, Kim HS, Estrin Y. Twinning engineering of a CoCrFeMnNi high-entropy alloy. Scripta Mater 2021;197:113808.
[243] Bouaziz O, Allain S, Scott C, Cugy P, Barbier D. High manganese austenitic twinning induced plasticity steels: a review of the microstructure properties relationships. Curr Opin Solid State Mater Sci 2011;15(4):141–68.
[244] Moon J, Bouaziz O, Kim HS, Estrin Y. Twinning engineering of high-entropy alloys: an exercise in process optimization and modeling. Mater Sci Eng, A 2021;822:141681.
[245] Watanabe H, Murata T, Nakamura S, Ikeo N, Mukai T, Tsuchiya K. Effect of cold-working on phase formation during heat treatment in CrMnFeCoNi system high-entropy alloys with Al addition. J Alloys Compd 2021;872:159668.
[246] Shim SH, Moon J, Pouraliakbar H, Lee BJ, Hong SI, Kim HS. Toward excellent tensile properties of nitrogen-doped CoCrFeMnNi high-entropy alloy at room and cryogenic temperatures. J Alloys Compd 2021;897:163217.
[247] Jodi DE, Park J, Park N. Precipitate behavior in nitrogen-containing CoCrNi medium-entropy alloys. Mater Char 2019;157:109888.
[248] Hemphill MA, Yuan T, Wang G, Yeh J, Tsai C, Chuang A, et al. Fatigue behavior of Al0. 5CoCrCuFeNi high entropy alloys. Acta Mater 2012;60(16):5723–34.
[249] Tang Z, Yuan T, Tsai C-W, Yeh J-W, Lundin CD, Liaw PK. Fatigue behavior of a wrought Al0. 5CoCrCuFeNi two-phase high-entropy alloy. Acta Mater 2015;99:247–58.
[250] Thurston KV, Gludovatz B, Hohenwarter A, Laplanche G, George EP, Ritchie RO. Effect of temperature on the fatigue-crack growth behavior of the high-entropy alloy CrMnFeCoNi. Intermetallics 2017;88:65–72.
[251] Thurston KV, Gludovatz B, Yu Q, Laplanche G, George EP, Ritchie RO. Temperature and load-ratio dependent fatigue-crack growth in the CrMnFeCoNi high-entropy alloy. J Alloys Compd 2019;794:525–33.

[252] Suresh S, Ritchie R. A geometric model for fatigue crack closure induced by fracture surface roughness. Metall Trans A 1982;13(9):1627–31.
[253] Pippan R, Haberz K, Stüwe H. The plastic deformation of fracture surface contacts in fatigue. Eng Fract Mech 1996;53(3):441–8.
[254] Mizumachi S, Koyama M, Fukushima Y, Tsuzaki K. Growth behavior of a mechanically long fatigue crack in an FeCrNiMnCo high entropy alloy: a comparison with an austenitic stainless steel. ISIJ Int 2020;60(1):175–81.
[255] Zhang Z, Mao M, Wang J, Gludovatz B, Zhang Z, Mao SX, et al. Nanoscale origins of the damage tolerance of the high-entropy alloy CrMnFeCoNi. Nat Commun 2015;6:10143.
[256] Ludwigson D. Modified stress-strain relation for FCC metals and alloys. Metall Trans A 1971;2(10):2825–8.
[257] Suzuki K, Koyama M, Hamada S, Tsuzaki K, Noguchi H. Planar slip-driven fatigue crack initiation and propagation in an equiatomic CrMnFeCoNi high-entropy alloy. Int J Fatig 2020;133:105418.
[258] Suzuki K, Hamada S, Koyama M, Tsuzaki K, Noguchi H. Notch shape dependence of fatigue crack extension in equiatomic CrMnFeCoNi high-entropy alloy. Int J Fatig 2021;153:106481.
[259] Li W, Chen S, Liaw PK. Discovery and design of fatigue-resistant high-entropy alloys. Scripta Mater 2020;187:68–75.
[260] Stephens RI, Fatemi A, Stephens RR, Fuchs HO. Metal fatigue in engineering. John Wiley & Sons; 2000.
[261] Lee GT, Won JW, Lim KR, Kang M, Kwon HJ, Na YS, et al. Effect of microstructural features on the high-cycle fatigue behavior of CoCrFeMnNi high-entropy alloys deformed at room and cryogenic temperatures. Met Mater Int 2021;27(4):593–602.
[262] Ghomsheh MZ, Khatibi G, Weiss B, Lederer M, Schwarz S, Steiger-Thirsfeld A, et al. High cycle fatigue deformation mechanisms of a single phase CrMnFeCoNi high entropy alloy. Mater Sci Eng, A 2020;777:139034.
[263] Oevermann T, Wegener T, Liehr A, Hübner L, Niendorf T. Evolution of residual stress, microstructure and cyclic performance of the equiatomic high-entropy alloy CoCrFeMnNi after deep rolling. Int J Fatig 2021;153:106513.
[264] Shams S, Jang G, Won J, Bae J, Jin H, Kim H, et al. Low-cycle fatigue properties of CoCrFeMnNi high-entropy alloy compared with its conventional counterparts. Mater Sci Eng, A 2020;792:139661.
[265] Shams SAA, Kim G, Won JW, Kim JN, Kim HS, Lee CS. Effect of grain size on the low-cycle fatigue behavior of carbon-containing high-entropy alloys. Mater Sci Eng, A 2021;810:140985.
[266] Lu K, Chauhan A, Walter M, Tirunilai AS, Schneider M, Laplanche G, et al. Superior low-cycle fatigue properties of CoCrNi compared to CoCrFeMnNi. Scripta Mater 2021;194:113667.
[267] Lu K, Chauhan A, Tirunilai AS, Freudenberger J, Kauffmann A, Heilmaier M, et al. Deformation mechanisms of CoCrFeMnNi high-entropy alloy under low-cycle-fatigue loading. Acta Mater 2021;215:117089.
[268] Lu K, Chauhan A, Litvinov D, Walter M, Tirunilai AS, Freudenberger J, et al. High-temperature low cycle fatigue behavior of an equiatomic CoCrFeMnNi high-entropy alloy. Mater Sci Eng, A 2020;791:139781.
[269] Li P, Li S, Wang Z, Zhang Z. Fundamental factors on formation mechanism of dislocation arrangements in cyclically deformed fcc single crystals. Prog Mater Sci 2011;56(3):328–77.
[270] Luo M-Y, Lam T-N, Wang P-T, Tsou N-T, Chang Y-J, Feng R, et al. Grain-size-dependent microstructure effects on cyclic deformation mechanisms in CoCrFeMnNi high-entropy-alloys. Scripta Mater 2022;210:114459.
[271] Picak S, Wegener T, Sajadifar S, Sobrero C, Richter J, Kim H, et al. On the low-cycle fatigue response of CoCrNiFeMn high entropy alloy with ultra-fine grain structure. Acta Mater 2021;205:116540.
[272] Wang A, An X, Gu J, Wang X, Li L, Li W, et al. Effect of grain size on fatigue cracking at twin boundaries in a CoCrFeMnNi high-entropy alloy. J Mater Sci Technol 2020;39:1–6.
[273] Hong S-G, Lee S-B. The tensile and low-cycle fatigue behavior of cold worked 316L stainless steel: influence of dynamic strain aging. Int J Fatig 2004;26(8):899–910.
[274] Niendorf T, Wegener T, Li Z, Raabe D. Unexpected cyclic stress-strain response of dual-phase high-entropy alloys induced by partial reversibility of deformation. Scripta Mater 2018;143:63–7.
[275] Bahadur F, Biswas K, Gurao N. Micro-mechanisms of microstructural damage due to low cycle fatigue in CoCuFeMnNi high entropy alloy. Int J Fatig 2020;130:105258.
[276] Feng R, Rao Y, Liu C, Xie X, Yu D, Chen Y, et al. Enhancing fatigue life by ductile-transformable multicomponent B2 precipitates in a high-entropy alloy. Nat Commun 2021;12(1):1–10.
[277] Shams SAA, Bae JW, Kim JN, Kim HS, Lee T, Lee CS. Origin of superior low-cycle fatigue resistance of an interstitial metastable high-entropy alloy. J Mater Sci Technol 2022;115:115–28.
[278] Vakili S, Zarei-Hanzaki A, Anoushe A, Abedi H, Mohammad-Ebrahimi M, Jaskari M, et al. Reversible dislocation movement, martensitic transformation and nano-twinning during elastic cyclic loading of a metastable high entropy alloy. Acta Mater 2020;185:474–92.
[279] Langdon TG. A unified approach to grain boundary sliding in creep and superplasticity. Acta Metall Mater 1994;42(7):2437–43.
[280] Cao C, Fu J, Tong T, Hao Y, Gu P, Hao H, et al. Intermediate-temperature creep deformation and microstructural evolution of an equiatomic FCC-structured CoCrFeNiMn high-entropy alloy. Entropy 2018;20(12):960.
[281] Kang YB, Shim SH, Lee KH, Hong SI. Dislocation creep behavior of CoCrFeMnNi high entropy alloy at intermediate temperatures. Mater Res Lett 2018;6(12):689–95.
[282] Kim Y-K, Yang S, Lee K-A. Compressive creep behavior of selective laser melted CoCrFeMnNi high-entropy alloy strengthened by in-situ formation of nano-oxides. Addit Manuf 2020;36:101543.
[283] Rozman KA, Detrois M, Liu T, Gao M, Jablonski P, Hawk J. Long-term creep behavior of a CoCrFeNiMn high-entropy alloy. J Mater Eng Perform 2020;29(9):5822–39.
[284] Jeong H, Kim WJ. Calculation and construction of deformation mechanism maps and processing maps for CoCrFeMnNi and Al0. 5CoCrFeMnNi high-entropy alloys. J Alloys Compd 2021;869:159256.
[285] Barnes AJ. Superplastic forming 40 years and still growing. J Mater Eng Perform 2007;16(4):440–54.
[286] Langdon TG. The mechanical properties of superplastic materials. Metall Trans A 1982;13(5):689–701.
[287] Valiev RZ, Kaibyshev OA, Kuznetsov RI, Musalimov RSh, Tsenev NK. Low-temperature superplasticity of metallic materials. Dokl Akad Nauk SSSR 1988;301:864–6.
[288] Langdon TG. The background to superplastic forming and opportunities arising from new developments. Solid State Phenom 2020;306:1–8.
[289] Langdon TG. Seventy-five years of superplasticity: historic developments and new opportunities. J Mater Sci 2009;44(22):5998–6010.
[290] Langdon TG. An evaluation of the strain contributed by grain boundary sliding in superplasticity. Mater Sci Eng, A 1994;174(2):225–30.

[291] Kawasaki M, Langdon TG. Principles of superplasticity in ultrafine-grained materials. J Mater Sci 2007;42(5):1782–96.
[292] Kawasaki M, Langdon TG. Achieving superplasticity in metals processed by high-pressure torsion. J Mater Sci 2014;49(19):6487–96.
[293] Kawasaki M, Langdon TG. Achieving superplastic properties in ultrafine-grained materials at high temperatures. J Mater Sci 2016;51(1):19–32.
[294] Shahmir H, Kawasaki M, Langdon TG. The potential for achieving superplasticity in high-entropy alloys processed by severe plastic deformation. IOP Conf Ser Mater Sci Eng 2017;194:012040.
[295] Reddy S, Bapari S, Bhattacharjee PP, Chokshi AH. Superplastic-like flow in a fine-grained equiatomic CoCrFeMnNi high-entropy alloy. Mater Res Lett 2017;5(6):408–14.
[296] Shahmir H, He J, Lu Z, Kawasaki M, Langdon TG. Evidence for superplasticity in a CoCrFeNiMn high-entropy alloy processed by high-pressure torsion. Mater Sci Eng, A 2017;685:342–8.


Prof. Terence G. Langdon

Professor Terence G. Langdon graduated in Physics from the University of Bristol in 1961 and obtained a Ph.D. degree in Physical Metallurgy from Imperial College, University of London, in 1965. He was awarded a D.Sc. degree in Physics by the University of Bristol, elected a Fellow of the Royal Academy of Engineering and received honorary doctorates from the Russian Academy of Sciences and Peter the Great Saint Petersburg Polytechnic University. He was on the faculty of the University of Southern California from 1971 until 2012 and then retired to England and was appointed Professor of Materials Science at the University of Southampton. He has received numerous awards including the Blaise Pascal Medal from the European Academy of Sciences, the Lee Hsun Award from the Chinese Academy of Sciences, the Honorary Medal "De Scientia et Humanitate Optime Meritis" of the Academy of Sciences of the Czech Republic and the Acta Materialia Gold Medal. He is listed on Google Scholar with more than 90,000 citations and an h-index of 144.


Dr. Hamed Shahmir

Dr. Hamed Shahmir graduated from School of Materials Science and Engineering, University of Tehran in 2015. After graduation, he started working in University of Southampton in UK as a Research Fellow (2015–2017) and then succeeded to get support from National Elites Foundation of Islamic Republic of Iran for accomplishing research as a Research Fellow in University of Tehran (2017–2019). Afterwards, he had a position as a Research Associate in University of Sheffield, UK (2019-2020). After that, he returned to Iran and started his career as Assistance Professor in Department of Materials Engineering of Tarbiat Modares University. His experiences on material processing combined with strong background in physical metallurgy, phase transformations and deformation mechanisms at ambient and high temperatures, place him in a very strong position to work on microstructure engineering in metallic materials.


Dr. Seyed Amir Arsalan Shams

Dr. Seyed Amir Arsalan Shams received his Ph.D. degree from Iran University of Science and Technology (IUST) in 2017. He focused on low cycle fatigue behavior of High Entropy alloys from 2018 to 2022 when he was a researcher at Graduate Institute of Ferrous Technology (GIFT) in Pohang University of Science and Technology (POSTECH), Korea. He is now doing research on enhancing fatigue behavior of HEAs in IUST as a senior researcher.


Mr. Mohammad Sajad Mehranpour

Mr. Mohammad Sajad Mehranpour graduated from School of Materials Science and Engineering, University of Tehran in 2020. He is currently working as a researcher assistant at the Tarbiat Modares University, Iran. He focused on microstructural engineering of CoCrFeNiMn high-entropy alloy. His research interests include thermomechanical processing, severe plastic deformation, high-entropy alloys, microstructural engineering, and overcoming strength-ductility trade-off. His current research is to design some novel alloys and tailor their microstructure in order to overcome the strength-ductility trade-off.